



COMPACT LASER SOURCES FROM THE
EXTREME ULTRAVIOLET TO THE MID-
INFRARED SPECTRAL RANGE

Thesis presented to the *Faculty of Science* for the degree of
Doctor of Science

Loïc P. J. M. Merceron

M. Sc. In Physics

submitted on 23.04.2019 to the jury:

Prof. Thomas Südmeyer	Director
Prof. Bojan Resan	Examiner
Dr. Stéphane Schilt	Examiner
Dr. Valentin J. Wittwer	Examiner

Neuchâtel, 2019

IMPRIMATUR POUR THESE DE DOCTORAT

**La Faculté des sciences de l'Université de Neuchâtel
autorise l'impression de la présente thèse soutenue par**

Monsieur Loïc P.J.M. MERCERON

Titre:

**“Compact laser sources from the extreme
ultraviolet to the mid-infrared
spectral range”**

sur le rapport des membres du jury composé comme suit:

- Prof. Thomas Südmeyer, directeur de thèse, Université de Neuchâtel, Suisse
- Dr Stéphane Schilt, Université de Neuchâtel, Suisse
- Dr Valentin Wittwer, Université de Neuchâtel, Suisse
- Prof. Bojan Resan, Fachhochschule Nordwestschweiz, Windisch, Suisse

Neuchâtel, le 15 juillet 2019

Le Doyen, Prof. P. Felber



Keywords – Mots-clés

Keywords

Thin-disk laser (TDL), difference frequency generation (DFG), high-harmonic generation (HHG), modelocked laser, ultrafast laser, high-power laser, diode-pumped solid-state laser (DPSSL), femtosecond, optical frequency comb, optical fiber amplifier, frequency noise, phase noise, near infrared (near-IR), mid-infrared (mid-IR), extreme ultra-violet (XUV).

Mots-clés

Laser à disque fin (TDL), génération de différence de fréquence (DFG), génération d'harmoniques d'ordre élevé (HHG), laser à verrouillage de mode, laser ultra-rapide, laser à haute puissance, laser à corps solide pompé par diode (DPSSL), femto-seconde, peigne de fréquence optique, amplificateur optique à fibre, bruit de fréquence, bruit de phase, proche infrarouge, infrarouge moyen, extrême ultraviolet (EUV).

Abstract

Lasers have revolutionized the way we live and work in so many ways and have become a major part of our lives. We use them in telecommunications, medical care, material processing, data storage and printing, just to name a few. Lasers have proved to be important tools and are a major subject of research in science, continuously developed further and finding new uses. Pushed by the need to characterize absorption lines of molecules in gas phase, laser radiation in the mid-infrared (mid-IR) have become very desirable. On the other hand, the intense electric fields created by lasers revealed new aspects of nature's behavior and extreme non-linear processes like high-harmonic generation (HHG) could be demonstrated. They gave us access to new sources of coherent radiation in the extreme ultra-violet. This thesis presents the development of compact laser sources in the mid-infrared by difference frequency generation (DFG) inside an enhancement cavity driven by high power fiber amplifiers on one side, and in the extreme ultraviolet (XUV) by high harmonic generation inside a modelocked thin-disk laser oscillator on the other side.

In the first part of this work, the implementation of a narrow linewidth and high-power 3- μm source based on DFG between 1- μm and 1.5- μm radiations inside an enhancement cavity supplied by two high-power fiber amplifiers is presented. Up to 120 mW of 3- μm radiation is measured, corresponding to a conversion efficiency of $1.4 \text{ mW}\cdot\text{W}^{-2}\cdot\text{cm}^{-1}$ for the overall system and $98.5 \mu\text{W}\cdot\text{W}^{-2}\cdot\text{cm}^{-1}$ for the intracavity conversion efficiency (equivalent to single-pass). The 3- μm frequency noise is estimated by measuring the noise of the semiconductor laser diodes that seed the system as well as the additive noise from the rest of the setup. This latter noise characterization is achieved by analyzing the beat note between the high-power continuous-wave cavity-enhanced DFG radiation and a single-pass DFG source seeded by two fiber amplifiers operating at the same wavelength. As the two systems are seeded by the same laser diodes, the additive frequency noise of the fiber amplifiers, the crystals and the cavity is characterized. It is shown that only the frequency noise of the laser diodes (at 1064 nm and 1560 nm) contributes to the linewidth of the mid-IR radiation (evaluated to amount to 1.1 MHz in our case).

Coherent extreme ultraviolet light sources open up numerous opportunities for science and technology. Femtosecond laser-driven HHG in gases is the most successful method for coherent table-top XUV generation in contrast to synchrotrons. While initial HHG systems were limited to low repetition rates, the last years have seen a strong research

effort on MHz systems. High repetition rates can strongly reduce measurement time, improve signal-to-noise ratio, and enable XUV frequency comb metrology. However, current MHz HHG sources have a high degree of complexity. In the last part of this thesis, a compact XUV source that generates high harmonics directly inside the cavity of a modelocked thin-disk laser (TDL) oscillator is presented. The laser is directly diode-pumped at a power of only 51 W and operates at a wavelength of 1034 nm and 17.4 MHz repetition rate. HHG is driven in a high-pressure xenon gas jet with an intracavity peak intensity of 2.8×10^{13} W/cm² and 320 W of intracavity average power. Despite the high-pressure gas jet, the laser operates at high stability. Harmonics up to the 17th order (60.8 nm, 20.4 eV) are observed and a flux of 2.6×10^8 photons/s for the 11th harmonic (94 nm, 13.2 eV) is estimated. Due to the power-scalability of the thin disk concept, it is highly expected that this new class of compact XUV sources will become a versatile tool for areas such as structural analysis of matter, attosecond science, XUV spectroscopy, and high-resolution imaging.

Résumé

Les lasers ont révolutionné notre manière de vivre et de travailler à bien des égards, à tel point qu'ils sont devenus un élément essentiel de nos vies. Nous les utilisons dans les domaines des télécommunications, des soins médicaux, du traitement des matériaux, du stockage de données ainsi que dans l'imprimerie, pour ne pas tous les nommer. Depuis leur invention, les lasers n'ont cessé d'être développés et leur utilisation s'étend continuellement vers de nouveaux domaines. Ils sont devenus des outils essentiels et représentent un sujet majeur de recherche scientifique. Poussé par la nécessité de caractériser les raies d'absorption de molécules en phase gazeuse, les lasers émettant dans la gamme de l'infrarouge sont devenus très désirables. D'autre part, les champs électriques intenses créés par rayonnement laser ont révélé de nouveaux aspects des lois naturelles comme les processus extrêmement non linéaires de conversion de photon telle la génération d'harmonique d'ordre élevée. Ce phénomène nous a donné accès à de nouvelles sources cohérentes de radiations pouvant s'étendre jusqu'à l'extrême ultraviolet. Cette thèse présente, d'une part, le développement de sources lasers compactes émettant dans l'infrarouge moyen par différence de fréquence dans une cavité résonante, et d'autre part dans l'extrême ultraviolet par génération d'harmoniques d'ordre élevé dans un oscillateur laser à disque fin à verrouillage de modes.

La première partie de ce mémoire présente l'implémentation d'une source à 3 μm basée sur la différence de fréquence entre des rayonnements à 1064 nm et 1560 nm à l'intérieur d'une cavité Fabry-Pérot alimentée par deux amplificateurs à fibres de haute-puissance. Jusqu'à 120 mW de puissance à 3 μm ont été mesurés, correspondant à une efficacité de conversion de $1.4 \text{ mW}\cdot\text{W}^{-2}\cdot\text{cm}^{-1}$ pour l'ensemble du système et à $98.5 \mu\text{W}\cdot\text{W}^{-2}\cdot\text{cm}^{-1}$ pour l'efficacité de conversion intra-cavité. Le bruit de fréquence du rayonnement généré à 3 μm est estimé en mesurant le bruit provenant des diodes sources à semi-conducteurs (à 1 μm et 1.5 μm) ainsi que le bruit additif provenant du reste du montage expérimental. Cette dernière caractérisation de bruit est faite en mesurant le battement entre le rayonnement à 3 μm provenant de la cavité Fabry-Pérot et celui d'une seconde source à 3 μm générée de manière similaire à partir des mêmes sources lasers, amplifiées séparément, mais dans une configuration non-résonante. Comme les deux systèmes opèrent avec les mêmes diodes sources, seul le bruit additif est caractérisé, comprenant le bruit provenant des amplificateurs à fibre, des cristaux et de la cavité. Il est démontré que

seul le bruit provenant des lasers sources contribue effectivement à la largeur de raie du rayonnement à 3 μm , évaluée dans ce cas à 1.1 MHz.

Les sources de lumière cohérentes dans l'extrême ultraviolet (EUV) ouvrent de nombreuses voies et opportunités pour la science et la technologie. La génération d'harmoniques d'ordre élevé dans les gaz par des sources lasers femto-secondes est la méthode la plus courante pour obtenir une source de rayonnement EUV compacte (à la différence de grandes installations telles les synchrotrons). Alors qu'initialement la génération d'harmoniques était limitée à de faibles taux de répétition, les dernières années ont été témoin d'un grand effort de la part de nombreux groupes de recherche pour développer des systèmes opérant dans les MHz. En effet, de hauts taux de répétition réduisent fortement les temps de mesures, améliorent grandement le rapport signal-à-bruit et rendent possible la génération de peignes de fréquence allant jusque dans l'EUV. Néanmoins, les sources actuelles d'harmoniques au MHz possèdent un haut degré de complexité. La deuxième partie de cette thèse traite d'une source compacte de rayonnement EUV générant de hautes harmoniques directement à l'intérieur de la cavité d'un oscillateur laser à disque fin à modes verrouillés. Le laser est directement pompé par diode à une puissance de 51 W et opère à une longueur d'onde de 1034 nm avec un taux de répétition de 17.4 MHz. Les hautes harmoniques sont générées dans un jet de Xénon à haute pression avec une intensité pic intra-cavité de 2.8×10^{13} W/cm² et 320 W de puissance moyenne intra-cavité. Malgré le jet de gaz à haute pression, le laser fonctionne avec une grande stabilité. Des harmoniques jusqu'au 17^{ème} ordre (60.8 nm, 20.4 eV) ont été observées avec un flux de photon estimé à 2.6×10^8 photons/s pour la 11^{ème} harmonique (94 nm, 13.2 eV). Grâce à la puissance évolutive du concept des lasers à disques fins, cette nouvelle classe de source EUV est en passe de devenir un outil versatile dans de nombreux domaines, tels que l'analyse structurale de matière, l'attoscience, la spectroscopie EUV et l'imagerie de haute résolution.

Contents

Keywords – Mots-clés	i
Abstract.....	iii
Résumé	v
Contents	vi
Chapter 1 Introduction	1
Chapter 2 Continuous-wave difference frequency generation inside an enhancement cavity	7
Introduction	7
Overview of mid-IR sources	8
2.1 High power fiber amplifiers.....	11
2.1.1 Basics of fiber amplifiers.....	11
2.1.2 Design and experiment	16
2.2 Difference frequency generation in a PPLN.....	28
2.2.1 Theoretical background	28
2.2.2 Single-pass difference frequency generation experiment.....	33
2.3 Difference frequency generation inside an enhancement cavity	42
2.3.1 Enhancement of the 1.5- μm signal in a resonant cavity.....	42
2.3.2 3- μm DFG inside a resonant cavity.....	48
2.4 Noise characterization of the intracavity DFG source.....	55
2.4.1 Choice of linewidth determination method	55
2.4.2 Setup of the second source of 3- μm	57
2.4.3 Noise analysis	61
Conclusion.....	67

Chapter 3	High harmonic generation in an ultrafast thin-disk laser oscillator.....	68
	Introduction	68
3.1	Modelocked thin-disk lasers	71
3.2	Thin-disk modelocking for intracavity HHG.....	82
3.2.1	CALGO-based thin-disk laser	82
3.2.2	LuO thin-disk modelocked oscillator in air	87
3.2.3	LuO thin-disk modelocked oscillator in vacuum	93
3.3	High harmonics generation.....	98
	Conclusion.....	103
Chapter 4	Conclusion and outlook	106
	Bibliography	108
	Curriculum vitae.....	115
	Remerciements	117

Chapter 1

Introduction

Since their invention by Theodore Maiman at Hughes Research Laboratories in 1960 [1], LASERs (light amplification by stimulated emission of radiation) have found numerous applications not only in our daily life but also in industry and in science, seeding greatly their popularity and the research effort for their development. Far from the previsions of the newspapers at the time of its invention, speaking of “killing rays”, the laser has been one of the main actors of the technological revolution of the late century and has invaded our lives through many devices such as smartphones, computers, flat screens, optical mouse, printers or DVD and Blu-rays for data writing, storage and processing. The latest advances in telecommunications also greatly rely on the laser technology with optical fibers, allowing terabits of data transfer all around the world, changing profoundly communication habits of the society.

Laser welding, cutting and polishing processes opened a large panel of possibilities for the industry. Metal processing industries can benefit from extreme high accuracy and precision by processing pieces down to the micrometer level using laser radiation. Injection nozzles for the automobile industry, turbine blades for the aviation industry or medical implants like stents can be produced at high accuracy thanks to laser micro-machining. Lasers find also an increasing number of applications in medicine where they can be used as a scalpel, e.g., for eye surgery with the huge advantage of avoiding any physical contact and thus limiting the risk of infection.

In addition to industrial and medical applications, lasers have proven to be an essential tool in most experimental research domains of science: biology, chemistry, physics and material science. The coherent and low diverging light emitted from lasers allows, once focused on a tight spot, the

creation of strong electric fields enabling the study of nature's laws under new conditions. On the other hand, the high specificity of the absorption of light in a propagation medium makes lasers a versatile and powerful tool for chemical species detection, but also for pumping atoms and probing their transitions. Some of the fundamental scientific questions were answered with the help of lasers, as proven by the recent Nobel Prize for Gravitational waves detection [2] inside the Laser Interferometer Gravitational-Waves Observatory (LIGO), which constitutes basically a large-scale laser interferometer measurement setup.

Lasers are thus considered as a polyvalent tool which has revolutionized modern technology. Laser physics is still a hot and exciting research topic in which any advance has a possible repercussion for a large panel of applications.

Lasers can operate in two temporal regimes: the continuous-wave (cw) operation, where the laser intensity is constant in time and the pulsed operation, where the temporal intensity is shaped as a train of pulses with a duration ranging from microseconds down to a few femtoseconds.

In the cw regime, the electric field amplitude as well as the intensity are constant over time. In the case of single-frequency lasers, only one line is emitted in the frequency domain. This frequency can be tuned, e.g. by changing the operating temperature for semiconductor lasers. With their tunable frequency, cw lasers are highly important for precision spectroscopy. For many applications, a high spectral purity, or in other terms a very small width of their spectral line, is essential.

The laser linewidth originates from both quantum noise arising from inherent spontaneous emission and additional technical noise resulting from e.g. vibrations of mechanical components or a noisy power supply. The laser linewidth is usually characterized by its full width at half maximum (FWHM) and for most cases cannot be directly measured on an optical spectrometer. To measure it, one commonly used technic consists in detecting a heterodyne beat between the laser under study and a reference laser with significantly lower frequency noise. The characterization of the beat frequency noise directly leads to the frequency noise of the laser under study and, from it, its linewidth can be estimated. In [3] Di Domenico et al. propose a simple approximation allowing to estimate the laser linewidth from the its frequency noise power spectral density (FN-PSD).

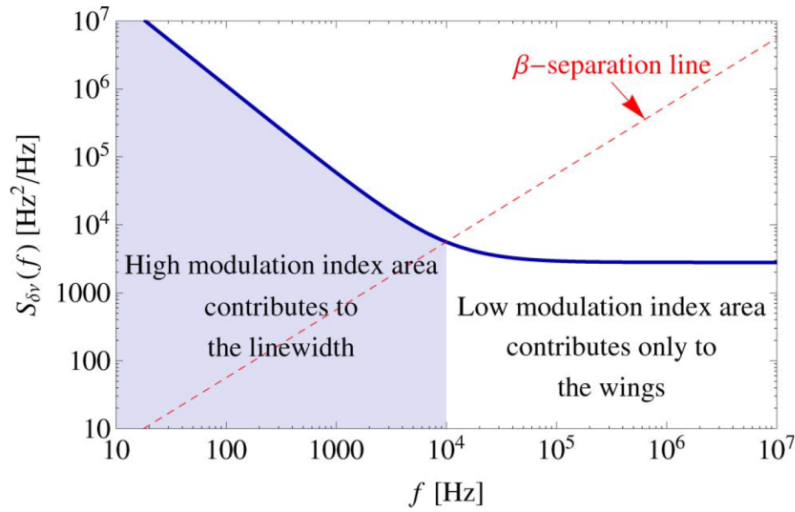


Figure 1.1: Illustration of the β -separation line approximation. A typical FN-PSD composed of $1/f$ noise at low Fourier frequencies and of white noise at high Fourier frequencies. The red dashed-line separates the spectrum into two regions whose contributions to the laser line shape is very different: the light blue area contributes to the linewidth, whereas the white area contributes only to the wings of the line shape. Figure taken from [3].

As depicted in Figure 1.1, the approximation of the β -separation line consists in dividing the frequency noise PSD into two regions delimited by the so-called β -separation line, which contribute differently to the shape of the laser spectrum: the region where the frequency noise is lower than the β -separation line does not contribute to the FWHM linewidth, while the region where the frequency noise exceeds the β -separation line does contribute to the laser linewidth. The FWHM linewidth can be approximated from the surface A below the FN-PSD for Fourier frequencies for which the noise is higher than the β -separation line (in light blue in Figure 1.1:

$$FWHM = \sqrt{8 \ln 2 A}.$$

However, one has to keep in mind that in terms of noise characterization, the linewidth only gives access to a limited information concerning the laser frequency noise. One important research direction is the development of powerful cw-lasers operating at narrow linewidth in the mid-IR region, which gives access to efficient sensing applications in the molecular fingerprint region.

In the pulsed regime, a laser delivers optical pulses with a certain repetition rate, pulse duration and energy. Among different methods to achieve such a regime, one of the most widespread is the modelocking. This

term refers to the phase locking of the resonant modes of the laser cavity. This method has the striking advantage to generate stable ultrashort pulses with pulse durations that can reach the femtosecond range [4]. This confinement of the optical energy in the time domain allows generating high peak power levels. When tightly focused in space, fs-pulses with sufficient energy achieve high intensities that allow reaching electric field strengths comparable to the bonding field of electrons with nuclei. Ultrafast modelocked lasers, thus, enable the study of the interaction of matter with strong electric fields. This enables important scientific tools such as high harmonic generation (HHG).

HHG typically occurs when an ultra-short laser pulse is focused inside a gas, reaching an intensity in the order of 10^{14} W/cm². The gas reacts to the incoming laser by emitting a coherent radiation consisting in odd harmonics of the laser frequency. Starting from a modelocked laser in the near-infrared (near-IR) region (typically a Ti:sapphire modelocked laser with a central wavelength of 780 nm) the harmonic spectrum extends to the vacuum ultraviolet (VUV) or even the extreme ultraviolet region (XUV). The emitted radiation is coherent, has a limited divergence angle (usually between 2 mrad to 12 mrad) and a defined polarization state. Figure 1.2 depicts a typical spectrum produced by HHG in a gas, where three regions can be identified. The intensity of the first harmonics is quickly decreasing in the perturbative regime, harmonics have a constant intensity in the plateau regime until the cut-off regime is met, where the intensity of the higher order harmonics decreases dramatically.

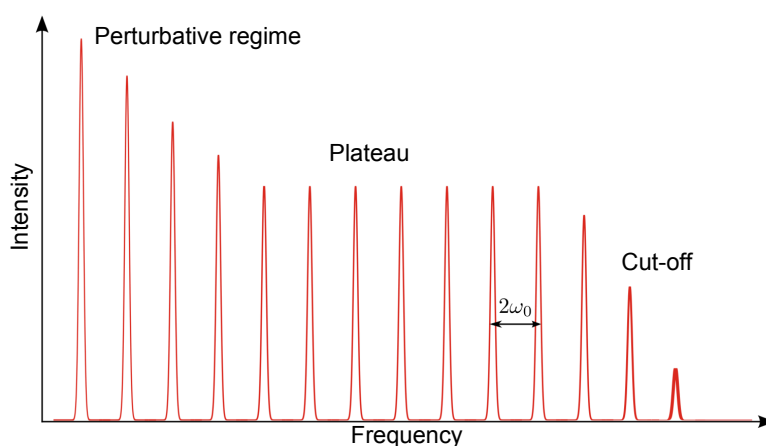


Figure 1.2: Illustration of the typical structure of the HHG spectrum generated in a gas. Only odd harmonics are generated, which are separated by two times the fundamental frequency of the laser (ω_0).

The HHG process can be understood simply from a basic semi-classical model: the three-step model (see Figure 1.3) [5,6].

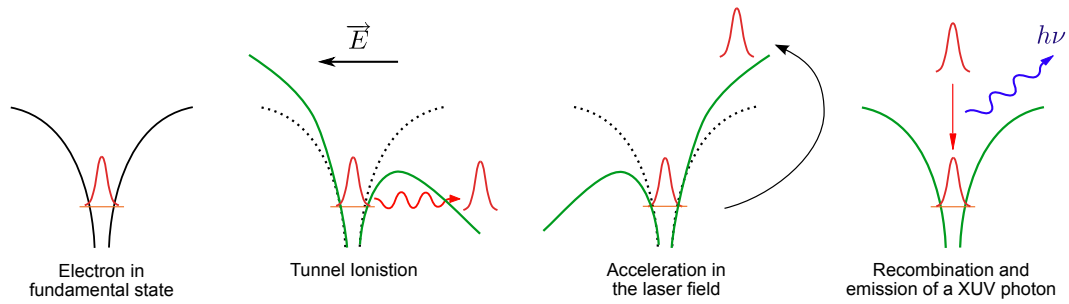


Figure 1.3: The three-step model of HHG (picture from [7]).

Starting from an electron in the fundamental state, where it is trapped in the Coulomb potential, the intense electric field of the laser pulse lowers the potential down enough to allow the electron crossing it by the tunnel effect. The electron is then accelerated in the laser electric field and, once the sign of the electric field is inverted, it comes back to its parent ion. During recombination, the atom releases the acquired kinetic energy in the form of an emitted XUV photon.

From this model, a few interesting remarks can be made: the strength of the electric field needed to lower the Coulomb potential depends on the ionization potential I_p which depends on the chemical species used as generation medium. Xenon has one of the lowest ionization potentials among gases and can thus produce HHG more easily.

XUV light produced by HHG finds numerous applications, in particular in spectroscopy. Indeed, it is possible to extract structural and dynamical information of the emitting medium directly from the properties of the harmonic radiations. By decoding the XUV spectrum emitted by HHG, the molecular orbital of nitrogen was imaged for the first time in [8]. The rearrangement dynamics of electrons during ionization was also studied through the phase of the HHG radiation [9]. The polarization state of the HHG radiation also contains important information concerning molecular alignment and structure [10]. Thus, many advances as well as fundamental questions were answered using HHG-based XUV light. However, due to the need for high intensities, initial HHG sources only operated at low repetition rates in the kHz regime. In order to reduce the measurement time and increase the signal-to-noise ratio in many measurements, an important research direction is the development of simple and efficient MHz HHG sources.

The work carried out in this thesis addresses two main research areas: narrow linewidth mid-IR laser sources for spectroscopy and the development of ultrafast solid-state lasers for HHG at MHz repetition rates.

The content of this thesis is organized as follows:

Chapter 2 describes the different steps toward the implementation of a narrow linewidth and high-power 3- μm source based on difference frequency generation inside an enhancement cavity driven by two cw lasers amplified in high-power fiber amplifiers. The frequency noise of the generated 3- μm radiation is estimated by measuring the noise of the semiconductor laser diodes that seed the system as well as the additive noise of the remaining part of the setup.

Chapter 3 presents the first realization of HHG inside a modelocked thin-disk laser. Different gain materials and cavities have been tested for high intracavity peak powers inside modelocked thin-disk oscillators. The laser cavity is placed inside a vacuum chamber and, with the creation of a tight focus extension of the cavity, the optical intensity is high enough to generate high harmonics.

Chapter 4 concludes the thesis and provides an outlook on future improvements, developments and applications of the presented experiments.

Chapter 2

Continuous-wave difference frequency generation inside an enhancement cavity

Introduction

The mid-infrared (mid-IR) spectrum (wavelengths from 3 μm to 20 μm) is commonly called “the molecular fingerprint” region as numerous molecules have their strong fundamental ro-vibrational transitions in this spectral range. A large variety of applications of mid-IR sources are dedicated to spectroscopy in fields like environmental monitoring of atmospheric gases and pollutants, industrial process control (e.g., in the semiconductor industry) [11,12] or medical diagnosis with exhaled breath monitoring [13–16]. Mid-IR sources also find applications in the security and military fields with explosives detection or optical countermeasures [17] or for the ablation of polymers [18–20] in industry.

In this chapter, a continuous-wave (cw) difference-frequency generation (DFG) source emitting at 3 μm seeded by two single-mode laser diodes operating at 1 μm and 1.5 μm , respectively, and amplified in dedicated high-power fiber amplifiers is presented. In a first proof-of-principle experiment for evaluation of the noise and linewidth of the generated 3- μm radiation, up to 120 mW are generated using a seed power of 10 W at 1 μm and 2.3 W at 1.5 μm that is further enhanced using a

resonant cavity for the 1.5- μm light. While this experiment was limited by the coating losses of the crystal and the thermal effects in the crystal, the concept of combining an enhancement cavity with a bulk periodically-poled lithium niobate (PPLN) crystal should allow for output power in the 1 - 10 W regime. This approach is in principle comparable to a cw-seeded optical parametric oscillator (OPO), however it is not required that the generated 1.5- μm power is higher than the introduced losses. Compared to OPO, no significant increase in the linewidth is expected. Compared to direct single-pass DFG in PPLN waveguides, this approach should enable higher output power levels.

The excess frequency noise introduced by the different parts of the experimental setup, i.e., by the fiber amplifiers, the 1.5- μm resonant cavity, etc. is studied in detail. The overall excess frequency noise of the generated 3- μm DFG radiation was assessed by building a second DFG source seeded by the same laser diodes, but operated in a single-pass configuration and with the use of independent fiber amplifiers, and by implementing a beat note between the two DFG radiations.

This chapter presents the different parts and steps towards the implementation and characterization of the 3- μm DFG-based source. In Section 2.1, the high-power fiber amplifiers are presented and studied. They deliver enough power to seed the DFG setup. Section 2.2 focuses on the DFG process inside a non-linear crystal and a single-pass DFG experiment is presented. Section 2.3 deals with the enhancement cavity built around the non-linear crystal, resonating at 1.5 μm , and with the performance of the setup generating powerful 3- μm radiation. In Section 2.4, the additive frequency noise of the setup is evaluated with the use of a second DFG-based mid-IR source allowing an estimation of the noise properties of the generated 3- μm light.

Overview of mid-IR sources

The large range of previously mentioned applications sets a large panel of requirements for the considered mid-IR sources. Depending on the application, the laser sources need to be narrow linewidth, continuously tunable, powerful enough, compact, robust, and preferably to operate at room temperature. In this section, continuous-wave mid-IR sources are reviewed.

Many mid-IR laser sources have been developed to address most of those requirements. But each technology displays advantages and drawbacks. For example, color center lasers operate between 2 and 3.5 μm

with watt power levels and MHz linewidth in continuous-wave operation [21]. But cryogenic cooling is required for stable operation, which strongly limits the robustness and the compactness of those lasers. CO and CO₂ lasers emit in the range of 5 - 6 μm and 9 - 11 μm , respectively, with high output powers (several watts). However, their tunability is intrinsically limited by the discrete gas emission lines, which can be partially overcome with high gas pressure operation. Those lasers are still commonly used for gas sensing applications, especially in industry (diagnosis of gases in semiconductor industry [22]), but within the range of the limited tunability. Semiconductor lasers like quantum cascade lasers (QCLs) [23,24] or interband cascade lasers (ICLs) [25] can emit power levels of a few hundreds of mW up to watts. The main advantage of such devices is that they can be designed to emit in a range of 3 - 25 μm and 2 - 6 μm , respectively, in continuous-wave operation, needing, nevertheless, an additional external cavity or DFB grating to operate in longitudinal single mode. Those lasers are compact, robust and the years of development made them work now at room temperature. QCLs are now a reference device for sensing applications [26].

Taking advantage of the development of lasers in the near-infrared region, mid-IR sources based on frequency conversion processes can fulfil most of the previously cited requirements. The most common frequency conversion processes used for mid-IR sources for high-resolution spectroscopy are based on OPO and DFG. Both processes are based on frequency conversion inside a nonlinear crystal using the exact same energy level scheme. Hence, their tunability is fundamentally the same. OPOs demonstrated several tens of watts of output power and a large tunability (typically from 2.4 μm to 4.3 μm for the idler wavelength) [27-31]. Sub-kilohertz linewidth of an OPO was achieved through pump frequency stabilization over the comparison of the idler signal with a narrow absorption line from a gas cell [32,33]. If OPOs display a quite large number of advantages, they can show a high degree of complexity due to the required active cavity stabilization. DFG, on the other hand, can work with a single pass scheme that reduces the complexity of the experimental setup. DFG works within a large range of wavelength (2 μm - 15 μm), with the capability of continuous tuning. Narrow linewidth sources are commonly used for high precision spectroscopy. However, the poor efficiency of cw DFG in bulk crystals makes high-power sources difficult to achieve. Watts of single-pass DFG power have been demonstrated using high power fiber lasers with approximatively 40 W of pump and signal power each [34]. High efficiencies are achievable by use of nonlinear crystals which also act as waveguides. However, the limited mode area and surface damage makes it challenging to operate these sources at the 1 - 10 W regime.

Compared to visible or near-infrared (NIR) lasers, mid-IR sources are generally less advanced in terms of low-noise and narrow linewidth operation, even though a QCL with Hz-level linewidth has been demonstrated by phase-locking to an ultra-stable NIR laser using a sum-frequency generation process with a femtosecond frequency comb [26]. Consequently, characterization tools and instrumentation to assess the laser frequency noise and linewidth properties are also less developed in the mid-IR. A commonly used method to measure the frequency noise of mid-IR laser sources and to retrieve their corresponding full-width at half maximum (FWHM) linewidth involves an optical frequency discriminator that converts the frequency fluctuations of the laser into intensity fluctuations that are measured by a photodiode. The discriminators can be a narrow molecular transition [35] or a resonance of a Fabry-Perot cavity [36]. These methods circumvent the need for a lower noise and more stable reference laser for comparison by heterodyne beating that is frequently used in the NIR, where such sources are more common.

2.1 High power fiber amplifiers

2.1.1 Basics of fiber amplifiers

Difference frequency generation in bulk crystals is a low-efficiency nonlinear process with a typical conversion efficiency of several hundreds of $\mu\text{W}\cdot\text{W}^{-2}\cdot\text{cm}^{-1}$ in continuous-wave operation ($\eta = 528.9 \mu\text{W}\cdot\text{W}^{-2}\cdot\text{cm}^{-1}$ reported in [34] as one of the highest single-pass efficiencies). For most applications, a few mW of 3- μm power level is highly desirable, which implies a few watts of power from both 1560 nm (signal) and 1030 nm (pump) sources. At each wavelength, erbium- or ytterbium-doped fiber-based amplifiers can provide a few watts of output power from milliwatt-level seed sources. Erbium- and ytterbium-doped fiber amplifiers are commonly used already for a few decades [37], they display typical advantages from a proven technology such as a relative low-cost and the accessibility of their components. Moreover, connectorized amplifiers feature the possibility to easily exchange the seed source which proves, in practice, to be very convenient.

2.1.1.1 Erbium-doped fiber amplifiers

Optical telecommunications have pushed the development of fiber technologies. For pure silica single-mode fibers, the lowest attenuation is located at 1.55 μm , which led to the early development of material and sources in this wavelength range. Since its ions display an atomic transition at 1.55 μm , erbium is a dopant of first interest for the emission and amplification of telecom signals. Erbium-doped fibers have benefited from decades of development, resulting in erbium-doped fiber amplifiers being the most commonly used type of optical amplifier.

The erbium ion Er^{3+} displays convenient energetic transitions for stimulated emission at 1.55 μm (see Figure 2.1) with possible pumping wavelengths of 980 nm and 1480 nm. Thanks to the availability of efficient and reliable pump diodes, the pumping transition at 980 nm is more often used.

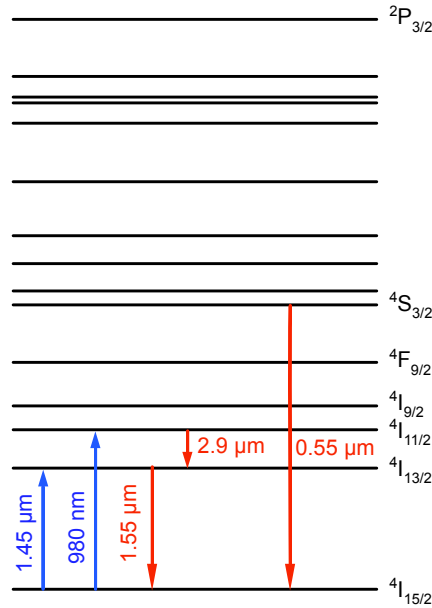


Figure 2.1: Energy levels of the erbium ion in silicate glass.

The erbium ions are placed into a glass host (phosphate glass can be used for a better transmission level) and manufactured as an active doped fiber. When placed in an amorphous silica host, Er^{3+} displays a large gain bandwidth (see Figure 2.2). The typical doping concentration is about $14.6 \cdot 10^{24}$ ions/ m^3 for erbium-doped fibers which constitute the gain medium in fiber lasers as well as in fiber amplifiers. In this work, erbium-doped fiber amplifiers (EDFAs) are pumped with 980-nm semiconductor laser diodes. In single-cladding fiber geometry, the pump is single-mode (transverse), and co-propagates with the 1550-nm signal through the fiber core for an efficient absorption in the gain medium.

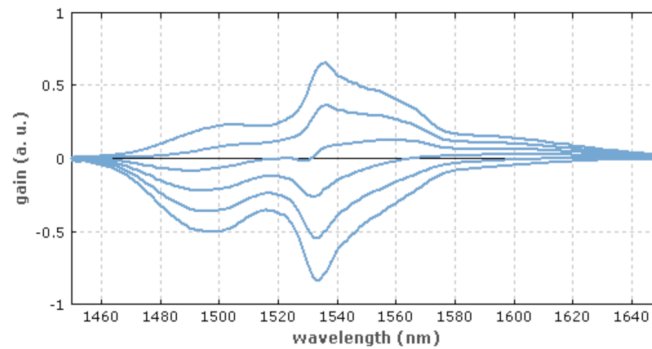


Figure 2.2: Gain spectrum of erbium (Er^{3+}) ions in phosphate glass for excitation levels ranging from 0 to 100% in steps of 20%, from RP Photonic website [38].

In the classical scheme, depicted in Figure 2.3, an EDFA (single-clad polarization-maintaining (PM) fiber) is composed of the following elements: the signal (also called the seed, $\lambda = 1550$ nm) is sent through a passive fiber, passes by a fiber-coupled optical isolator and a combiner before being amplified into the erbium-doped single-clad fiber. The amplifier ends with another fiber-coupled isolator, as well as a pump coupler (not used in this work). The role of the isolators is to prevent any backward propagating light to get out of the amplifier towards the seed laser (input isolator) and to prevent any back reflections, from after the amplifier, to reach the doped fiber (output isolator). Indeed, optical fiber amplifiers are sensitive to back-reflections. In the case of small back reflections reaching the end of the doped fiber, the backward small signal would be amplified, depleting the gain and then perturbing the amplification of the original signal. If the seed diode is not protected by an isolator, this backward amplified signal can severely damage the diode. The combiner, a wavelength-division multiplexer (WDM), mixes the pump and the signal into one fiber, to which the erbium-doped fiber is spliced. A large number of doped fibers with various doping concentrations, core diameters, etc. are available from different manufacturers and a suitable one is chosen according to the needs of the experiment (e.g., transverse single-mode propagation at signal wavelength, PM fiber and signal mode-field diameters matching between the different elements of the EDFA).

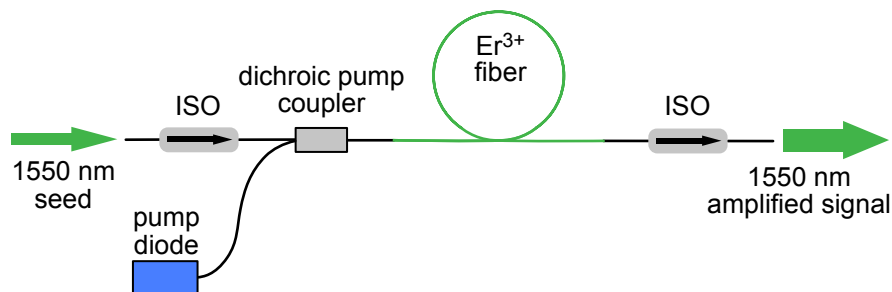


Figure 2.3: Typical setup of an EDFA. ISO: isolator.

2.1.1.2 Ytterbium-doped fiber amplifier

The difference between EDFAs and ytterbium-doped fiber amplifiers (YDFAs) is basically the doping ion used for amplification, and thus the operating wavelength. All the other aspects of fiber amplifiers discussed before are common for both and are thus not repeated here.

The ytterbium ion is a rare-earth metal, it features some convenient properties making it a first-choice dopant for emission or amplification at $1 \mu\text{m}$. Owing to their simple energy levels structure, their small quantum defect, small quantity of impurities in the medium, their large gain

bandwidth, ytterbium-doped gain media have a long track of use in free-space lasers and in fibers lasers and amplifiers [39], thus benefiting from a long and proven technology development. High quality crystals are now commercially available as well as high quality doped fibers.

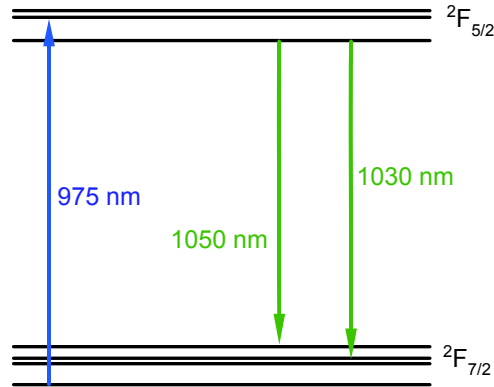


Figure 2.4: Energy levels of ytterbium ions in YAG host.

Because of its quasi three-level behavior (see Figure 2.4), the ytterbium-doped gain medium requires high pump intensity for population inversion. Pumping can be achieved at 910 nm (see Figure 2.5) as well as at 975 nm. The zero-phonon line (at 975 nm) requires narrow linewidth pumping and the reachable excitation level is mitigated by the stimulated emission. The maximum of the emission cross section is located at 1030 nm, but laser emission can occur up to 1080 nm. Therefore, switching from 1030 nm to 1064 nm seed source has small effect on the YDFA performance.

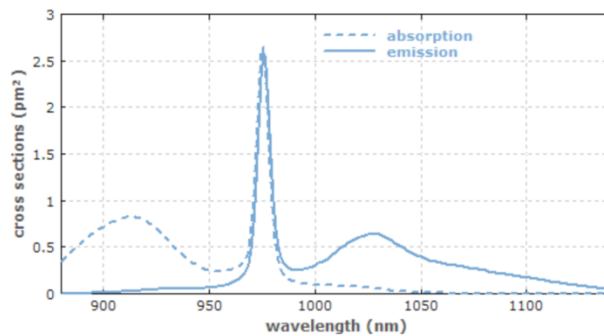


Figure 2.5: Absorption and emission spectra of ytterbium-doped germanosilicate glass (typically composing ytterbium doped-fiber core). Figure from RP photonic website [40].

The classical scheme of YDFAs is, in all point, the same as for EDFAs, except for the doped fiber.

2.1.1.3 High power fiber amplifiers

The amplifiers described before are restricted to single-clad geometry and are thus limited in terms of achievable pump level. Indeed, with the pump traveling into the fiber core, a transverse single-mode pump is required for a good overlap with the seed signal. The pump can reach high intensities in the fiber core and is thus limited by the fiber damage threshold. In addition, high-power single-mode pump diodes are challenging to produce and thus expensive in comparison with multimode pump diodes. To overcome those limitations, a fiber with an additional cladding in which the pump is traveling is used. The cladding usually supports higher-order mode propagation while the core remains a single-mode fiber. The outer cladding is often made of polymers (cheaper than glass and less sensitive to shocks). If double-clad (DC) fibers allow high pump power levels thanks to a larger area for mode propagation, the overlap with the seed signal is reduced compared to single-clad doped fibers. Nevertheless, the length of the fiber combined with high pump power levels allows for high power amplification. Already more than 1 kW has been reached at 1080 nm with an M^2 value of 1.4 [41] using a double-clad fiber amplifier. In our case, high-power amplifiers based on double-clad fibers are placed after the single-mode fiber amplifiers to reach the watt level.

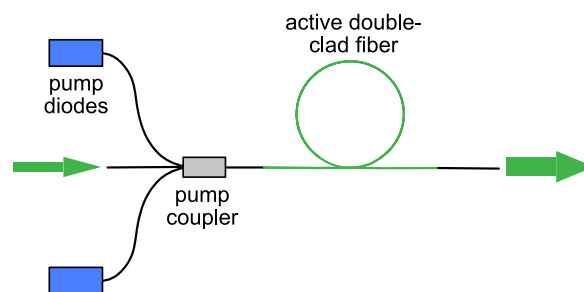


Figure 2.6: High power amplifier pumped by multimode pump diodes coupled into the double-clad fiber through the multimode pump combiner.

The scheme of high-power fiber amplifiers is close to the single-mode fiber amplifiers as depicted in Figure 2.6. The multimode pumps are coupled into the double-clad fiber using a multi-mode pump combiner (MPC). This component fuses many multimode fibers into the cladding of the double-clad passive fiber enabling high pump power operation. In this work, only forward pumping is used and thus depicted in the scheme of principle in Figure 2.6, but backward pumping is also an option for other cases.

In this work, high power fiber amplifiers constitute the last stage of amplification for both 1- μm and 1.5- μm amplification lines. For the amplification at 1.5 μm , a co-doped erbium-ytterbium double-clad fiber is used. The pump at 980 nm is more easily absorbed by the ytterbium ions, which transfer their energy to the erbium ions, thus enhancing the pumping efficiency.

2.1.2 Design and experiment

In fiber amplification, many physical processes occur either participating to the amplification of the signal or degrading it. Two important examples of those processes are the amplified spontaneous emission (ASE) and the stimulated Brillouin scattering (SBS).

Spontaneous emission is, in most cases, an undesirable effect that occurs in gain media. Atoms (or ions) of the gain medium are pumped to a higher energy level and, depending on their lifetime, spontaneously return to a lower level by emitting a photon. This luminescence is usually considered as noise. In a pumped doped fiber, photons from spontaneous emission propagate along the fiber and are amplified by stimulated emission and, in the two directions, forward and backward. This phenomenon is called Amplified Spontaneous Emission (ASE) in fibers. In a fiber amplifier, ASE is unavoidable and takes the form of parasitic light emission in both directions contributing to the noise of the amplifier. To keep its level as low as possible, many solutions are available: the first one consists of an optimized design of the amplifier, depending on the input seed level and on the pumping level to reduce the generation of ASE. Enclosing the fiber amplifier by two isolators increases the signal-to-ASE power ratio of the out-coupled light. Finally, inserting an optical filter tuned to the seed wavelength at the the amplifier output confines most of the ASE inside the amplifier as its spectral bandwidth is much larger than the amplified signal linewidth.

Stimulated Brillouin scattering (SBS) originates from Brillouin scattering where a backscattered optical wave and an oscillation of the medium with an acoustic frequency (a phonon) are created during the propagation of light in a medium. This nonlinear effect is particularly visible in fibers as its efficiency depends on the light intensity. The backscattered wave has its frequency downshifted (by 10 - 20 GHz) compared to the propagating light (Stokes wave). Owing to a physical effect called electrostriction, Brillouin scattering is further amplified. Indeed, due to the interference pattern created by the forward and backward

propagating light, the medium density is periodically modified, creating a Bragg grating, enhancing the reflected Stokes wave, resulting in stronger interferences [42]. This effect is called SBS, it is particularly present for narrow linewidth continuous-wave radiation with its high-power spectral density at the laser frequency. In fiber amplifiers, high levels of SBS can lead to strong pump depletion and chaotic power fluctuations thus limiting the achievable amplified power. SBS effects can be prevented with a suitable fiber amplifier design: long fibers tend to favour SBS, thus for a given pump and signal powers, the fiber length is optimized such that the SBS power remains low.

In order to make a proper design of the fiber amplifiers, the commercially available software RP Fiber Power (RP Photonics) was used. It proposes an efficient power propagation as well as a numerical beam propagation. The other physical effects that limit the amplification, such as SBS and ASE, are also evaluated.

2.1.2.1 1.5- μm amplification

The laser source is a fiber-coupled 14-pins butterfly semiconductor diode (Eblana-photonics EP1560-0-NLW). The diode mount (LM14S2 Thorlabs) allows temperature control and current adjustment of the chip combined with a temperature controller (TED200C Thorlabs) and a low-noise current driver (Koheron DRV 200). When stabilized at 35 °C and supplied with 300 mA the diode delivers 9 mW at 1560 nm. Using the elements presented in subsection 2.1.1, an amplifier system composed of multiple stages was designed. Aiming for tens of watts of output power at 1560 nm, the amplifier design started with the last stage of amplification using a double-clad doped fiber. The pump power available from multimode semiconductor diodes at 980 nm is about 50 W. Double-clad fibers with Er- and Yb-co-doped core supporting single-mode propagation at 1560 nm are not numerous on the market. For its high doping concentration and the long record of quality fibers produced by the supplier, the DCF-EY-10/128-PM fiber from Coractive was chosen. The fiber specifications given by the supplier and summarized in Table 2.1 were used in the simulations.

The goal of the simulations was to evaluate the optimal fiber length for a given input seed power while checking that the ASE and SBS powers remain sufficiently low. Figure 2.7 shows the evolution of the pump and signal power along the fiber for an input seed power of 400 mW, a pump power of 50 W and a total fiber length of 4.3 m.

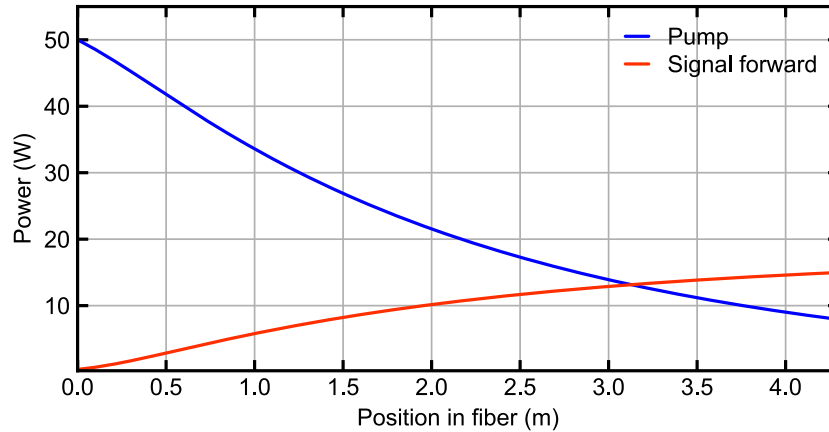


Figure 2.7: Evolution of the pump (at 980 nm, in blue) and signal (at 1560 nm, in red) powers along the double-clad fiber. The fiber length is set to 4.3 m.

Up to 15 W of amplified signal power are predicted directly out of the DC fiber, as well as 7.9 W of unabsorbed pump.

The SBS and the forward and backward ASE total powers were calculated in the script but are not shown on the graphics. In this case, 1.3 W of SBS is predicted. The ASE in backward and forward direction was simulated as well but the script showed difficulties in handling it properly, most probably because of the co-doped core. The given values are 50 μ W for forward ASE and 276 μ W of backward ASE power.

Increasing the fiber length would allow achieving higher signal power with less pump power out of the DC fiber. However, the SBS power would increase dramatically resulting in a high risk of damaging components before the amplifier (e.g., the isolator). For example, a fiber length of 4.5 m would lead to 10 W of SBS power instead of 1.3 W.

Decreasing the input seed power would slightly release the constraint for the amplification stage before the DC fiber, but would result in a strong increase of the ASE: with 100 mW of input seed power, 1.5 mW of backward ASE power is predicted instead of 276 μ W (although the values are not reliable, the trend can be trusted).

To couple around 400 mW of signal power into the last stage amplifier from a 9-mW laser seed diode, another amplifier was designed and set in between. This amplification stage is referred to as the pre-amplification stage (or the pre-amplifier). Considering the involved power levels, a single-clad doped fiber is enough for an efficient amplification and an Er35-7PM fiber from Coractive was chosen. In contrast to the previously described DC fiber, the supplier did not provide all specifications of this

active fiber and assumptions concerning many parameters like the doping concentration or the upper-state lifetime were made as listed in Table 2.1. Using a 600-mW pump diode and 7 mW of input power (an isolator is placed between the seed diode and the Er-doped fiber) simulations predict that with a fiber length of 2.6 m, up to 375 mW of signal can be obtained with only 1 mW of remaining pump power (see Figure 2.8).

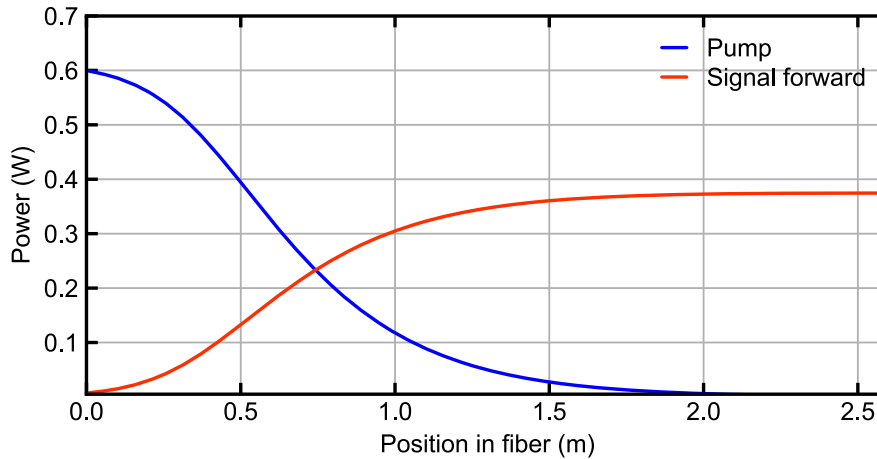


Figure 2.8: Signal (in blue) and pump (in red) powers along the fiber length for 2.6 m of Er-doped single-clad fiber with an input power of 7 mW.

The SBS is not significant for such power levels, with 14 pW of predicted power. The ASE displays a relatively flat spectrum (see Figure 2.9) and a low level in both directions: 377 μ W of backward power and 54 μ W of forward power. During the experiments, the seed diode might be changed, or optical elements might be inserted (like an acousto-optic modulators AOM) before the active doped fiber, reducing the input signal power coupled to the amplifier. Figure 2.10 shows the evolution of the output signal power level and the ASE powers (in both directions) for different input power levels. The input power could be, in principle, reduced to 1 mW, while the system performances would remain quite similar: a low level of ASE and an output power level of approximately 370 mW.

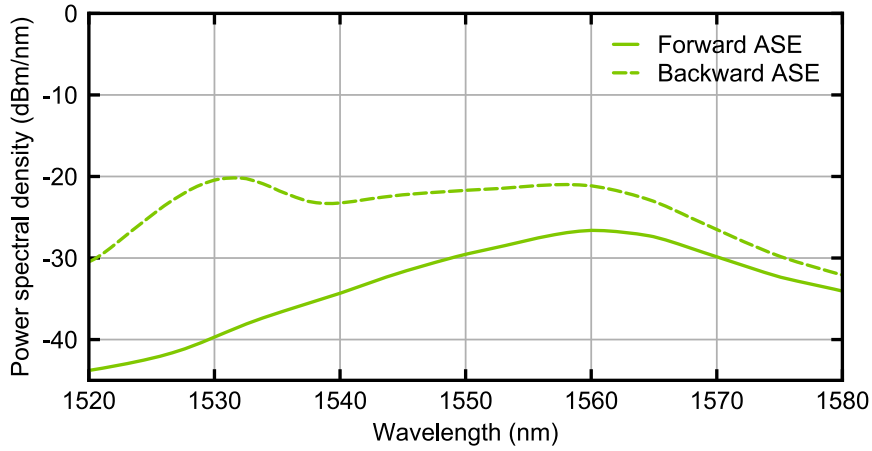


Figure 2.9: ASE power spectral density around the signal wavelength (1560 nm) for 2.6 m of Er-doped single-clad fiber, pumped by 600 mW at 980 nm and emitting 375 mW of signal at 1560 nm with an input power of 7 mW.

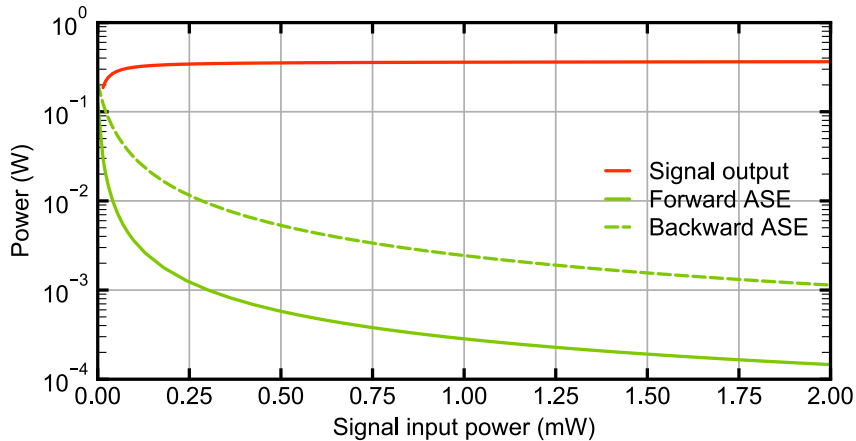


Figure 2.10: ASE powers (in both directions, in green) and signal output power (in red) for different input power levels for 2.6 m of Er-doped single-clad fiber, pumped by 600 mW at 980 nm and emitting 375 mW of signal at 1560 nm.

The power level calculated from these simulations is enough to seed the last stage amplifier. However, in the experiment, the pre-amplifier power level is measured to be only 200 mW instead of the simulated 375 mW of signal. Most likely, this difference is due to higher losses of the

isolators and the WDM than assumed in the simulations, or to differences in the used fiber parameters.

To counterbalance the low power, a second pre-amplifier has been built after the first one. The design is essentially the same, except for the fiber length which is reduced to 2 m thanks to the high input seed signal power, using the same doped fiber but to reach higher signal power, a 1-W pump diode is used.

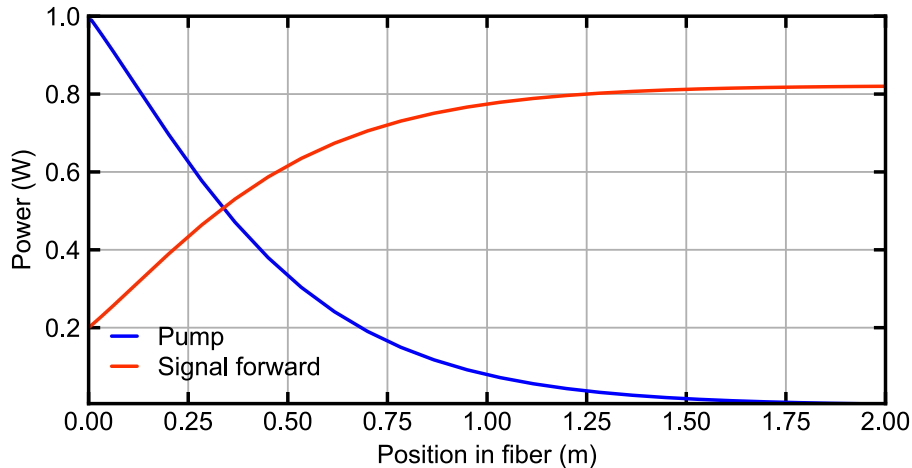


Figure 2.11: Signal (in red) and pump (in blue) powers along the fiber length for 2 m of Er-doped single-clad fiber with an input power of 200 mW.

Up to 820 mW of signal power is predicted with an input power of 200 mW, with 4 mW of pump remaining at the end of the doped-fiber (see Figure 2.11). The SBS remains at a negligible power level: 30 pW of power as well as the ASE in both directions: 12 μ W of forward power and 26 μ W of backward power.

In the experiment, like for the previous comparison with simulations, the power level is lower than the predicted value: up to 500 mW is measured directly out of the active fiber. Again, the difference might originate from non-accurate parameters for losses or describing the fiber.

	1- μm amplifier	1.5- μm amplifier
Pre-amplification stage		1 st part / 2 nd part
Fiber denomination	Yb401-PM	Er35-7-PM
Fiber length (m)	0.64	2.6 / 2
Core diameter (μm)	5	5
Ion doping	Yb	Er
Doping concentration (assumption) (ion/ m^3)	8×10^{25}	24.6×10^{24}
Absorption (dB/m)	7.7 @1200nm	37.9 @1530nm
Last amplification stage		
Fiber denomination	Yb1200- 10/125DC-PM	DC-EY-10/128-PM
Fiber length (m)	1.9	4.3
Core diameter (μm)	10	10
Cladding diameter (μm)	125	128
Ion doping	Yb	Er / Yb
Doping concentration (assumption) (ion/ m^3)	9×10^{25}	43×10^{24} (Er) 2.2×10^{24} (Yb)
Absorption (dB/m)	7.7 @976nm	1.97 @915nm

Table 2.1: Fiber parameters for 1- μm and 1.5- μm fiber amplifier simulations. Data from fiber specifications provided by the supplier.

Nevertheless, the goal of 400 mW at the entrance of the last stage amplifier is reached in this configuration. The next paragraph sums up the entire amplification system and focuses on the last stage fiber amplifier design and performances as well as the trouble-shooting of the encountered problems.

The overall amplification system is shown in Figure 2.12. The seed signal originates from a 9-mW semiconductor diode emitting at a wavelength of 1560 nm in single-mode operation. It is then amplified in two stages of SC Er-doped fiber (Coractive Er35-7 PM) with gain segments of 2.6 m and 2 m, respectively. Using two single-mode fiber Bragg grating

(FBG) stabilized pump diodes with a respective maximum power of 600 mW and 1 W at 980 nm, the signal is first amplified up to 400 mW. Then it passes through a 1550-nm/1030-nm WDM, to extract the backward propagating ASE at 1030 nm, generated in the following Er-Yb amplification stage. The last amplification stage consists of 4.3 m of DC Er-Yb co-doped fiber (Coractive DCF-EY-10/128-PM, 10 μ m core diameter) and is pumped up to a power of 15 W at 976 nm. A 5-cm long 10 degrees angle-cleaved SC fiber (PM 1550) is spliced to the DC gain fiber for transverse mode cleaning. The outcoupled beam is collimated using an aspheric lens with a focal length of 8 mm and passes through a half waveplate and a high-power isolator. After isolation, 4 W of amplified power are measured at 1560 nm.

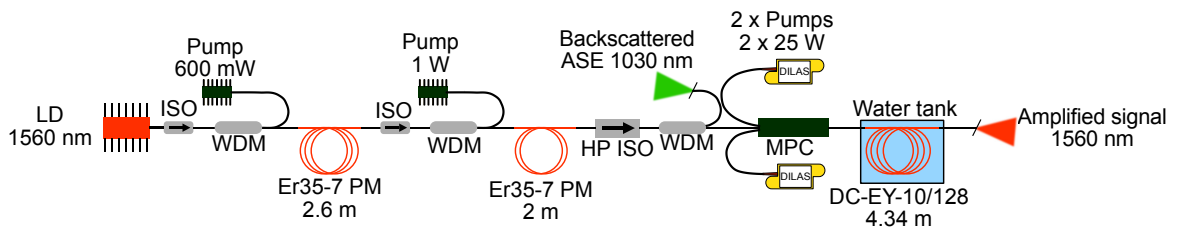


Figure 2.12: Scheme of the amplification stages at 1560 nm. LD: laser diode, ISO: isolator, WDM: filter-based wavelength-division multiplexer used in reflection, HP ISO: high power isolator, MPC: multimode pump combiner.

Since high-power fiber lasers can reach the kilowatt level in single mode operation, the thermal management of DC fibers has been well studied [43]. In a first configuration, the fiber was rolled around a home-designed aluminum rod with grooves maintaining the fiber and assuring (a priori) a proper heat extraction. But with around 15 W of pump power and 5.5 W of signal power, the fiber was damaged. For a better heat management, the Er-Yb double-clad fiber was placed in a water tank. Indeed, water offers a uniform thermal heat removal with a high thermal capacity. In this configuration, no fiber damage was observed, the pump power could be increased up to 14.6 W and 4.7 W of cw radiation at 1560 nm was obtained (see Figure 2.13). When the power was further increased, the next point of the power slope was slightly below the linear trend. The same behavior was also noticed just before the fiber was previously damaged. For a safe operation, the pump power was kept under 12 W and the output power was thus limited to 4 W at maximum for the experiments reported in the next sections.

With a thermal camera, a very high and unusual temperature of the high-power isolator was observed. Suspecting some backward ASE, a WDM was spliced to extract the backward radiation around 1 μm . For 3 W of amplified signal at 1560 nm, up to 500 mW of ASE at 1030 nm was shining on the isolator, heating it up and thus reducing its transmission.

Directly out of the DC fiber, once the remaining pump is removed (removal of the fiber second cladding and coated with high index glue), some higher order modes were still present in the beam. In a first design for pump extraction at the end of the DC fiber, the polymer coating was removed, and the uncoated part of the fiber was directly glued onto a metallic piece (aluminum in this case) covered with a thin graphite sheet used as heat sink (design used for the single-pass DFG experiment, with results reported in subsection 2.2.2.4). The junction between the coated and uncoated fiber parts was set with low index glue at the center of the heat sink for maximum heat removal. But occasionally, the junction ignited, setting fire to the polymer coating of the DC fiber. To solve those two problems, a 5-cm long PM 1550 fiber was spliced at the end of the DC fiber (and angle-cleaved on the other side) to filter-out the higher order modes.

The splicing point as well as the coated/uncoated junction of the DC fiber were glued onto a water-cooled copper-based graphite-covered heat sink. The water-cooled piece of metal was home-designed and manufactured at the university workshop. No more fiber ignition was observed since then and the output transverse mode was clean and single-mode.

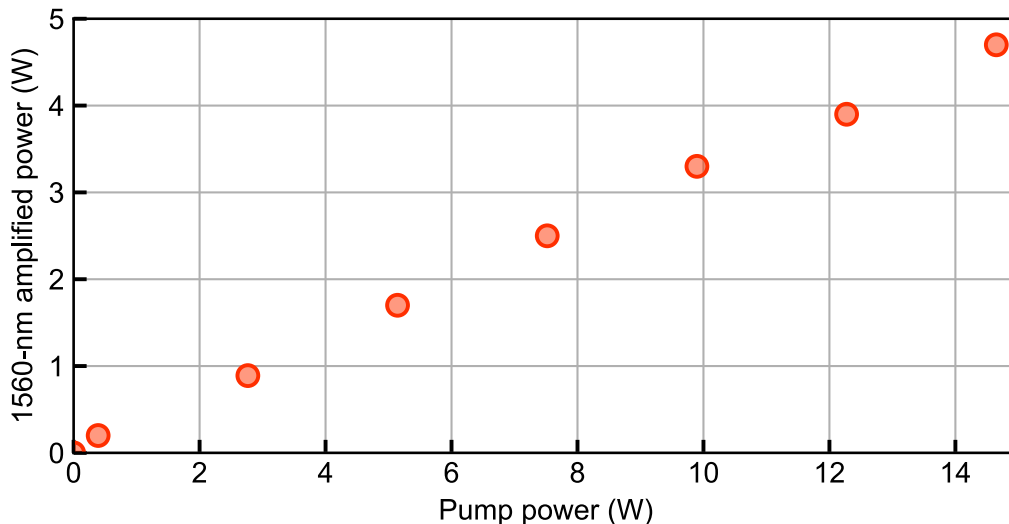


Figure 2.13: Power slope of the last fiber amplifier stage at 1560 nm. Initial input power: 400 mW. The slope efficiency is $\eta = 32\%$.

2.1.2.2 1- μm amplification

The design of the 1- μm amplification system was achieved using a similar scheme and script as for the 1.5- μm amplifier. Simulations match quite well the measurements for Yb-doped fiber and the ASE and SBS levels are predicted low.

At 1 μm , the amplifier is also seeded by a fiber coupled 14-pins butterfly distributed feedback (DFB) semiconductor diode (QDLaser QLD1061-3030). The chip is mounted in an all-included laser driver module (OptoSci LDR1500E) including temperature controller and current driver that are computer-controlled. When stabilized at 25 °C, the diode delivers 55 mW of 1030-nm light at a current of 200 mA. It was initially amplified to 400 mW, using 1 W of pump light, in a 64-cm long single clad (SC) Yb-doped fiber (Coractive Yb 401-PM) amplifier. Fiber coupled isolators were placed between the seed source and the following amplification stages. The pre-amplified signal was power-amplified in a 1.9-m long double clad (DC) fiber (Liekki Yb 1200-10/125DC-PM, 10 μm core diameter) that was pumped by volume Bragg grating (VBG) stabilized fiber-coupled laser diodes at 976 nm with a total power up to 45 W. The fiber length was optimized to minimize SBS while maximizing the amplification factor. The end tip of the gain fiber was spliced to a 20-cm long SC fiber (PM980) to filter out higher-order modes and clean the transverse mode of the laser radiation. As for the 1.5- μm amplifier, the splice point was glued onto a water-cooled copper block using a high-index epoxy to extract and prevent the excess pump from reaching the fiber tip and causing thermal issues. The fiber tip was cleaved at an angle of 10 degrees and glued onto an aluminum block. The output beam is collimated using an aspheric lens with a focal length of 11 mm.

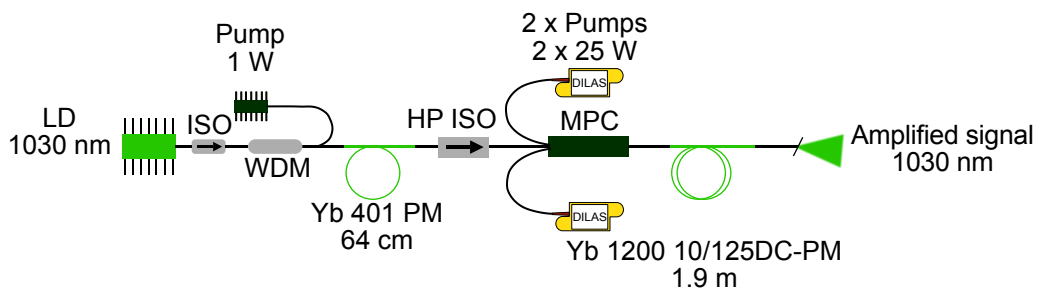


Figure 2.14: Fiber amplification system at 1030 nm. LD: laser diode, ISO: isolator, WDM: wavelength division multiplexer used in reflection, HP ISO: high power isolator, MPC: multimode pump combiner.

As for the 1.5- μm amplifier, problems of coating ignition and higher-order modes appeared and were solved in the same way. However, no thermal management problems along the fiber appeared, and the first design with a home-made aluminum cylinder with grooves was kept for the following experiments. As a result of the high ytterbium absorption at 980 nm only a short fiber length is enough to reach high power.

As no problems of ASE were observed, the full pump power capacity could be used, and up to 29.6 W of amplified signal at 1030 nm was measured with 45 W of pump power (see Figure 2.15).

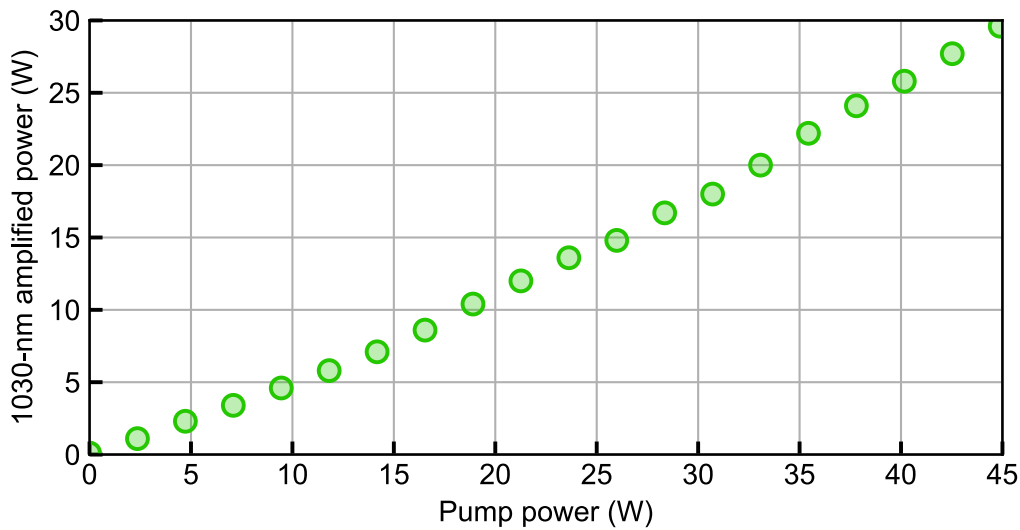


Figure 2.15: 1030-nm fiber amplifier power slope. Input power: 330 mW; doped-fiber length: 1.9 m. The slope efficiency is $\eta = 62\%$.

In conclusion to this section, two high-power fiber amplifiers delivering respectively up to 4 W at 1560 nm and 30 W at 1030 nm have been presented. Some issues like thermal management of the pump out-coupling and a remaining multimode operation as well as backward ASE were solved with design modifications. However, after passing through a half wave plate and an optical high-power isolator, the optical power at both wavelengths was unstable over time (variation of about 10 % at the highest power operation). This power instability seemed, among other reasons, to originate from polarization instabilities. For both lines, all the fibers of the amplifiers are PM, thus the linear polarization of the light out of the seed laser diodes should be preserved [44]. However, the birefringence of PM fibers could be modified with mechanical stress or with temperature variation, and in the case of high-power fiber amplifier where

thermal management is possibly an issue, precise polarization control is very challenging. In the 1.5- μm fiber amplifier where some residual mode mixing was observed, polarization instabilities were the strongest. Thus, for difference frequency inside the enhancement cavity, the pump power was limited to 5-6 W resulting in an output power of 2.3 W at 1560 nm.

2.2 Difference frequency generation in a PPLN

2.2.1 Theoretical background

In this subsection, a short review of the basic principles of nonlinear optics and DFG is presented. It is followed by the description of a single-pass DFG experiment, its results in comparison to the theoretical expectations and a discussion of the encountered limitations.

2.2.1.1 Difference frequency generation

DFG is a three-wave nonlinear interaction that occurs when light is coupled into a material lacking inversion symmetry. The medium exhibits a χ^2 nonlinearity. When two light beams of different frequency and sufficiently high intensity are coupled into the crystal, difference frequency generation can occur. By convention (from the OPO community), ω_p , ω_s and ω_i are the pump, signal and idler frequencies, respectively, which are linked by the energy conservation relation (see Figure 2.18):

$$\omega_p - \omega_s = \omega_i.$$

Difference frequency generation has been theoretically studied by Armstrong et al. [45] and formalized by Boyd and Kleinman [46] in the case of two focused gaussian beams.

Nonlinear processes strongly depend on the intensity of the incoming radiations. However, another fundamental parameter is phase matching. Indeed, to participate efficiently to the nonlinear process, the involved waves have to interact together with a defined phase relationship all along their propagation inside the nonlinear crystal. In other words, the phase mismatch between the different waves has to be as close as possible to zero. For a three-wave interaction (pump, signal and idler), the phase mismatch is given by:

$$\Delta k = k_p - k_s - k_i$$

where k_s and k_i represent the wave numbers of the signal and idler, respectively and k_p the wave number of the pump.

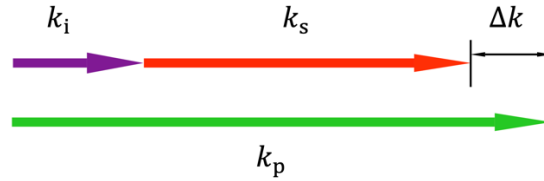


Figure 2.16: Scheme of principle of the phase-matching condition.

Inside the nonlinear crystal, the different waves experience normal dispersion (the refractive index increases with frequency), which makes the phase matching impossible to achieve without any additional process.

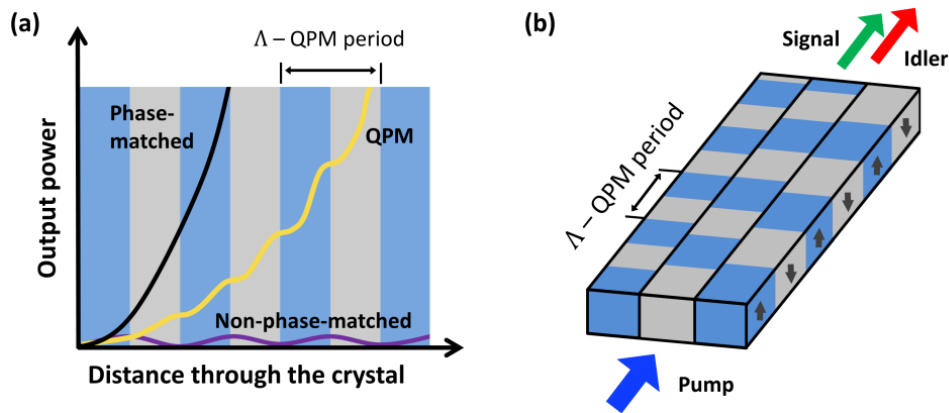


Figure 2.17: (a) Comparison between the output power of a fully phase-matched process, quasi-phase-matched (QPM) process and a non-phase-matched process as function of the position inside the crystal. Λ represents the QPM period. (b) Scheme of a periodically-poled crystal with different channels corresponding to different poling periods.

In the frame of this thesis, quasi-phase-matching is used to efficiently generate DFG. The crystal used for quasi-phase matching is no longer homogeneous but periodically “poled”, meaning that one of the crystal axes is periodically inverted with a spatial poling period Λ . The inversion of the crystal axis changes the sign of the effective nonlinear coefficient, which then compensates for the nonzero phase mismatch coefficient. If the poling period is correctly chosen, the induced electrical field at this point contributes positively to the total amplitude of the induced electric field created before this point instead of decreasing it (see Figure 2.17).

In comparison to the fully phase-matched case, the quasi-phase matching displays a lower idler electric field amplitude. In first order approximation, the effective nonlinear coefficient is reduced by a factor of $2/\pi$. However, the birefringent phase-matching and the quasi phase-matching are based on different terms of the nonlinear tensor of the crystal,

and in the case of lithium niobate, the quasi-phase matching term is several times larger than the birefringent phase matching, leading to higher conversion efficiency. In this work, the crystal used for nonlinear conversion is a periodic-poled lithium niobate (PPLN).

The optical power produced in the DFG process is defined as:

$$P_{\text{idler}} = \eta P_{\text{signal}} P_{\text{pump}} L_{\text{PPLN}}$$

with P_{idler} , P_{signal} and P_{pump} are the optical powers of the idler, signal and pump, respectively and L_{PPLN} the length of the PPLN. The key parameter is η , the efficiency of the DFG process. In [47], it is defined as follows:

$$\eta = \frac{(2\omega_i d_{\text{eff}})^2}{n_p n_s n_i c^3 \pi \epsilon_0} \times \frac{h(\mu, \xi)}{\frac{1}{k_p} + \frac{1}{k_s}}$$

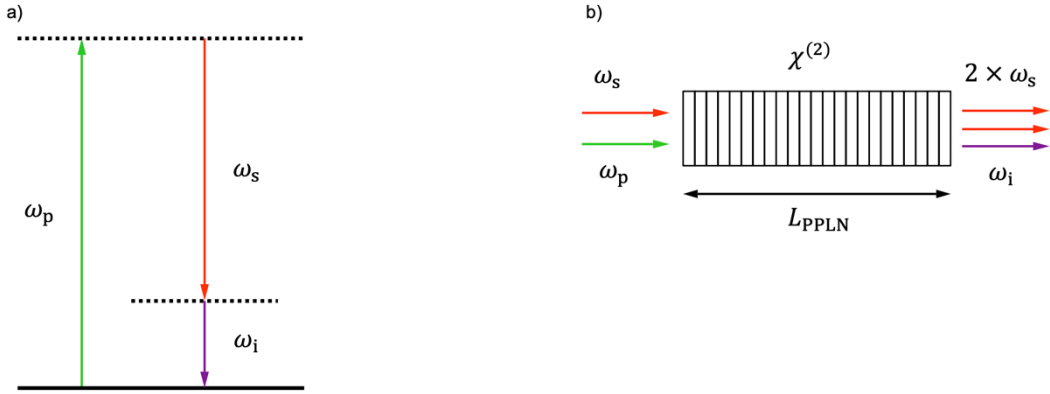


Figure 2.18: a) Energy diagram of the difference frequency generation process. b) Basic scheme of the DFG process with L_{PPLN} being the PPLN length.

with $n_{p,s,i}$ the refractive index of the pump, signal and idler, respectively, c the speed of light, ϵ_0 the permittivity of vacuum and $k_{p,s}$ the wavenumber of the pump and signal.

An important part results from the imaging function $h(\mu, \xi)$ that is precisely described in [48], and [47] sets as follows:

$$h(\mu, \xi) = \frac{1}{2\xi} \times \iint_{0-\xi}^{\xi\xi} \frac{1 + \tau'\tau''}{(1 + \tau'\tau'')^2 + \frac{1}{4} \left(\frac{1+\mu}{1-\mu} + \frac{1-\mu}{1+\mu} \right)^2 (\tau' - \tau'')^2} d\tau' d\tau''$$

with $\mu = \frac{k_s}{k_p}$ the degeneracy parameter, $\tau = \frac{2z}{b}$ where z is the optical distance from the focal point, b the confocal range of a Gaussian beam: $b = 2z_R$ with z_R the Rayleigh range and $\xi = \frac{L_{PPLN}}{b}$ is the focusing parameter.

The imaging function accounts for the spatial distribution of the light intensity at the focus inside the crystal assuming Gaussian pump and signal beam profiles. Note that here a perfect overlap between pump and signal beams is assumed.

As previously seen in the expression of the DFG efficiency, the refractive indices have an important influence. The wavelength and temperature dependency of the extraordinary refractive index in Mg-PPLN are described by the Sellmeier equation [49]:

$$n_e^2 = a_1 + b_1 f + \frac{a_2 + b_2 f}{\lambda^2 - (a_3 + b_3 f)^2} + \frac{a_4 + b_4 f}{\lambda^2 - a_5^2} - a_6 \lambda^2$$

with the temperature-dependent parameter $f = (T - 24.5)(T + 570.82)$ and T the temperature of the material in °C. Note that λ is expressed directly in μm in this equation. All coefficients a_j and b_j , where j is an integer, are relative to the material, they are known as the Sellmeier coefficients. For a 5 % Mg-doped lithium niobate crystal, the Sellmeier coefficients are given in Table 2.2.

Coefficient	Value
a_1	5.319725
a_2	0.09147285
a_3	0.3165008
a_4	100.2028
a_5	11.37639
a_6	0.01497046
b_1	4.753469×10^{-7}
b_2	3.310965×10^{-8}
b_3	2.760513×10^{-5}

Table 2.2 : Determined Sellmeier coefficients for 5% MgO-doped congruent LiNbO₃, data from [50].

The idler wavelength is given by the conservation of energy:

$$\omega_p = \omega_s + \omega_i$$

$$\frac{2\pi c}{\lambda_i} = \frac{2\pi c}{\lambda_p} - \frac{2\pi c}{\lambda_s}$$

$$\lambda_i = \frac{\lambda_s \lambda_p}{\lambda_s - \lambda_p}$$

In this thesis, with a pump wavelength of 1030 nm and a signal at 1560 nm, the idler wavelength corresponds to $\lambda_i = 3070.2$ nm (wavelength in vacuum). The phase mismatch wavevector is defined as:

$$\Delta k = k_p - k_s - k_i - \frac{2\pi}{\Lambda}.$$

The optimum phase-matching corresponds to $\Delta k = 0$, which gives the following condition when introducing the wavelength $\lambda_{p,s,i} = \frac{2\pi n_{p,s,i}(T)}{k_{p,s,i}}$.

$$k_p - k_s - k_i - \frac{2\pi}{\Lambda} = 0$$

$$\frac{1}{\Lambda} = \frac{n_p(T)}{\lambda_p} - \frac{n_s(T)}{\lambda_s} - \frac{n_i(T)}{\lambda_i}$$

For a given temperature T , the phase matching condition defines a unique value of the poling period Λ . In the experiment of this thesis, the selected PPLN crystal has the following set of polling periods: 28.5, 29, 29.5, 30, 30.5, 31, and 31.7 μm . For pump and signal wavelengths of 1030 nm and 1560 nm, the phase matching condition can be fulfilled for a groove with a poling period of 30 μm at a crystal temperature of 124 $^\circ\text{C}$ (see Figure 2.19).

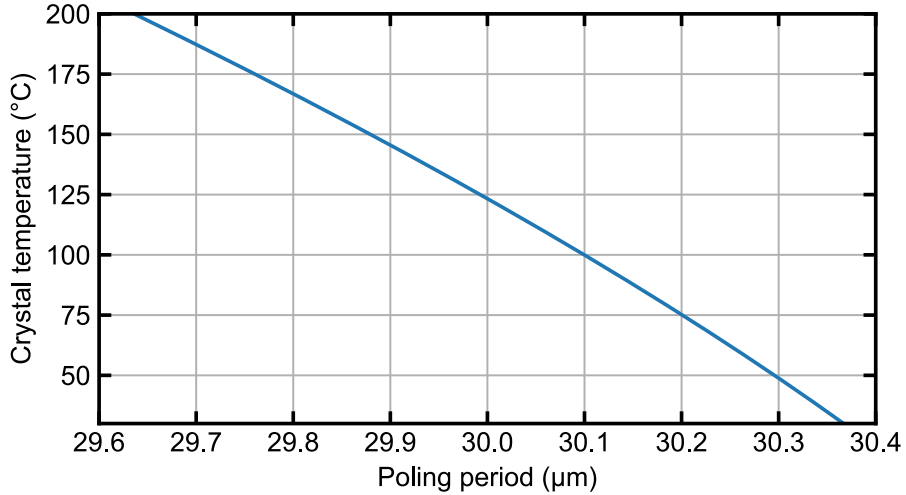


Figure 2.19: Phase matching conditions fulfilled for a given poling period and temperature with $\lambda_p = 1030$ nm, $\lambda_s = 1560$ nm and $\lambda_i = 3070$ nm in vacuum.

2.2.2 Single-pass difference frequency generation experiment

The final experimental goal was to generate a powerful radiation in the mid-IR by DFG by recycling the 1.5- μm beam inside an enhancement cavity. However, a simpler experiment was initially realized in a single-pass configuration to optimize different parameters, such as the beam collimation for an optimum focusing into the crystal as well as the detection of the generated 3- μm radiation.

2.2.2.1 Optimal radius for DFG and collimation line

For a given crystal (5 % MgO-doped PPLN, 5-cm long) and a defined power and wavelength of the pump and signal, only the imaging function can be varied and affects the DFG efficiency. Assuming Gaussian beams, the Rayleigh distance is defined as $z_R = \frac{\pi r_0^2}{\lambda}$ with r_0 the beam radius at the focal point and λ the wavelength of the focused light. The confocal parameter is simply defined as $b = 2z_R$. Figure 2.20 shows the calculated variation of the 3- μm idler power for 6 W of 1030-nm pump and 3.7 W of 1560-nm signal (typical values obtained out of the fiber amplifiers).

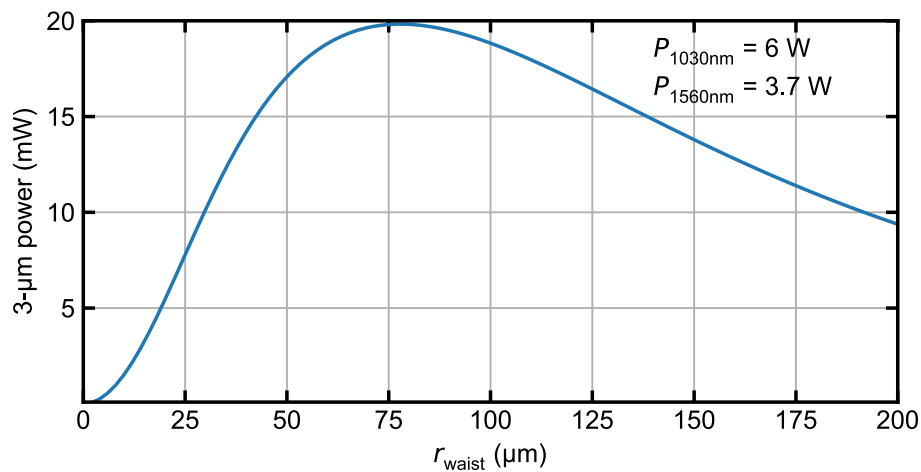


Figure 2.20: Calculated idler power for 6 W of pump and 3.7 W of signal as a function of the radius of the focused beams in a 5-mm long PPLN for a poling period of 30 μm and a crystal temperature of 124°C.

For an optimized overlap of the pump and signal beams, the waist at the focal point must be the same at both wavelengths. The maximum calculated value of the idler power is 19.8 mW, which is reached for a beam radius of $77.2 \mu\text{m}$ at the focal point.

To experimentally reach this value, a collimation line has been set for each wavelength with a selected set of lenses.

Figure 2.21 and Figure 2.22 show the respective collimation setup. A ray propagation script implemented under Python and based on the ABCD-matrix formalism was used to simulate the beam propagation out of the fiber amplifiers.

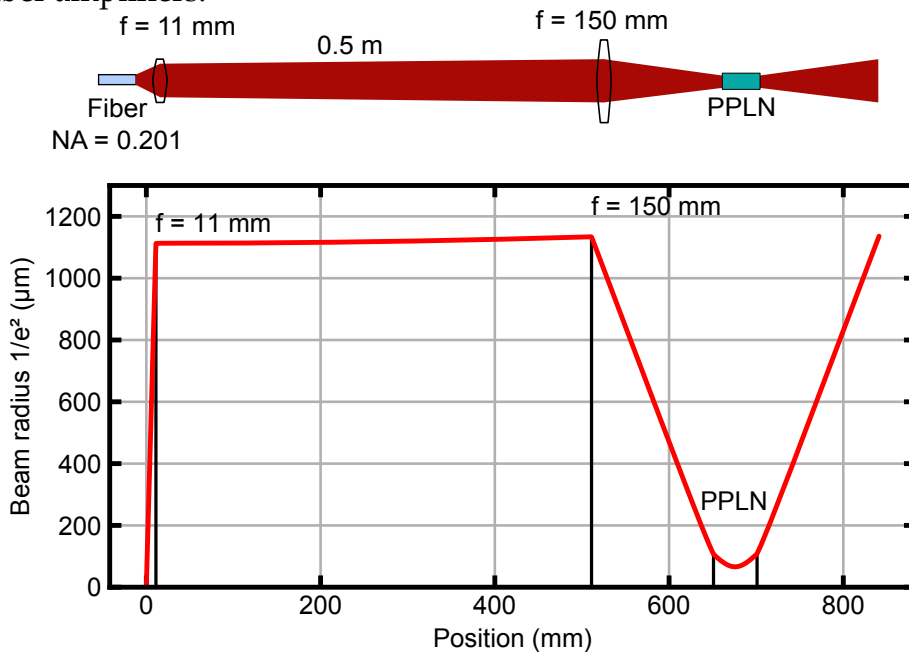


Figure 2.21: 1.5- μm beamline for focus creation inside the PPLN. Top: the beam path scheme with optical components out of the DCF-EY-10/128-PM fiber creating a focus inside the crystal. NA: numerical aperture. Bottom: the beam propagation along the z-axis from simulations.

In order to minimize spherical and coma aberrations, a short focal length ($f = 11 \text{ mm}$) aspheric lens (Thorlabs C220TMD-C) was chosen to collimate the beam at the output of the fiber. The second lens (Thorlabs AC254-150-C-ML) is achromatic and focuses the 1560-nm beam inside the crystal with a calculated radius of $78 \mu\text{m}$ (at $1/e^2$) at focus. In the 1030-nm beam line, the collimation follows a fairly similar path, excepted for the numerical aperture (NA) of the output fiber, resulting in a smaller beam divergence.

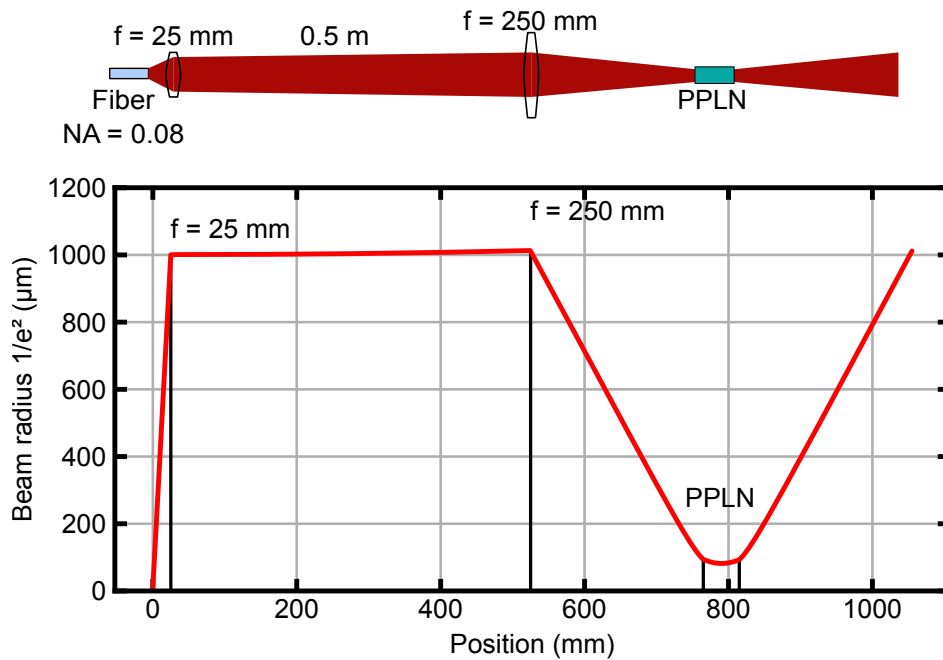


Figure 2.22: 1- μm beamline for focus creation inside the PPLN. Top: the beam path scheme with optical components out of the Yb 1200-10/125DC-PM fiber creating a focus inside the crystal. Bottom: the beam propagation along the z -axis from simulations.

Only a $f = 25$ mm lens (Thorlabs AC1270-25-B-ML) is needed out of the fiber to collimate the beam. The 1- μm beam is then focused by a $f = 250$ mm achromatic lens (Thorlabs AC254-250-C-ML) into the crystal with a 76- μm radius (calculated) at focus.

The simulation method presented here will prove to be very convenient later for collimation and efficient coupling of the beams inside the enhancement cavity (see subsection 2.3.1).

As previously mentioned, the end-tip of both fiber amplifiers are angle-cleaved and followed by the first collimation lens. For both beamlines, the first lens is followed by a half-wave plate and a high-power free-space isolator, which protects the fiber amplifier from any back reflexion from the following components. The high-power isolators also ensure a s -polarization operation that is strictly necessary for the PPLN. About 50 mm after the collimating lenses, the focusing lenses are placed. The two beams are then superimposed using a dichroic mirror. For a good overlap of the two foci, the 1- μm beam path is 10-cm longer than the 1.5- μm path. The two beams are focused in the center of the PPLN crystal. Figure 2.23 gives an overview of the experimental setup.

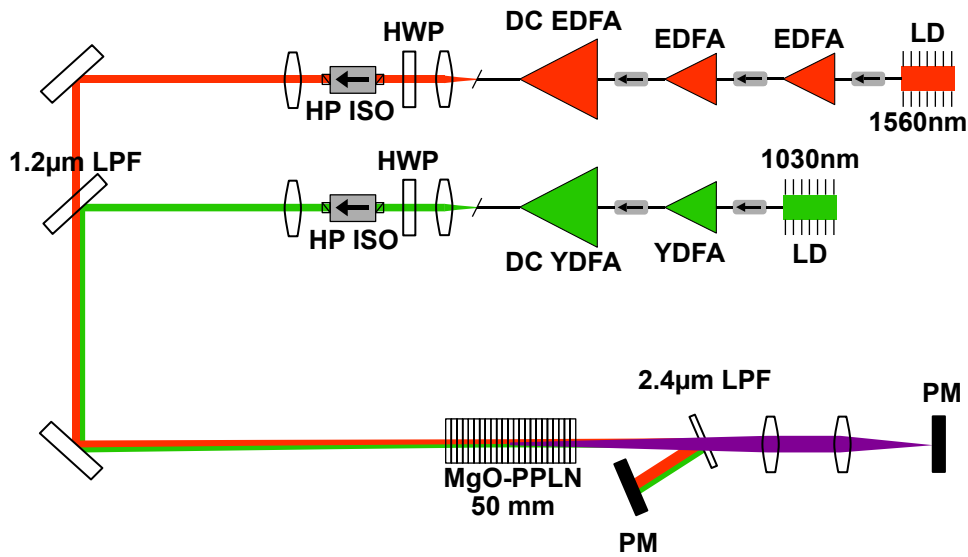


Figure 2.23: Single-pass DFG experimental setup. LD: laser diode, (DC) EDFA: (double-clad) erbium-doped fiber amplifier, (DC) YDFA: (double-clad) ytterbium-doped fiber amplifier, HWP: half-waveplate, HP ISO: high power isolator, LPF: long pass filter and PM: power meter.

In the following paragraph, the method used to ensure a good beam overlap is presented. The details about the PPLN crystal and the 3- μm generation will be treated afterward although already depicted in Figure 2.23.

2.2.2.2 Foci overlap of the two beam-lines

The overlap of the pump and signal beams inside the PPLN crystal directly affects the DFG efficiency. Indeed, the theoretical elements presented before assumed a perfect overlap of the beams.

To experimentally check the proper overlap of the two beams, an imaging camera was placed at the crystal position and moved along the z -axis. Both the radius and the alignment at the focal position were verified for each beam.

This experimental alignment procedure allowed getting a good starting point for the generation of 3- μm light, not to directly optimize the beams overlap. Indeed, once the crystal is placed, the alignment slightly changes as a result of the different refractive index between the two wavelengths. Thus, the fine tuning of the beam overlap was realized with the first 3- μm radiation detection. This alignment procedure was developed for the single-pass experiment but proved to be very useful for the cavity-enhanced DFG, as the beam propagation needs to match the standing-wave inside the cavity.

The 1560-nm beam was focused, at low power operation (less than 1 mW) onto an InGaAs scanning-slit beam profiler (DataRay Inc., Beam'R2-IGA). Figure 2.24 displays the transverse mode of the 1560-nm beam at the focal point.

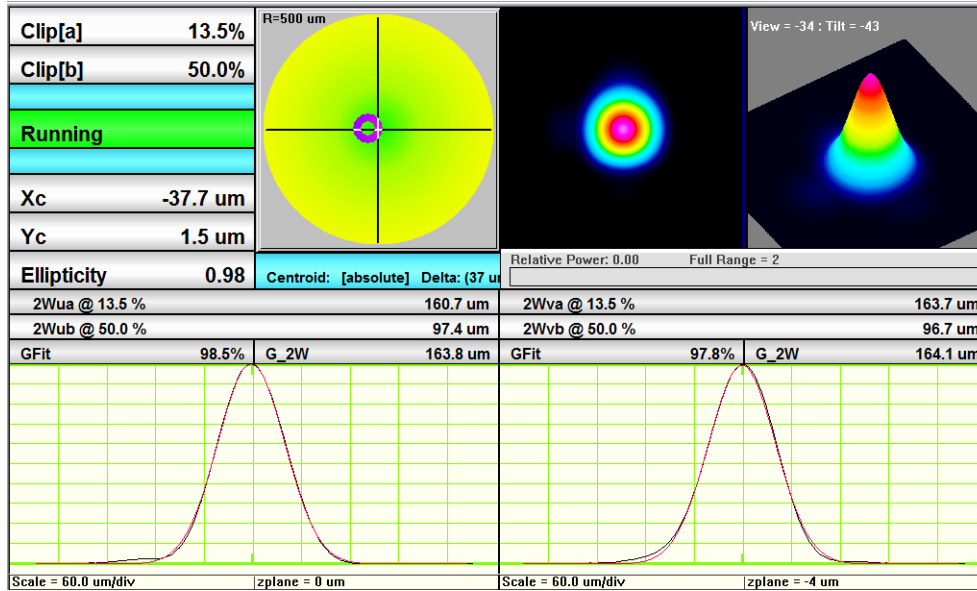


Figure 2.24: Measurement of the beam waist at focus for the 1560-nm beam.

The transverse mode displays a Gaussian shape with a slight difference between the X and Y axis, with a beam waist $w_{1560} = 1/e^2 = 162 \mu\text{m}$ (mean value between the X and Y axis values) in diameter, corresponding to a radius of $r_{1560} = 81 \mu\text{m}$. This value is in rather good agreement with the design simulation ($r_{1560} = 78 \mu\text{m}$).

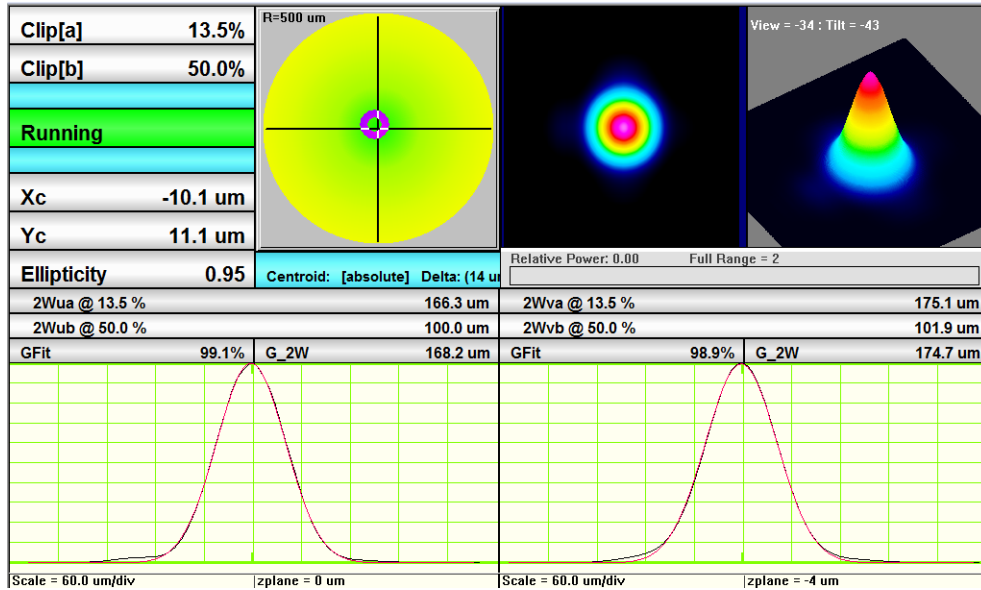


Figure 2.25: Measurement of the beam waist at focus for the 1550-nm and 1030-nm beams overlapped. The beams are superimposed and cannot be distinguished.

The 1030-nm beam was analyzed in the exact same way and showed a beam radius of $r_{1030} = 81.5 \mu\text{m}$ at the same position.

To check the overlap of the two beams, the same method was used with the two radiations shining simultaneously on the slit-cam. Figure 2.25 shows the transverse mode measurement, with a perfect overlap between the two beams.

2.2.2.3 PPLN setup and DFG detection line

The 5% MgO-doped PPLN crystal (Covesion MOPO-5) is 5-cm long and contains 7 channels with a different poling period (28.5, 29, 29.5, 30, 30.5, 31.0 and 31.7 μm). The crystal is mounted in a copper heat sink (see Figure 2.26) and placed into a pierced oven which stabilizes the crystal at a temperature between 20 °C and 200 °C. The oven is mounted onto a 3D-translation stage and the crystal is placed into the beamline. The center of the crystal (along the laser axis) corresponds to the focal point of the two beams.

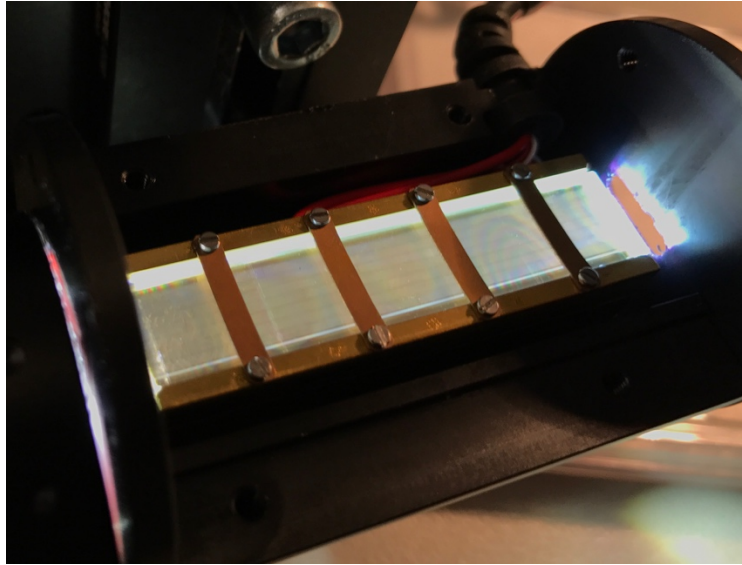


Figure 2.26: PPLN crystal mounted into the oven (opened) and illuminated by white light. The channels with different poling periods are visible.

Both crystal facets, corresponding to input and output of the beams, are AR-coated at 1064 nm, 1550 nm and 3010 nm, strongly reducing the Fresnel reflection for the pump, signal and idler beams. The oven temperature was initially set to 124 °C.

To detect the generated 3- μm light, a 2.4- μm long-pass filter was placed after the crystal, reflecting the 1030-nm and 1560-nm onto a power meter while transmitting the 3- μm light. In a first detection setup, a pair of MgF_2 lenses, with focal lengths $f = 200$ mm and $f = 100$ mm, respectively, was used to collimate and focus the 3- μm light onto a thermal power meter (see Figure 2.23).

2.2.2.4 3- μm generated power

The crystal oven was initially set at 124°C and the pump and signal powers were limited to about 1 W each until some 3- μm radiation was detected on the power meter after playing with different parameters of the system (alignment of the beams and of the crystal, crystal temperature, etc.).

As other nonlinear processes than DFG can occur in the PPLN crystal (e.g. second-harmonic generation SHG or sum-frequency generation SFG), some tests were implemented to verify that the detected power was really related to DFG. As no mid-IR spectrometer was available during this work, the pump or signal beam was blocked to verify that the detected signal resulted from a three-wave process. The use of the 2.4- μm long-pass filter

would also block any SFG or SHG component that might be generated, therefore ensuring that the detected optical power resulted from DFG.

Once some DFG power was detected, the system was finely adjusted to maximize the generated power. The overlap between the pump and signal beams was optimized. Then, the pump and signal powers were raised up to 6 W and 3.7 W, respectively, resulting in 16 mW of idler at 3 μm . Table 2.3 summarizes the achieved 3- μm power levels and DFG efficiency for the corresponding 1.5- μm and 1- μm power levels.

1030-nm Power (W)	1560-nm Power (W)	3- μm Power (mW)	DFG efficiency ($\mu\text{W}\cdot\text{W}^{-2}\cdot\text{cm}^{-1}$)
0.189	0.2	0	0
0.2	0.3	0	0
1.0	0.8	1.0	250
2.0	1.5	2.5	166.7
2.8	2.0	4.2	150
3.8	2.7	8.5	165.7
4.8	3.3	12	151.5
6.0	3.7	16	144.1

Table 2.3: DFG power at 3 μm as a function of pump and signal powers.

Only one current source was available for the high-power multimode 980-nm pump diodes of the high-power fiber amplifiers at 1.5 μm and 1 μm at the time of this experiment. Therefore, the four pump diodes were connected in series and driven by the same current, resulting in a simultaneous increase of the pump power for both fiber amplifiers. As the efficiency of the two amplifiers is different (see subsection 2.1.2), the total output power at 1.5 μm and 1 μm increased both linearly, but at a different rate. Therefore, the generated idler power scales as the product of the pump and signal powers. Figure 2.27 displays the power slope corresponding to the data set of Table 2.3 together with the expected values. A good general agreement is observed between the predicted and measured optical powers, but the discrepancy increases at high pump and signal powers.

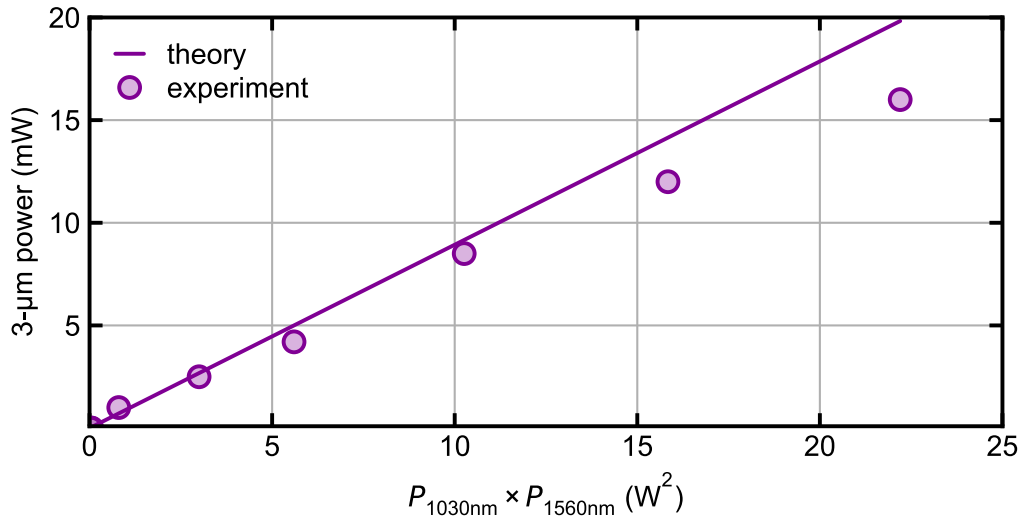


Figure 2.27: DFG power slopes. In dots, data set from the experiment. In plain line, data calculated from the simulations. The x-axis represents the product of the pump and signal powers.

In this experiment, the fiber amplifiers were not optimized and a little portion of the power was contained in higher order transverse modes, as mentioned in subsection 2.1.2.1, which led to losses in efficiency. Also mentioned at the end of the same section, the thermal management of the fiber was not optimized and due to excessive heating (at high power), the fiber tip was slightly bending leading to beam pointing instabilities. As the overlap of the two beams is a critical parameter, beam pointing instabilities has potentially a strong negative effect on the DFG efficiency.

In conclusion of this subsection, single-pass DFG was successfully achieved with a good agreement with the simulated performance. The encountered limitations gave good indications about the modification of the setup needed in order to optimize the DFG inside an enhancement cavity.

2.3 Difference frequency generation inside an enhancement cavity

DFG in a cw single-pass configuration is an experiment with a low level of complexity, however it usually displays a weak power conversion for bulk crystals. In order to improve the efficiency, a resonant cavity can be set around the nonlinear crystal to recycle the non-converted power from the pump or the signal wavelength. This principle has already been explored in cw operation for frequency doubling [51], as well as for DFG [52,53]. Nevertheless, the output power of such systems has been limited so far to the tens of milliwatts level. Today high-power amplifier systems in combination with PPLN crystals are expected to enable narrow linewidth 3- μm generation with 1 - 10 W power.

2.3.1 Enhancement of the 1.5- μm signal in a resonant cavity

2.3.1.1 Cavity design

The implementation of a cavity around the crystal changed the optimal value of the beam radius at the focal point inside the crystal. In order to create a resonant cavity sustaining a 92- μm tight focus inside a 5-cm long PPLN crystal, the simulation software RP Resonator was used. The software calculates the propagation of gaussian rays using the ABCD matrix formalism. The cavity design was realized to meet certain number of requirements fulfilling some constraints. The intracavity losses had to be as small as possible, implying to limit the number of cavity mirrors for instance. The choice of the mirrors (coatings, radii of curvature, angle of incidence), the space between them as well as their mount has been made accordingly.

Many designs have been experimentally tried in the frame of this thesis, but only the last implemented configuration that led to the results reported here after is presented. The idea of using only four mirrors has been abandoned to the profit of a 6-mirror configuration driven by the necessity to have input and output couplers, two curved mirrors and one mirror mounted on a piezoelectric actuator. Figure 2.28 shows the geometry used for the last cavity design.

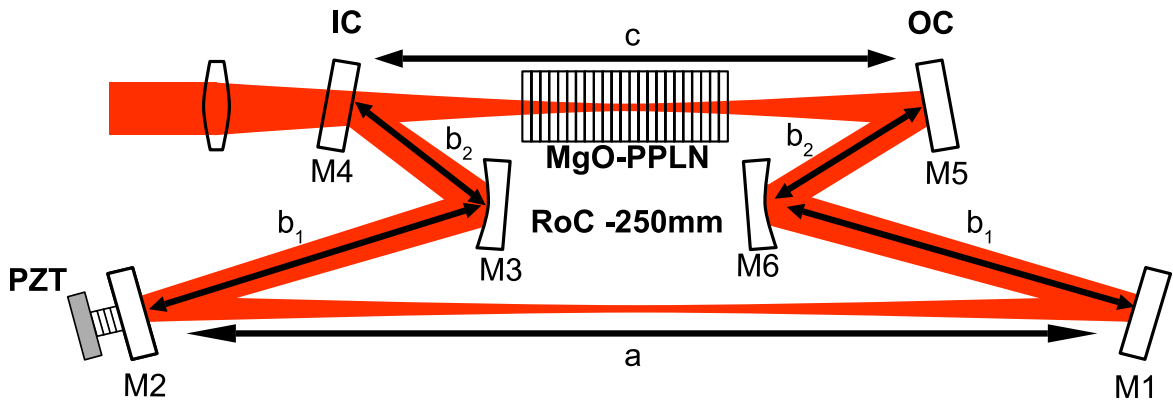


Figure 2.28: Cavity scheme: the two curved mirrors (radius of curvature (ROC) = -250 mm) create a 105- μm inside the 5-cm long PPLN crystal. Mirrors are labeled from M1 to M6 and separated by distances a , b_1 , b_2 and c . They are $a = 430$ mm, $b_1 = 165$ mm, $b_2 = 70$ mm and $c = 240$ mm. IC: input coupler, OC: output coupler, PZT: piezoelectric actuator.

In this configuration, the input and output couplers are plane mirrors. It allows for easy in-coupling of the signal and pump beams as well as the out-coupling of the 3- μm light. A CaF_2 substrate was used as output coupler, which exhibits low absorption of the mid-IR beam.

The two curved mirrors (radius of curvature $\text{ROC} = -250$ mm) produce a focus of diameter $r_0 = 105$ μm (from simulation) in the center of the crystal. The distance between mirrors is optimized to create a stable focus inside the crystal with a radius as close as possible from the optimal calculated value of 92 μm . The beam size along its propagation in the resonant cavity is depicted in Figure 2.29. The cavity length is equal to 1.14 m.

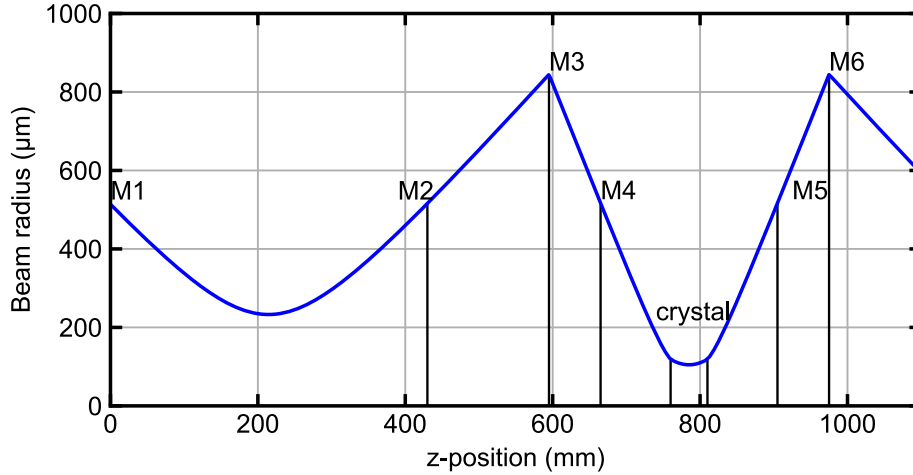


Figure 2.29: Beam radius (at $1/e^2$) along the z-axis inside the resonant cavity of total length of 1.14 m.

In first experimental configurations to test the resonant cavity, the crystal was removed. Thanks to the focus position being at the center of the crystal, the cavity remained stable without changing any parameter.

2.3.1.2 Beam focus

For the single-pass configuration, the beam focusing setup was limited to two lenses at each wavelength, the second one producing the desired beam waist at focus. In the case of coupling into a resonant cavity, not only the beam size at focus has to be carefully handled, but the convergence of the beam as well, such that the incoming beam matches the cavity mode.

Compared to the single-pass configuration, an additional pair of lenses was added and the 1.2- μm long-pass filter was placed between this telescope and the last focusing lens. The same Python script was used as in the previous subsection to simulate the beam propagation in order to determine the needed lenses as well as the distances between the different optical elements. As displayed in Figure 2.30, the beam from the PM1550 fiber end tip is collimated by an aspheric lens with $f = 8$ mm. Then it propagates over a distance of 50 cm (through a half-wave plate and an HP-isolator) and goes through the telescope which is composed of $f = 30$ mm and $f = 50$ mm singlet lens. The beam expands over 1 m until the last focal lens, an achromatic $f = 500$ mm lens and is focalized into the PPLN crystal through the first cavity mirror.

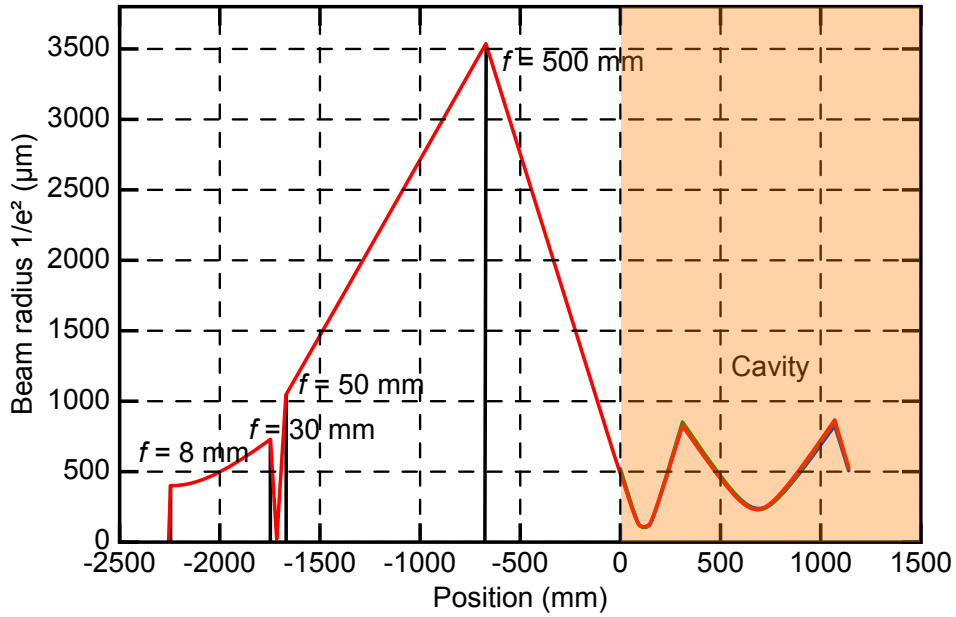


Figure 2.30: Simulated propagation of the 1560-nm beam out of the PM1550 fiber. The cavity starts at position 0 of the x-axis. Lenses are depicted with plain black lines and their focal length is noted above.

One can notice the large beam radius after the telescope. Because of geometrical considerations, the distance between the last focusing lens and the first cavity mirror had to be long (65 cm) in order to place two in-coupling plane mirrors.

Figure 2.31 shows that the incoming 1560-nm beam overlaps properly with the intra-cavity resonant beam with small amount of astigmatism.

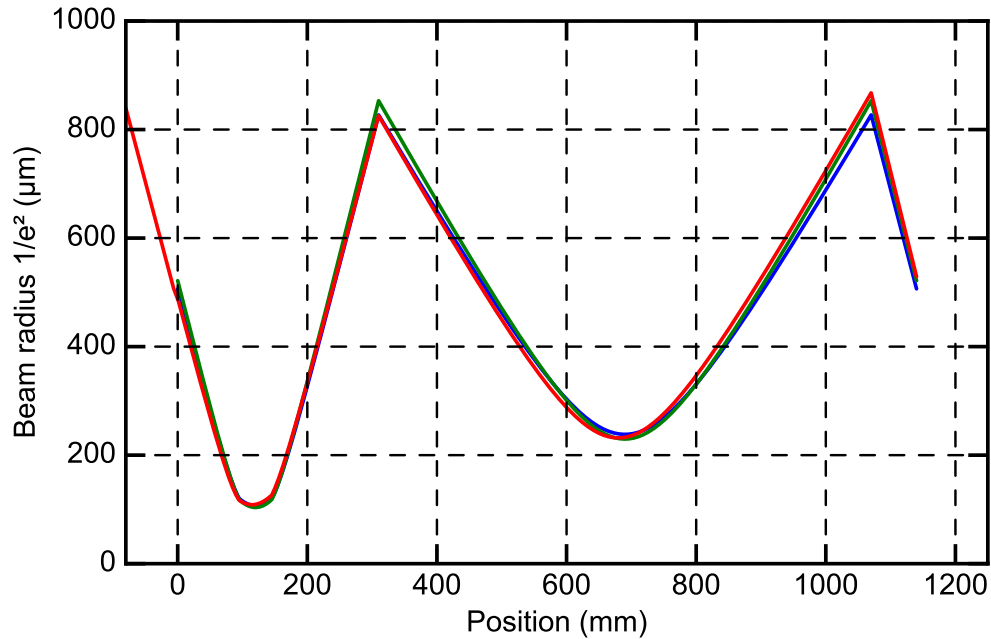


Figure 2.31: Zoom on the cavity part of the simulations. In blue and green the vertical and horizontal resonant beam size in the cavity. In red the incoming beam.

The propagation of the 1030-nm beam follows a similar path. The beam is collimated out of the PM980 fiber by an $f = 11$ mm aspheric lens and propagates until the telescope composed of an $f = 25$ -mm lens and an $f = 50$ mm lens. As for the 1560-nm beam line, the beam is expanded and recombined with the 1560-nm beam before the $f = 500$ mm achromatic lens that focuses the two beams into the PPLN crystal. In the next paragraph, the overlap of the two beams and their radius at focus is presented.

2.3.1.3 Foci overlap of the two beam lines

Using the same setup as for the single-pass DFG, the beams were analyzed with imaging cameras along their propagation axis. The purpose was two-fold, on one hand to align the 1030-nm beam and its overlap with the 1560-nm beam, and on the other hand to check the agreement between the measured and simulated beam propagations. For a correct mode-matching of the incident beam into the cavity, this step is crucial.

For beam alignment, only an InGaAs scanning slit beam profiler (DataRay Inc., Beam'R2-IGA) was used as it operates at both wavelengths.

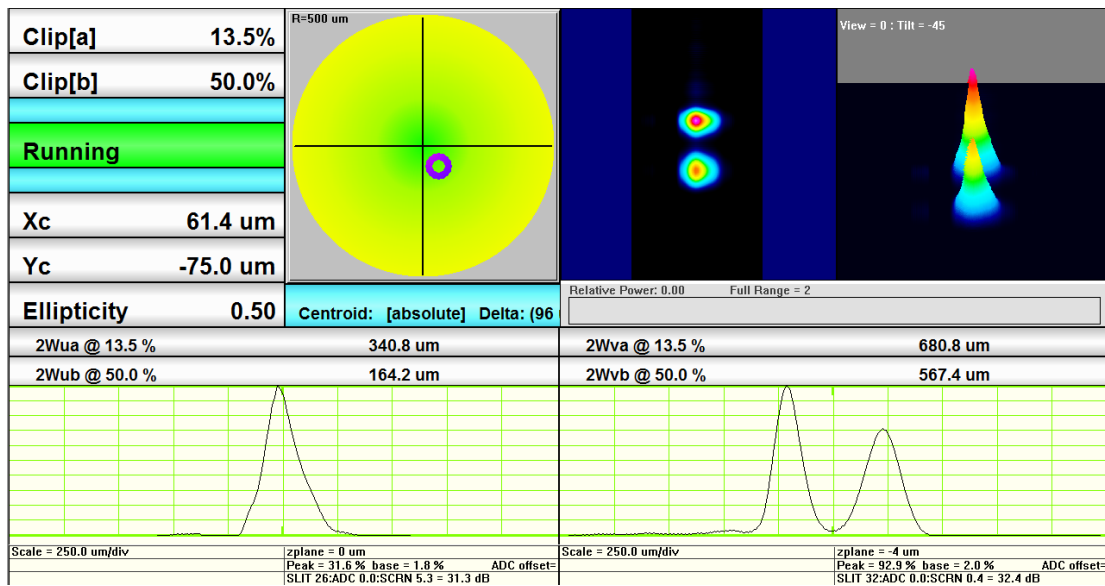


Figure 2.32: 1560-nm and 1030-nm separated beams around the focus position (vertically separated for check).

Figure 2.32 shows an image of the Beam'R2-IGA during the alignment process. As the beams are set at a height of 75 mm upon the optical table, the two beams are almost always aligned vertically. To achieve a good overlap of the beams in the horizontal direction, the 1030-nm beam was first slightly tilted vertically such that the two beams were close but separated. Once the two beams were aligned on the x-axis, the 1030-nm beam was set back to its initial height, achieving a complete overlap of the two beams in the two directions.

To verify the beam size along the propagating axis, different cameras were used. The Beam'R2-IGA was kept for the 1560-nm beam but a DataRay-BladeCam HR was used for the 1030-nm beam (for large beam diameters at 1030 nm, our slit-camera Beam'R2-IGA shows some aberrations). The 1030-nm beam propagation is far less critical than the 1560 nm beam. Figure 2.33 summarizes the measurements of the 1560-nm beam size along the propagation axis. During the measurements with the slit-beam profiler, the crystal was not inserted into the cavity as the device is too large. A very good agreement is observed between simulations and measured values, which was also the case for the 1030-nm.

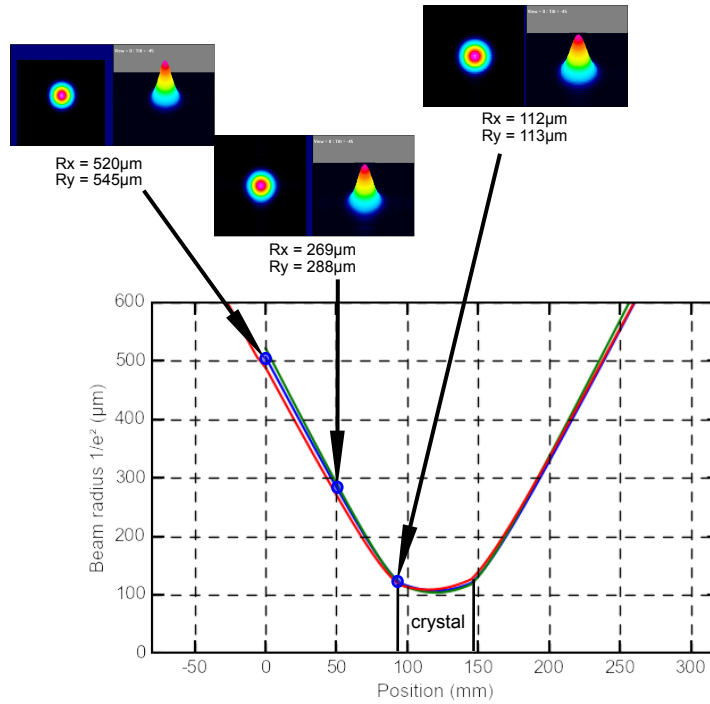


Figure 2.33: The experimental mode-matching. Upper part: experimental values of the 1560 nm beam size. Down part: simulations of the propagating beam (with the crystal). In blue and green the vertical and horizontal resonant beam size in the cavity. In red the incoming beam. The measurement points are $z = 0$ mm, $z = 50$ mm and $z = 95$ mm.

2.3.2 3- μm DFG inside a resonant cavity

2.3.2.1 Cavity resonance

As mentioned in the previous section, the cavity mirrors have been placed according to resonator simulations. The choice of the mirrors is important as the cavity resonance mainly depends on the intracavity losses and thus on the mirror reflectivity.

For a three-wave interaction such as DFG, the mirror coating is of high importance. Hence, the input coupler was coated on a fused silica substrate with our ion beam sputtering (IBS) machine with a reflectivity of 99% at 1560 nm and an anti-reflection (AR) coating at 1030 nm. The output coupler is a CaF_2 substrate with a highly-reflective (HR) coating at both 1560 nm and 1030 nm and an AR coating at 3 μm with a large acceptance bandwidth (from 2800 nm to 3600 nm). All other cavity mirrors are HR-coated at 1560 nm and the plane mirrors are also HR-coated at 1030 nm. The coating of the curved mirrors is only specified at 1550 nm as they have been acquired from LaserOptik and not coated by our IBS machine.

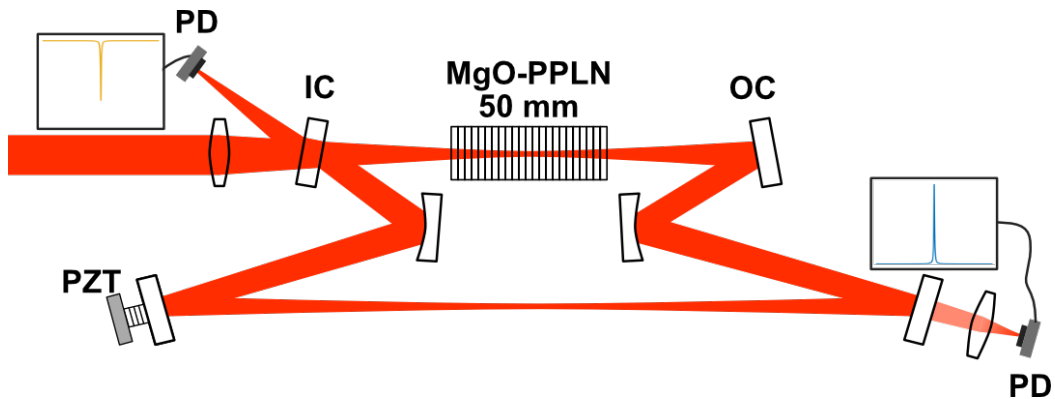


Figure 2.34: 1.5- μm cavity setup with the PPLN crystal. A photodiode is placed in reflection and another one in transmission. PD: photodiode, IC: input coupler, OC: output coupler, PZT: piezoelectric actuator. PD-displayed resonance in transmission (in blue) and in reflection (in yellow).

The signal reflected from the input coupler was sent to a photodiode and the leakage from one of the plane mirrors was detected by another photodiode. The cavity transmission signal can be observed by scanning either the cavity length with the piezoelectric actuator (see Figure 2.34) or the frequency of the 1560-nm signal with the current of the seed laser diode. In a first scheme, the seed laser diode current was modulated (with a triangular waveform) to scan the cavity resonance.

To excite a cavity resonance, the laser beam has to follow the beam path defined by the cavity design until it comes back to its exact position onto the input coupler. This path corresponds to the first cavity round trip. By aligning the cavity mirrors such as all cavity round trips overlap with the first one, resonance is achieved. On the transmission photodiode, peaks of intensity are appearing while on the reflection photodiode peaks of depletion resulting from destructive interferences can be seen. The cavity is then aligned such as only one peak is visible per free spectral range (FSR), which corresponds to the fundamental mode.

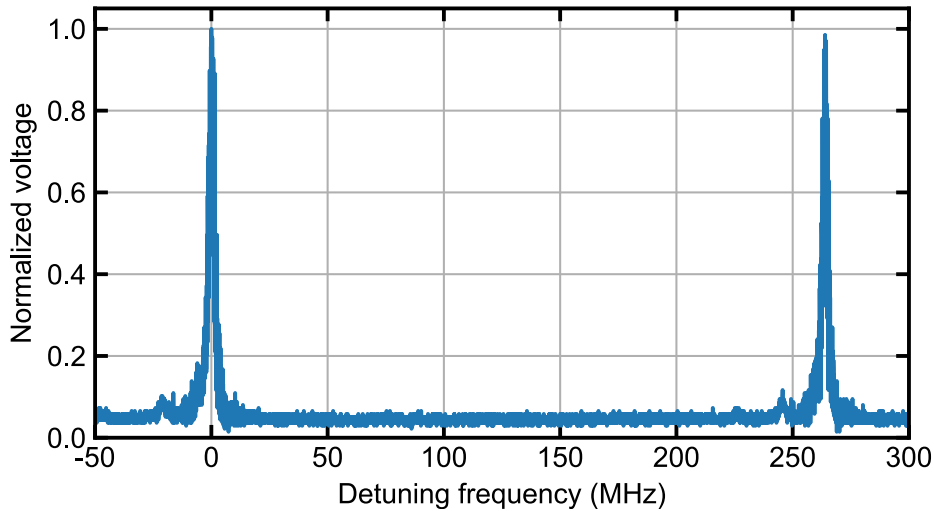


Figure 2.35: Two cavity resonances measured in transmission on a photodiode when scanning the seed laser frequency via its injection current.

In a first attempt of aligning the cavity, the crystal was not placed in the cavity. Figure 2.35 shows the transmission photodiode signal of the optimized cavity while the current of the seed laser diode was modulated by a triangular signal.

Once a clear resonance was obtained, the crystal was inserted into the cavity, and the alignment had to be readjusted. The achieved transmission and reflection signals on the photodiodes are depicted in Figure 2.36. The contrast of the resonance on the reflected signal is around 50%.

Indeed, now a proper resonance is found, the signal frequency has to follow the cavity movements such as the resonance condition is always fulfilled. In order to achieved this locking a Pound-Drever-Hall (PDH) locking scheme is setup [54]. Before entering the fiber amplifiers the fiber-coupled 1560-nm signal goes through an electro-optical modulator (EOM) which modulates the optical signal at the radio-frequency of 36.8 MHz creating sidebands around the laser frequency. The reflected signal is sent to a PDH module that demodulates it at the EOM frequency to generate the characteristic PDH error signal (see Figure 2.36). This error signal is sent to a PID servo controller which locks either the laser frequency onto the cavity resonance by retroacting on the diode current or the cavity length onto the laser by retroaction on the piezo actuator inside the cavity. Note that for 3- μm frequency-noise measurements, the retro-action loop acts onto the piezo actuator and thus the cavity length (in the next section) leaving the 1560-nm

frequency untouched. The cavity is thus locked in resonance with the seed laser and the intra-cavity power at 1560 nm is enhanced.

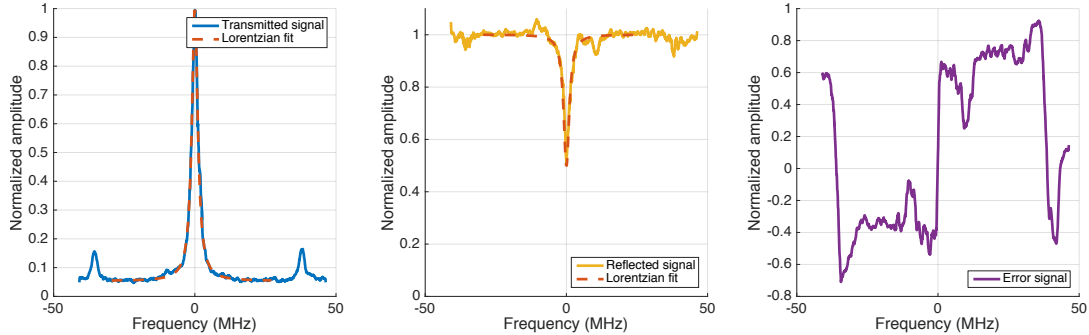


Figure 2.36: From left to right: transmission signal, reflected signal and error signal of the cavity as a function of the laser detuning frequency obtained when scanning the seed laser current.

Using the transmitted signal side bands to scale the laser current scan into a frequency axis, the cavity FSR and the resonance linewidth were calculated. The finesse of the cavity was then estimated, as well as the cavity enhancement factor. Measuring an FSR of 258.6 MHz and a resonance FWHM of 2.5 MHz, the cavity finesse was estimated to be around 102.5 and the cavity enhancement factor $G_{th} = 32.6$. The cavity coupling ratio was obtained from the contrast of the reflected signal $C = 0.5$. The theoretical effective power enhancement factor of the cavity (considering the fraction of the incident power effectively resonating inside the cavity) was obtained accordingly:

$$G_{eff_th} = C \times G_{th} = 0.5 \times 32.6 = 16.3$$

For a direct evaluation of the intracavity power, the power of the 1560-nm beam has been measured out of resonance before and after the output coupler, giving its transmission ($T_{oc} = 1\%$). Thus for an incoming power of 1.7 W, the intracavity power was estimated to 24 W, resulting in a power enhancement factor of 14.1. This measurement is in relatively good agreement with the effective power enhancement factor calculated previously.

2.3.2.2 3- μm light detection and power slope

Once the 1.5- μm enhancement cavity was locked at resonance onto the laser frequency, adding the 1- μm beam allowed powerful DFG inside the PPLN crystal. To detect and quantify the 3- μm radiation, the previous experimental setup has been slightly modified (see Figure 2.37). The 1- μm beam was reflected by the output coupler and was extracted through the

first curved cavity mirror. A MgF_2 $f = 200$ mm lens was added after the cavity output coupler and a $2.4\text{-}\mu\text{m}$ long-pass filter was used to extract the remaining leakages at $1.5\ \mu\text{m}$ and $1\ \mu\text{m}$ from the $3\text{-}\mu\text{m}$ beam. The $1.5\text{-}\mu\text{m}$ beam was focused onto a photodiode using a lens with a short focal length ($f = 10$ mm), and the signal from the photodiode was used as the cavity transmission signal. A thermal power-meter was placed in the $3\text{-}\mu\text{m}$ beam.

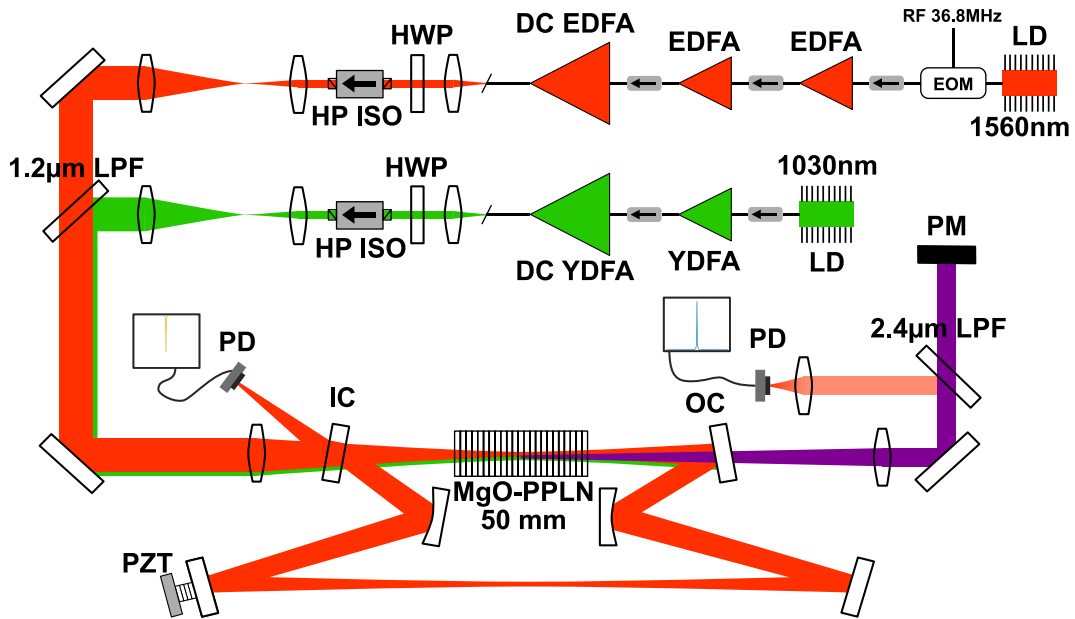


Figure 2.37: General experimental setup including high-power fiber amplifiers, beams collimation, $1.5\text{-}\mu\text{m}$ enhancement cavity and $3\text{-}\mu\text{m}$ detection. The $1\text{-}\mu\text{m}$ beam is represented in green, the $1.5\text{-}\mu\text{m}$ beam in red and the generated $3\text{-}\mu\text{m}$ light in violet.

By setting the 1560-nm power to 2.3 W and locking the laser frequency to the cavity resonance, thus enhancing the intracavity power to 32 W (estimated value with $1.5\text{-}\mu\text{m}$ power measured behind a cavity mirror), the $3\text{-}\mu\text{m}$ power slope was recorded while the 1030-nm power was raised (see Figure 2.38).

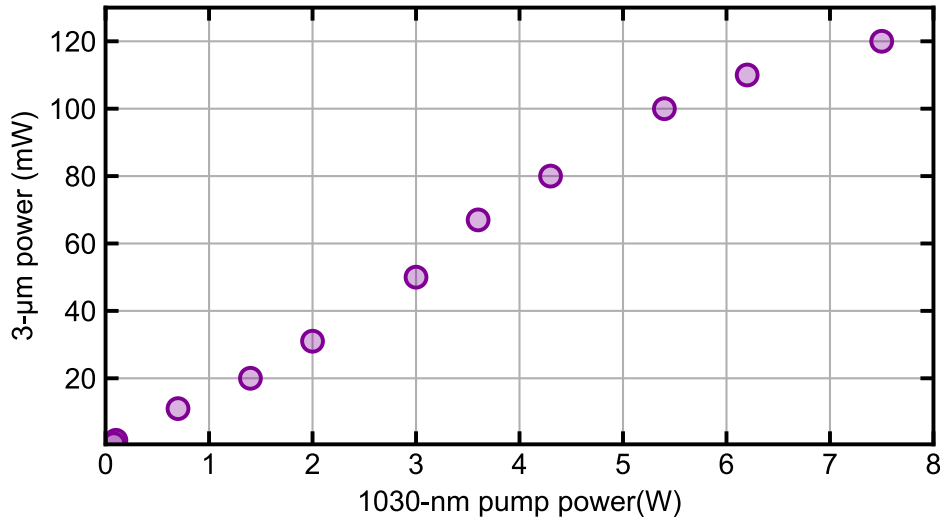


Figure 2.38: Mid-IR (3- μm) power slope for 2.3 W of 1.5- μm seed light and a varying 1 μm pump power (x-axis).

Up to 120 mW of 3- μm power was measured on a thermal power meter, corresponding to a conversion efficiency of $\eta = 1.39 \text{ mW}\cdot\text{W}^{-2}\cdot\text{cm}^{-1}$ for the overall system and $\eta = 98.5 \text{ }\mu\text{W}\cdot\text{W}^{-2}\cdot\text{cm}^{-1}$ for the intracavity conversion efficiency (equivalent to single-pass). Only up to 7.5 W of 1030-nm pump power was used because strong instabilities prevented us to further increase the pump power. In an optimized configuration (alignment, less input power from the 1560-nm amplifier and thus less instabilities), up to 113 mW was achieved with only 4.3 W of 1030 nm and 1.4W of 1560 nm, resulting in a conversion efficiency of $\eta = 3.75 \text{ mW}\cdot\text{W}^{-2}\cdot\text{cm}^{-1}$ for the overall system and $\eta = 265.9 \text{ }\mu\text{W}\cdot\text{W}^{-2}\cdot\text{cm}^{-1}$ for the intracavity conversion efficiency. In comparison, with their enhanced cavity, Witinski et al. [53] showed a conversion efficiency of $\eta = 2.86 \text{ mW}\cdot\text{W}^{-2}\cdot\text{cm}^{-1}$ ($\eta = 285.7 \text{ }\mu\text{W}\cdot\text{W}^{-2}\cdot\text{cm}^{-1}$ inside the cavity) in single pass Guha et al. [34] achieved $\eta = 528.9 \text{ }\mu\text{W}\cdot\text{W}^{-2}\cdot\text{cm}^{-1}$.

The main limitation of our system comes from thermal effects and results in a non-stable power level of the 3- μm radiation on a long-time scale (over few minutes). Indeed, after a 5-10 minutes of high-power operation (2 W of 1560 nm for example), the alignment of the 1.5- μm beam line has drastically changed and needs to be corrected. And even afterwards the position of the focal point inside the crystal is not very stable. The same effect is visible on the 1- μm beam line however with less amplitude, resulting in a very unstable overlapping of the two beams inside the crystal and thus a very unstable 3- μm power level. The problem is caused by the

thermal behavior of the fiber holders at the end of the two high power fiber amplifiers. Even if the pump power (980 nm for both 1- μm and 1.5- μm fiber amplifiers) is extracted before the end of the amplifier, the glue at the end tip of the amplifier is heating up, bending the fiber enough to misalign the beam line afterward. An improved setup should be designed in the future to prevent any fiber end tip movement (with a metallic ferrule for example).

Nevertheless, before any further optimization of the system, its performance is already sufficient for a proof-of-principle evaluation of its noise properties, which is done in the following section.

2.4 Noise characterization of the intracavity DFG source

For most applications of mid-IR sources like in spectroscopy, the linewidth of the source directly impacts the precision of the measurements. Narrow-linewidth sources are thus highly attractive. However, the determination of a laser linewidth at kHz or even sub-kHz level is not an easy task. The FWHM linewidth of a laser results from its frequency noise, and lasers with low frequency noise levels display a narrow linewidth. The most common ways to determine the frequency noise of a laser source are to compare it to another low-noise source at the same wavelength or to use a narrow molecular or atomic absorption line as a frequency discriminator to convert the laser frequency fluctuations into measurable intensity fluctuations. In any case the measurement is limited by the highest noise level between the source under test and the reference, which requires a reference source with a lower noise.

2.4.1 Choice of linewidth determination method

The linewidth of the 3- μm radiation can be determined by applying the β -separation line method to its measured frequency noise [3]. This requires a beat note with another 3- μm reference source of lowest noise or the use of an optical frequency discriminator such as the side of a narrow molecular transition.

A first idea was to frequency-double the 3- μm beam inside a 20-mm long PPLN, generating a 1505-nm radiation which could be compared with one line of a stabilized frequency comb available at the institute (FC 1500 from Menlo System). However, the calculated optimum SHG efficiency for the 3- μm radiation is only $6.4 \times 10^{-5} \text{ W}^2/\text{W}$ for the available 20-mm long PPLN crystal. With such a weak power, the detection and analysis of a beat note with a line of the frequency comb (power estimated about hundreds of nW) would be too challenging.

Inside the PPLN, besides the DFG, many other non-optimized nonlinear processes occur. They are usually considered as parasitic light. Indeed, during the experiment, green and red radiation were visible when a paper sheet was placed after the PPLN while the two near-IR beams were overlapping inside the crystal. The green light results from the frequency doubling of the 1030-nm beam, while the red light originates from the sum-frequency generation (SFG) between the 1030-nm and 1560-nm radiation. Indeed, if one of the two near-IR beams is blocked, the red light disappears

(this light was actually used for DFG pre-alignment). Assuming that the frequency noise of the SFG is comparable to that of the DFG, a beat-note between the SFG red light and a line from a frequency comb extending in the visible could be detected and analyzed. However, in practice, about 1 μW of SFG red light could be measured and the corresponding power of an individual line of the frequency comb was estimated at the nW level. Once again, the too-low power levels prevented any beat detection.

The previous attempts to evaluate the frequency noise of the 3- μm radiation were based on a scheme which uses an external and independent source as a reference to make a beat note: one line of a frequency comb at 1505 nm in the first case and in the red for the second case. As the lack of power was the limiting factor, another DFG-based source of 3- μm radiation seeded by independent fiber amplifiers was set using a 5-mm long PPLN crystal. The pump and signal sources, at 1 μm and 1.5 μm can be chosen according to the need of the experiment. In an ideal case, two independent sources at 1 μm and two at 1.5 μm should seed the cavity-enhanced DFG and the second DFG source. However, because of the unavailability of narrow linewidth and stable sources, the same pump and signal sources at 1 μm and 1.5 μm , respectively, were used to seed the cavity-enhanced DFG and the single pass DFG (see Figure 2.39). An acousto-optic modulator (AOM) shifts the 1560-nm light going to the cavity-enhanced DFG setup by 34 MHz, allowing a heterodyne beat between the two 3- μm sources to be implemented. In this configuration, as the two 3- μm signals share the same near-IR seed sources, the measurement of the frequency noise of the 3- μm beat note gives only the additive phase noise of the overall system (fiber amplifiers, cavity and DFG conversion). To complete the frequency noise analysis and to evaluate the total linewidth of the 3- μm radiation, a separate measurement of the frequency noise of the two seed and pump near-IR sources is needed. The 1030-nm semiconductor laser from QD Laser, used as 1- μm source in the DFG setup previously reported, was tested by analyzing its beat signal with a frequency-stable source at 1 μm (supercontinuum spectrum of a fully-stabilized frequency comb). However, the resulting beat signal appeared to be very unstable with a strong ripple visible on the RF spectrum analyzer. This made this laser source unsuitable for narrow-linewidth 3- μm light generation by DFG due to its large frequency noise. Therefore, this laser diode was changed for a 1064-nm semiconductor laser module (ORION laser from Redfern Integrated Optics - RIO) with a much better frequency stability and lower frequency noise for the subsequent experiments described below.

The wavelength change of the 1- μm source introduced a number of issues. The 1- μm fiber amplifier, initially designed for 1030 nm, contained several components that were not well suited for 1064 nm (the isolators and

WDM displayed higher transmission losses). All the amplifier components being fiber-spliced together, changing one component in the line is a very delicate operation. Instead of rebuilding the fiber amplifier in an optimized way for the 1064-nm source, the fiber amplifier was used with the previously presented design (see subsection 2.1.2.1) but restricted to low power operation (with 3 W of maximum output) to avoid any component damage. On the crystal part, the wavelength change modified the phase-matching conditions as well as the generated 3- μm wavelength. Using the same crystal channel (with 30- μm poling period) the oven temperature was raised up to 177 °C for an efficient phase-matching. According to energy conservation, the idler wavelength was 3346 nm.

2.4.2 Setup of the second source of 3- μm

The pump and signal laser sources (at 1560 nm and 1064 nm) are divided into two channels: one seeds the cavity-enhanced DFG setup previously described and depicted in Figure 2.37, the other channel seeds the single-pass DFG source. The 1- μm laser diode is directly amplified in a double-clad 4.5-m long ytterbium-doped fiber amplifier, increasing the power from 10 mW to 450 mW. The 1064-nm line is then divided into two channels through a 50/50 fiber coupler. A power of 194 mW goes in the high-power amplifier for the cavity-based 3- μm setup and 187 mW go in the 2nd 3- μm source setup. On the 1560-nm line side, the Eblana-Photonics laser diode is simply divided into two equal channels, with a power of 4 mW each. Before entering the high-power amplifier, the frequency of the signal is shifted by a value ranging from 32 MHz to 42 MHz using a fiber-coupled AOM (IntraAction FCM-401E6AP). Because of its poor transmission, only 2 mW are coupled into the high-power 1.5- μm fiber amplifier after the AOM. The second 3- μm source setup consists of an amplification stage for each wavelength, a WDM to combine them, then a free-space part where the beams are collimated and focused into a 5-mm-long MgO-doped PPLN and finally separated from the 3- μm using a 2.4- μm long-pass filter.

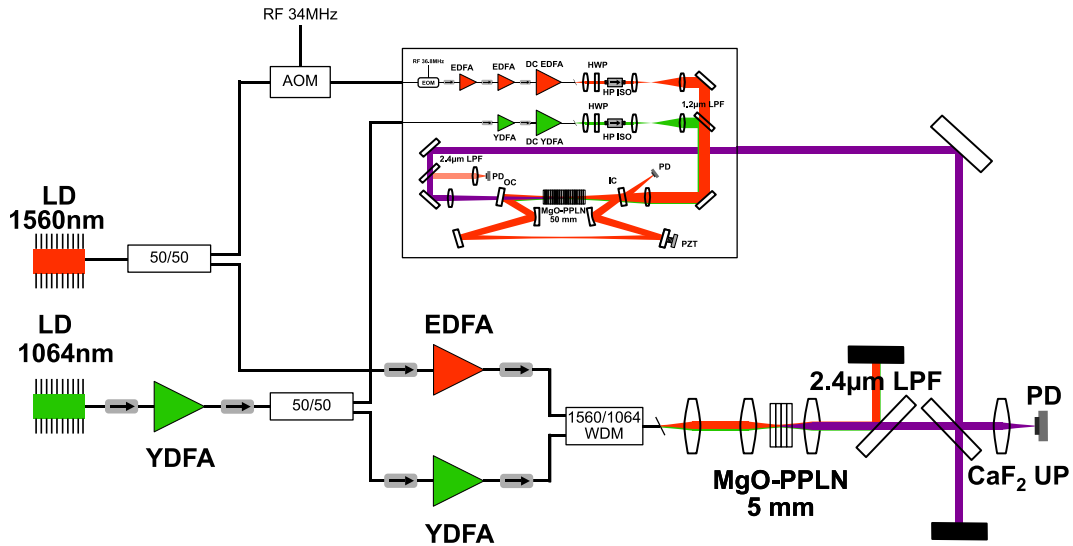


Figure 2.39: Experimental setup of the second DFG source for beat detection. CaF₂ UP: CaF₂ uncoated plate.

The 1.5- μm fiber amplifier, composed of 3.5 m of erbium-doped fiber (Coractive ER35-7), amplifies the signal from 2 mW to 210 mW. The 1- μm fiber amplifier, composed of 29 cm of DF-YB-6/128S-PM fiber from Coractive, increases the power level from 187 mW to 660 mW. After isolation, both amplified radiations are combined in a WDM and outcoupled in free-space through a connectorized FC/APC end fiber. A pair of lenses is placed to collimate ($f = 30$ mm) and focus ($f = 75$ mm) the beams into the crystal with a beam size of 30 μm (radius) at the focal point. The crystal, a 5 %-doped MgO-PPLN, dimensions of 5 x 1 x 10 mm, is placed in an oven mounted onto a 3D translation stage. As the available poling period for this new crystal was 29.95- μm , the temperature of the oven was set at 177.7 $^{\circ}\text{C}$ to reach the phase matching. The output beams are collimated using a CaF₂ lens ($f = 25.4$ mm) and the 3- μm radiation is separated from the non-converted 1- μm and 1.5- μm by a 2.4- μm long-pass filter.

To combine the two 3- μm beams from the cavity-enhanced DFG source and from the single-pass DFG source, an uncoated CaF₂ plate (90 % transmission) is placed at the crossing of the two 3- μm beams. As the power of the 3- μm radiation from the second source is weak (estimated to a few μW), the plate is used in transmission for the second source 3- μm radiation and in reflection for the high-power cavity-enhanced 3- μm radiation. The two beams are then focused onto a mid-IR photodiode (VIGO 4TE-5, 100-MHz bandwidth) through a CaF₂ lens ($f = 75$ mm). With such a weak power level, the alignment of the 3- μm radiation coming from the second source was achieved with the help of a lock-in detection. Once this arm was

aligned, the cavity-enhanced beam was aligned to spatially overlap the first arm. Analyzing the RF spectrum of the photodetector signal, a clear beat signal was visible (see Figure 2.40, the AOM was set at 37 MHz).

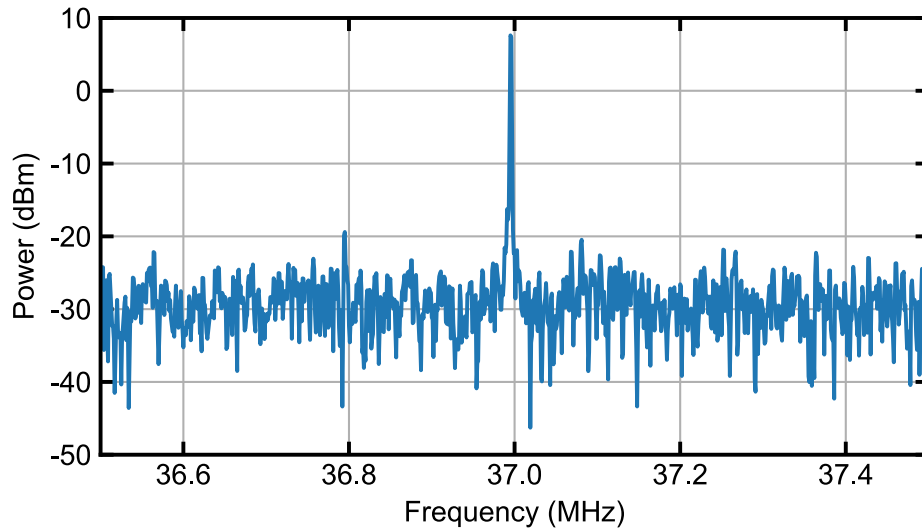


Figure 2.40: 3- μm beat note detected between the two DFG sources with a resolution bandwidth of 1 kHz. After the photodetector, the electrical signal is filtered (high-pass filter at 27.5 MHz and low-pass filter at 48 MHz) and amplified.

As a result of its relatively unstable amplitude, the beat signal was difficult to analyze. In order to enhance the beat signal for noise characterization, it was filtered and amplified using a tracking oscillator filter. This was realized by mixing the beat signal with the RF signal from a voltage controlled oscillator (VCO, central frequency $f_c = 204$ MHz) frequency-divided by a factor of 6 to $f_c = 34$ MHz to match the AOM frequency to generate a phase error signal corresponding to the relative phase fluctuations between the VCO and the beat signal. This error signal was input into a PID servo controller acting onto the VCO voltage to tightly lock the VCO onto the beat frequency (see Figure 2.41). The output of the VCO (after the frequency division) constitutes a filtered and amplified copy of the beat signal (within the PID loop locking bandwidth of around 500 kHz) that is much more stable in amplitude and which was used for noise analysis (see Figure 2.42).

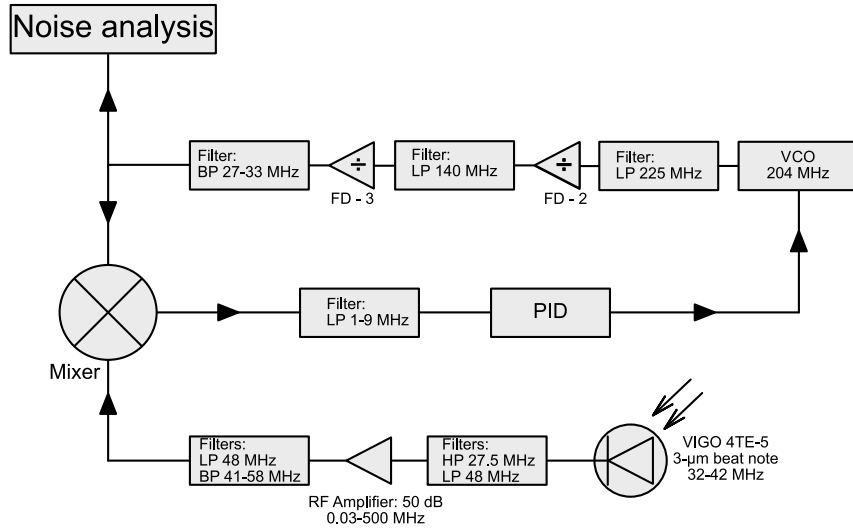


Figure 2.41: Enhancement of the 3- μm beat note with a tracking oscillator filter. HP: high-pass filter, LP: low-pass filter, BP: band-pass filter; FD: frequency divider (followed by the dividing factor).

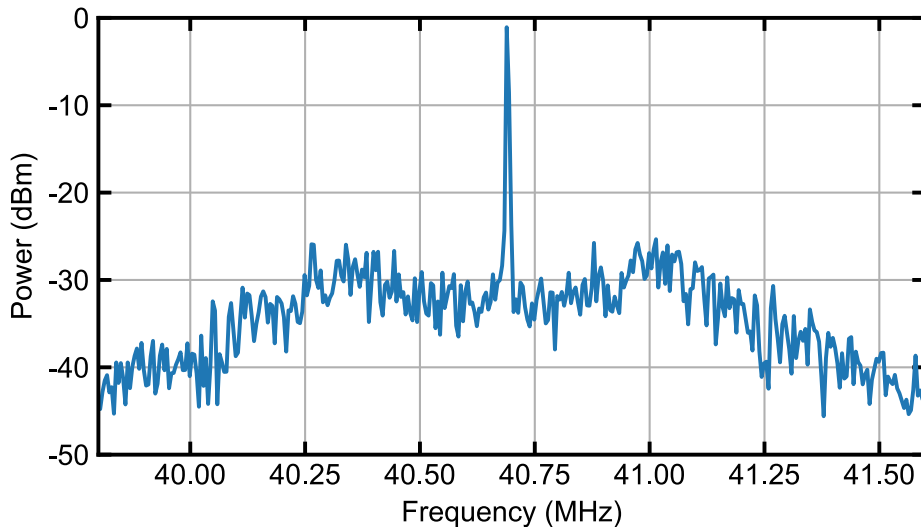


Figure 2.42: VCO signal (after frequency division) locked on the 3- μm beat note (central frequency 40.69 MHz), resolution bandwidth: 1 kHz.

The locked VCO signal was analyzed with a phase-noise analyzer (Rohde & Schwarz FSWP26) to measure its phase noise over a large range of Fourier frequencies (up to 1 MHz).

Table 2.4 summarizes the power performance achieved in the different experiments reported in this thesis. The performance of the fiber amplifiers

were presented in subsections 2.1.2.1 and 2.1.2.2. The highest measured 3- μm power corresponds to the results described in subsection 2.3.2.2, as well as the 3- μm power corresponding to the highest efficiency. The experimental conditions for the 3- μm beat note characterization correspond to the current subsection.

Fiber amplifier (see subsection 2.1.2.1 & 2.1.2.2)	
1 μm	30 W
1.5 μm	4.7 W
DFG (highest power, see subsection 2.3.2.2)	
7.5 W @1 μm	120 mW @3 μm
2.3 W @1.5 μm	
DFG (highest efficiency, see subsection 2.3.2.2)	
4.3 W @1 μm	113 mW @3 μm
1.4 W @1.5 μm	
DFG (beat note, see subsection 2.4.2)	
2 W @1 μm	30 mW @3 μm
2 W @1.5 μm	

Table 2.4: Summary of the power performance achieved for the different configurations of the DFG setup presented in this thesis.

2.4.3 Noise analysis

2.4.3.1 Frequency noise analysis

As previously stated, the linewidth determination of the 3- μm signal from its frequency noise PSD is based on the β -separation line method, presented in Chapter 1.

The frequency noise PSD of the beat-note between the cavity-enhanced 3- μm and the second source of 3- μm radiation is the sum of the non-correlated noise originating from every component of the setup influencing the pump or the signal frequency. As the two 3- μm sources share the same seed laser diodes, their noise contribution is common in the two generated 3- μm signals and cancels out in the beat signal. The frequency noise of the 1- μm and 1.5- μm laser diodes was thus separately

measured from their respective beat note with an optical line of a supercontinuum spectrum from a fully-stabilized frequency comb (OFC250 from Menlo System) to assess their contribution to the overall noise and linewidth of the 3- μm light. In addition to the noise of the laser sources, other components in the overall setup can add extra noise to the 3- μm beat signal. For example, the high phase-noise of an AOM RF driver (see Figure 2.43) initially used in a first implementation of the setup was totally limiting the measurement of the 3- μm frequency noise for Fourier frequencies below roughly 1 kHz.

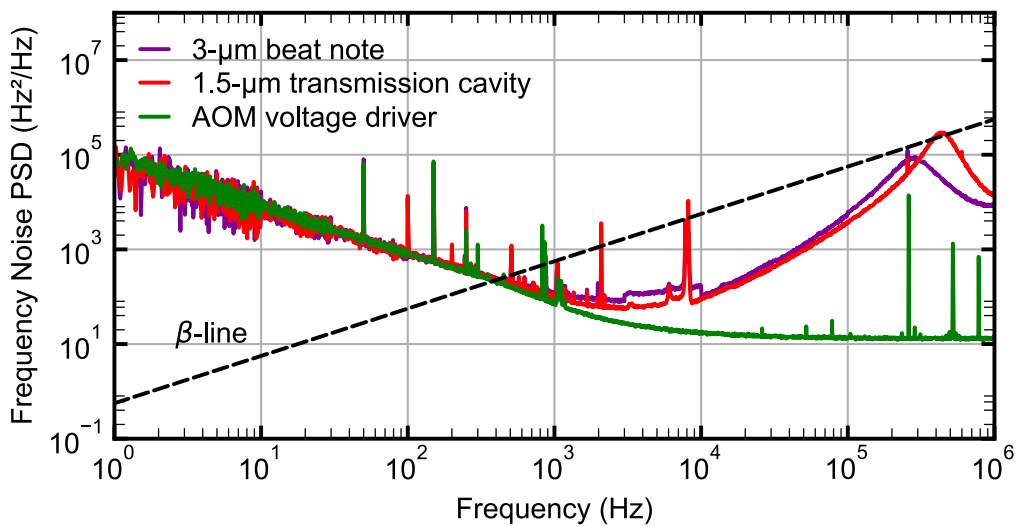


Figure 2.43: Frequency noise spectra of the 3- μm beat note in purple, of the 1.5- μm signal transmitted through the cavity in red and of the AOMRF driver in dark green. The difference between the 3- μm and 1.5- μm curves around 400 kHz originates from the different setting of the PID of the VCO used in the two measurements.

Integrating this 3- μm frequency noise above the β -separation line leads to an FWHM linewidth of 100 kHz approximatively. By changing for a less noisy AOM RF driver, the measured 3- μm frequency noise was drastically decreased (see Figure 2.44). The bumps around $4 \cdot 10^5$ Hz in the 3- μm and 1.5- μm FN spectra are the signature of the VCO servo-loop.

By performing a beat note between the output of the fiber amplifiers and the laser diode sources, respectively at 1064 nm and 1560 nm, the additive frequency noise of each amplification chain was evaluated. Figure 2.44 displays the additive frequency noise spectra.

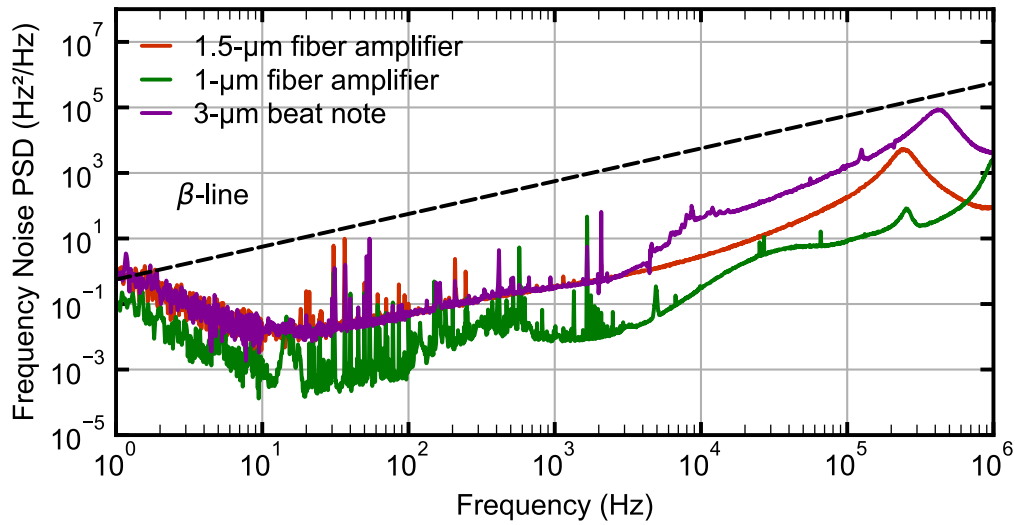


Figure 2.44: Frequency noise spectra of the fiber amplifiers at 1560 nm in dark red and at 1064 nm in dark green and of the 3- μm beat in purple.

The 3- μm beat frequency noise spectrum is almost entirely below the β -separation line and follows the noise spectrum of the 1560-nm amplifier. This means that the noise contribution of the cavity and of the non-linear conversion in the crystal is negligible. The overall system frequency noise is mainly limited by the laser sources. Above 5-kHz Fourier frequencies, a bump and a few peaks are visible in the 3- μm FN spectrum. By increasing or decreasing the gain of the servo loop of the piezo-locked cavity, the bump increased or decreased as well. The piezo movement inside the cavity has an influence on the cavity FSR (for the resonance to be maintained and thus the intracavity power to remain high) and should not have any influence on the 1560-nm frequency. An intensity-to-frequency conversion might occur inside the crystal.

The frequency noise of the 1- μm and 1.5- μm laser sources was assessed by detecting a beat note between each laser and a corresponding line of a stabilized frequency comb (OFC-250 from Menlo Systems), whose linewidth is estimated at 180 kHz at 1.5 μm and 440 kHz at 1 μm . From the measured frequency noise spectra depicted in Figure 2.45, the linewidth of the 1.5- μm Eblana diode was estimated at 700 kHz for an integration between Fourier frequencies of 1 Hz and 1 MHz and the linewidth of the 1- μm laser diode was estimated at 780 kHz. For comparison, the datasheet of the 1.5- μm Eblana laser specified a linewidth of 150 kHz.

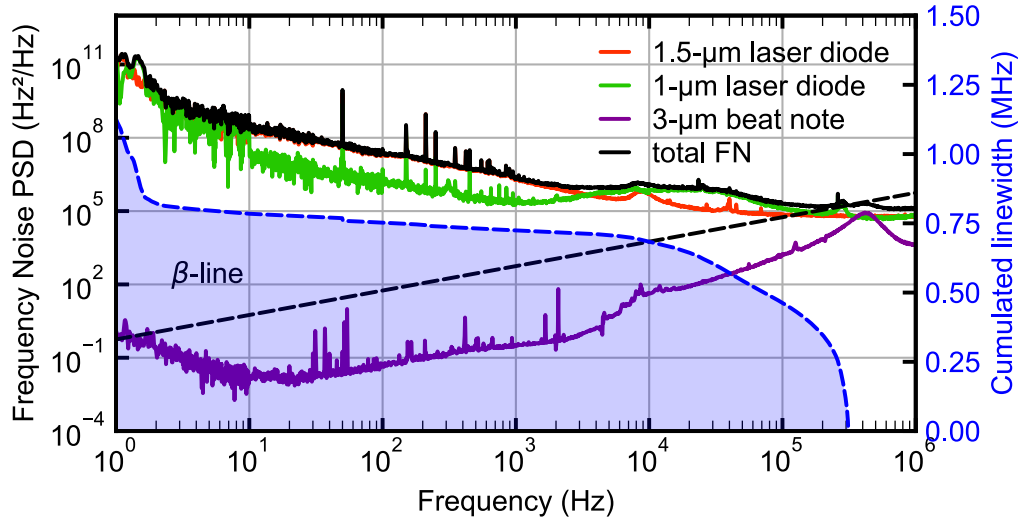


Figure 2.45: Frequency noise spectra of the laser diode at 1560 nm in red, at 1064 nm in green, of the 3- μm beat (contributions of the fiber amplifiers and cavity) in purple and calculated total frequency noise in black. In blue, the estimated linewidth calculated from the β -separation line (right scale).

The total frequency noise of the cavity-based 3- μm DFG radiation was calculated as the sum of the frequency noise PSDs of the two laser diodes and of the 3- μm beat signal that contains the extra noise induced by the amplifiers and cavity, as depicted in Figure 2.45. From the β -separation line concept (see Chapter 1), the linewidth (FWHM) of the 3- μm radiation is estimated at 1.1 MHz (integration from 1 Hz to 1 MHz). This is higher than state-of-the-art DFG-based sources, as C.C. Liao et al. reported a 100-kHz free-running linewidth [55] and more recently, H. Sera et al. reported a few hertz linewidth DFG-based source locked to a stabilized optical frequency comb [29]. The interest of the result reported here resides in the complete frequency noise analysis of the setup, which shows a small contribution of the servo-loop of the cavity (around 10 kHz) and a negligible contribution of the frequency conversion process.

2.4.3.2 Intensity noise analysis

As previously mentioned, the generated 3- μm power was rather unstable over time. The power stability was studied at two time-scales: at long time scale, for measurements longer than 1 second, it was characterized in the time domain, and at short time scale for measurements ranging from 1 Hz to 1 MHz, it was characterized in the frequency domain.

For time scales over 1 second, the power level stability of the 3- μm radiation depends strongly on the 1- μm and 1.5- μm power levels. Typically, for pump and signal powers below 1 W each, the resulting 3- μm power is varying in a range of 10 % of its average value. This power stability is considered as acceptable for the present experiment but should be improved for experiments like gas-phase absorption spectroscopy. For higher pump and signal levels, the 3- μm power becomes fairly unstable as depicted in Figure 2.46.

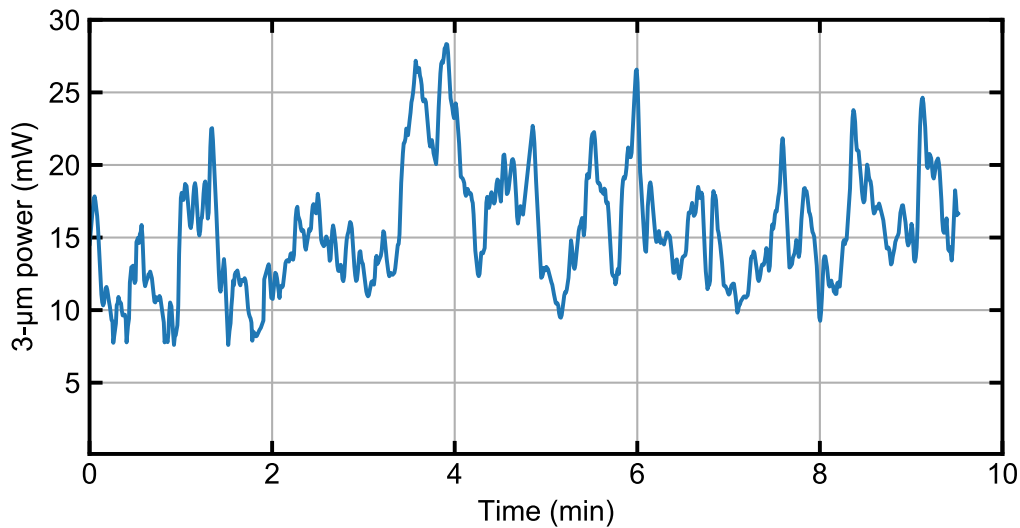


Figure 2.46: DFG power instabilities for 2 W of pump at 1064 nm and 1.7 W of signal at 1560 nm. Time resolution: 1 point/s.

In this case, the 3- μm power was set initially at 20 mW but evolved varying over a range of 15 mW (10 mW to 25 mW). By re-aligning both beam lines (and re-locking the 1.5- μm resonant cavity), the initial power level was restored, but was rapidly varying strongly around its mean value. Such high instabilities can be mainly explained by the pointing instabilities at the output of the fiber amplifiers at 1 μm and 1.5 μm , resulting from insufficient thermal management of the setup. Indeed, the DFG efficiency is closely related to the overlap between the pump and signal beams, pointing instabilities from both 1- μm and 1.5- μm lines end up in the deterioration of the 3- μm stability. This effect is predominant for the intensity noise over the long time scale. One solution, for future improvements, consists in using a high-power fiber collimator including an aspheric lens mounted in one piece with a metallic ferrule at the end tip of each fiber amplifiers for an optimized thermal management. Such robust system could resolve the pointing instabilities issue. Other effects

influencing the 3- μm power like polarization state instabilities could be spotted after the fiber amplifiers, but compared to the signal and pump beam pointing instabilities, their impact was lower.

For the 3- μm power variations at frequency ranging from 1 Hz to 1 MHz, the relative intensity noise (RIN) is measured using the same phase-noise analyzer than for the frequency-noise measurements. RIN is measured from different part of the cavity for a complete analysis and sum-up of the RIN of the system is depicted in Figure 2.47.

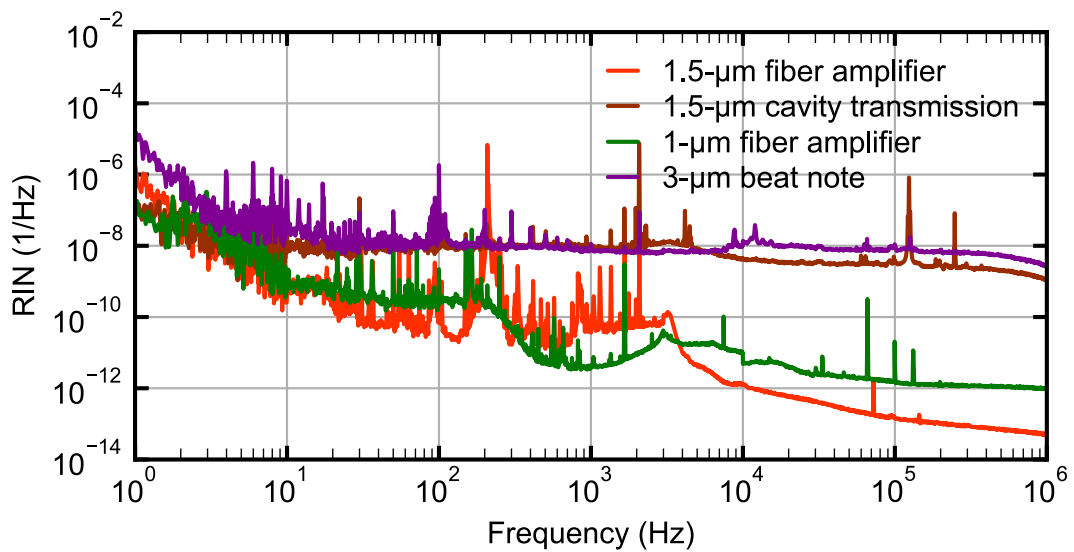


Figure 2.47: RIN spectra of the radiation at the output of the fiber amplifiers at 1064-nm in green and 1560-nm in bright red, of the signal in transmission of the cavity in dark red and of the 3- μm radiation in purple.

The RIN of the 3- μm radiation (0.54%) is very low for Fourier frequencies going from 1 Hz to 1 MHz, and is mainly driven by the intracavity 1.5 μm RIN and then, depends strongly on the quality of the piezo-locked cavity servo loop. The RIN from the 1- μm and 1.5- μm signals directly out of the fiber amplifiers is measured decades below the cavity transmitted 1.5- μm signal. The transfer function of the loop with the piezo was measured with a cut-off frequency around 10 kHz. This value corresponds to the weak bump in the RIN of the 3- μm radiation in Figure 2.47, but can be shifted depending on the PID parameters, as depicted in the RIN of the 1.5- μm signal in transmission from the cavity, where the bump can be spotted around 1.5 kHz (the two measurements were achieved with different PID parameters). In comparison to the long time-scale stability, the 3- μm power is rather stable in the high frequencies domain.

Conclusion

To conclude, a noise characterization was achieved by analyzing the beating note between a high-power (more than 120 mW) continuous-wave cavity-enhanced difference frequency generation-based source driven by two fiber amplifiers operating at 1064 nm and 1560 nm, and a single-pass DFG source seeded by two fiber amplifiers operating at the same wavelengths. As the two systems were seeded by the same laser diodes, the additive frequency noise of the fiber amplifiers, the crystal and the cavity was characterized. It is shown that only the frequency noise of the laser diode (at 1064 nm and 1560 nm) contribute to the linewidth of the mid-IR radiation (evaluated to 1.1 MHz). Using lower noise laser sources at 1 μm and 1.5 μm (in terms of frequency noise) in the reported setup would lead to an ultra-narrow linewidth and powerful 3- μm source which would constitute a highly attractive source for state-of-the-art spectroscopic experiment.

Chapter 3

High harmonic generation in an ultrafast thin-disk laser oscillator

Introduction

XUV coherent light sources constitute very beneficial tools in many scientific areas. They are commonly used in X-ray imaging [56], biology and biochemistry [57–59] or in fundamental physics [60,61]. Among the different possible coherent sources of XUV light, HHG holds a special place as it can emit optical frequencies ranging from 1 eV to more than 1.6 keV [62] and in contrary to synchrotron sources, can still fit onto an optical table [63,64] which makes it far less expensive and more accessible. As introduced in Chapter 1, HHG appears when an intense electric field interacts with an atomic or molecular gas jet (HHG can also be produced from laser interacting with solid surfaces or even in liquids [65–67]). The laser intensity required to produce HHG is ranging from a few 10^{13} W/cm² to a few 10^{14} W/cm² depending on the considered gas. With such a broad emission spectrum of coherent light, the HHG enabled the generation of attosecond-scale pulse durations [68–70].

Since the first HHG demonstration in the eighties [63,64], the research effort to develop high-XUV-flux table-top HHG sources is still strong. The most common scheme for HHG involves a Ti:sapphire chirped pulse amplifier as laser source, operating usually with mJ-pulses, at kHz repetition rates and a few watts average power [71]. HHG with higher repetition rates, in the MHz range, is beneficial for many experiments like

electron-ion coincidence spectroscopy [72,73] and microscopy [74] by highly decreasing the measurement time and enhancing the signal-to-noise ratio of applications with fast recovery dynamics (below the μs). The HHG process displays a very low conversion efficiency. The highest HHG efficiency reported to date is 7.5×10^{-5} for a single harmonic [75], while most of other systems operate in the range of 10^{-7} - 10^{-6} . For systems based on Ti:sapphire lasers operating in the watt-level, the average XUV power is about a few nW to a few μW . For applications involving high resolution imaging, the XUV photon flux impacts directly on the acquisition time and resolution [76,77]. For frequency comb spectroscopy, both MHz repetition rate for a well-resolved comb combined with high average power for enough power in each line are required [78,79].

Changing from a Ti:sapphire to a diode-pumped solid-state laser geometry allowed laser sources to reach average powers of multiple hundreds of watts with sub-picosecond pulses. Slab lasers [80], coherently-combined fiber chirped-pulse-amplifiers [81,82] and ultrafast thin-disk laser oscillators [83–86] can provide enough power to enable HHG at MHz repetition-rate with however the use of a nonlinear pulse compression [87,88]. Femtosecond enhancement cavities can also be used to enhance the average and peak-power of MHz ultrafast laser sources [89]. By coherent addition of the optical pulses inside a passive cavity with an enhancement factor ranging from 100 to 10 000, a few kW of intra-cavity average power with pulses in the femtosecond range is possible. This approach allowed in 2005 the realization of the first MHz-repetition-rate HHG [90,91]. A femtosecond enhancement cavity HHG-based system demonstrated the generation of XUV light with a photon energy above 100 eV at a repetition rate of 250 MHz [92]. Furthermore, this approach has resulted in the generation of XUV photon flux up to several hundred μW in a given harmonic [25,26]. However, the experimental realization of this approach is highly complex. Stable coupling of fs-pulses from an amplified frequency comb into a high-finesse resonator containing the HHG interaction is challenging. In addition, the requirements on the phase stability of the driving laser system are very demanding.

Placing the HHG interaction directly inside a modelocked laser oscillator appears as a simpler approach that does not require any input matching of ultrashort pulses. Instead, the oscillating fs-pulse can adapt to the present cavity nonlinearities and dispersion. In 2012, the feasibility of this concept was demonstrated using a Ti:sapphire laser oscillator [93], but only at an intracavity average power of 10 W. Due to thermal effects and nonlinearities, ultrafast lasers using bulk crystals, such as Ti:sapphire, are severely limited in average power. This is not the case for ultrafast thin-disk laser (TDL) oscillators. Here the gain medium has the shape of a thin disk

(typically 100 μm to 200 μm thick), which is mounted onto a heat sink and used in reflection with a large beam diameter [83,94]. Ultrafast TDL oscillators have achieved the highest average power and pulse energy of any modelocked laser oscillator, both intra- and extra-cavity [84,85,95]. Intracavity peak powers up to 1.76 GW have been generated [96]. Recently, ultrafast TDL oscillators based on Yb-doped gain materials achieved pulse durations as short as 30-fs directly emitted from the oscillator [97,98]. Furthermore, they can operate with low noise and carrier-envelope offset (CEO) frequency stabilization has been achieved [99–102], showing their suitability for frequency comb applications.

In this chapter, the first demonstration of HHG inside an ultrafast TDL oscillator is presented. In section 3.1, an introduction to modelocked thin-disk lasers is given, where the advantages of the thin-disk geometry, the basics of modelocking and the choice of the disk material are explained. Section 3.2 presents the different steps toward modelocked thin-disk oscillator with enough intracavity peak power for HHG. Starting from the modelocking of an ytterbium-doped CaAlGdO_4 (Yb:CALGO) thin-disk laser, different cavities and configurations are presented. The final cavity using an ytterbium-doped lutetium oxide $\text{Yb}^{3+}:\text{Lu}_2\text{O}_3$ (Yb:LuO) disk was chosen for HHG operation. Finally, HHG inside a modelocked cavity based on an Yb:LuO thin-disk is detailed in Section 3.3. With the implementation of a tight focus extension inside the cavity and a gas nozzle, high harmonics were produced and detected.

3.1 Modelocked thin-disk lasers

In this sub-section an overview of the basic principles of modelocking of thin-disk lasers is given. Starting from the specifications of the thin-disk geometry, the most commonly used materials are then presented and finally the modelocking principle is described.

Lasers can be realized in many forms and their core element, the gain medium, can consist of material in all different state of matter, as solids, liquid or even gases. However, solid-state configurations are the most extensively used in research today to perform state-of-the-art experiments, owing to the high quantum efficiency, precise control of the crystal lattice enabling optimized quantum transitions, as well as for the better stability and ease of experimental implementation.

The need for fundamental science to resolve ultrafast events (e.g., molecule breaking dynamics) drove the development of laser sources able to emit pulses as short as a few femtoseconds ($1 \text{ fs} = 10^{-15} \text{ s}$). Focusing such a laser beam enables reaching very intense electric fields, allowing the study, of, e.g., the interaction of matter with light or heatless matter-ablation.

As previously mentioned, the most commonly used ultrafast solid-state lasers for this type of applications are titanium-doped sapphire (Ti:sapphire) lasers. Such systems can deliver pulses with a duration of a few femtoseconds with a few hundreds of milliwatts of average power [103]. They have already demonstrated GW of peak power, after amplification and pulse compression, for repetition rates of a few hundreds of kHz. Even though those performances allow reaching sufficient intensity to realize strong field physics experiments such as HHG, these laser systems suffer from some limitations.

The Ti:sapphire material exhibits a good thermal conductivity ($33 \text{ W}/(\text{m}\cdot\text{K})$ at 5 at.%), allowing the crystal to withstand a few watts of green pump power. However, this configuration presents many disadvantages. The large energy difference between the pump photons and laser photons (quantum defect) in

Ti:sapphire leads to heat generation and the classical bulk laser geometry of the pumping system does not allow increasing the power level, therefore limiting the achievable average and peak powers. Moreover, the amplification and compression stages add a severe complexity and cost increase to the already expensive system. They also limit the repetition rate to typical values of hundreds of kHz.

To overcome these limitations, different technologies have been developed: slab amplifiers [80], TDL oscillators, fibers and regenerative amplifiers [104]. All these geometries are based on an efficient heat removal in the gain medium through an optimized surface-to-volume ratio. This chapter focuses on the thin-disk laser geometry.

3.1.1.1 The thin-disk geometry, an efficient heat removal

The concept of the thin-disk was introduced for the first time by A. Giesen et al. [94] in 1994. It consists of a thin-disk-shaped gain medium (typical thickness of $100\ \mu\text{m}$) glued or soldered onto a heat sink (made of copper-tungsten or diamond) which is cooled on the back side by a water flow (see Figure 3.1). The disk is commonly placed into the laser cavity as a folding gain mirror. The rear side of the disk has a highly reflective (HR) coating for both the pump and the operating laser wavelength, whereas the front side has an anti-reflective (AR) coating at the same wavelengths. The pump beam diameter on the disk is much larger than the disk thickness, allowing a nearly one-dimensional heat flow and an effective and uniform heat removal. Typically, a thin-disk of ytterbium-doped yttrium-aluminum-garnet ($\text{Yb}^{3+}:\text{YAG}$) usually withstands pump intensities up to $5\ \text{kW}/\text{cm}^2$ without laser operation.

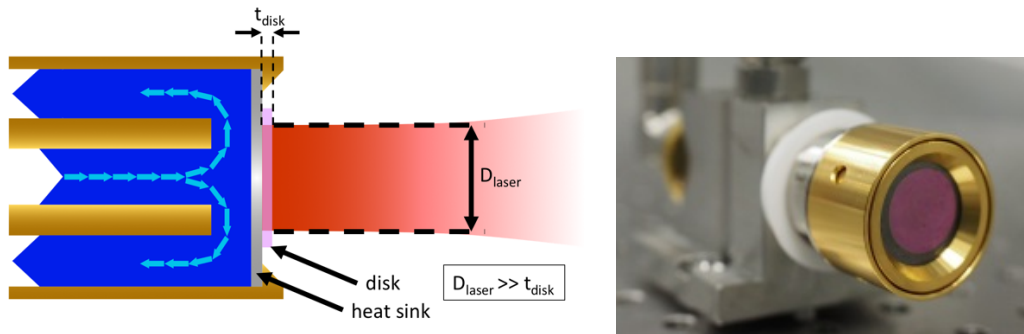


Figure 3.1: Left: the cooling principle of a thin-disk gain medium. Right: thin-disk contacted on a diamond heat sink and mounted on cooling finger.

As the gain medium is very thin, the pump absorption per pass is very limited (to approximately 10%). A. Giesen et al. [94] proposed a configuration where the pump beam is reflected onto several mirrors and passes many times through the thin disk (see Figure 3.2). Thin-disk laser heads, now commercially available, are composed of a parabolic mirror and several plane mirrors, which focus the pump beam onto the disk 24, 32 or even up to 48 times. Owing to this particular geometry, the pump beam is recycled and the pump absorption during laser operation is commonly enhanced to 90%. The pump beam is usually delivered by a highly multimode optical fiber. It is collimated through collimation optics and

imaged on the disk by the parabolic and plane mirrors. Non-fiber-coupled systems are also used sometimes. Resulting from the overlap of several highly multimode beams, the pump beam profile is shaped as a homogenized flat-top profile onto the disk.

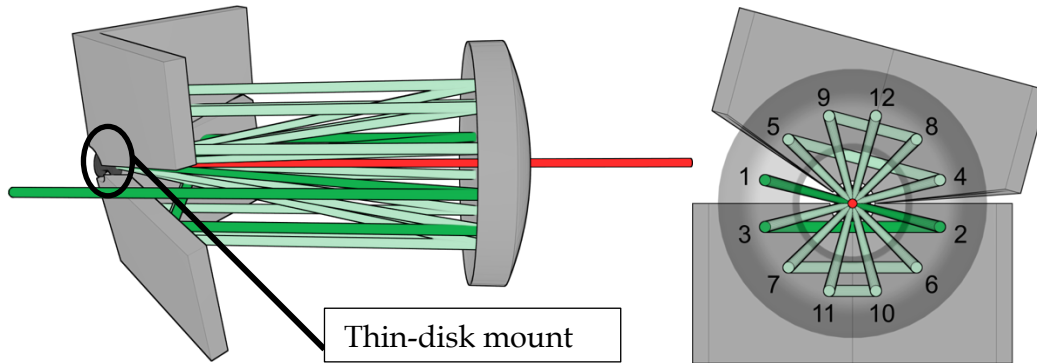


Figure 3.2: Illustration of the multiple pump pass geometry of a thin disk laser. The disk mount is displayed in dark gray (as labelled) and the mirrors in light gray. The pump beam is pictured in green and the laser beam in red. In this example, 12 passes through the disk are shown.

3.1.1.2 Power scaling of the thin-disk technology

In addition to the efficient heat removal and the high absorption of the pump, the thin-disk concept has the advantage of being power scalable. Indeed, one of the major limiting factors of this concept is the maximum pump intensity that can be applied to the disk. This value depends on various parameters such as the disk surface, coating quality and the thermal conductivity of the material. By scaling-up the pumped disk area, the applicable pump power can be increased while keeping the same intensity on the disk, which enhances the laser performance. However, increasing the disk size while keeping a small thickness results in some other limitations. The production, polishing and coating of large (above 10 mm in diameter) thin disks with a high quality is difficult. Furthermore, large laser heads supporting high pump power operation (above 2 kW of pump power for example) are expensive.

An important effect in terms of laser cavity stability and alignment is the thermal lensing. TDLs display a rather low thermal lensing sensitivity compared to the other geometries. It affects the power scalability, and directly results from the low thickness of the disk combined with the huge thermal load it has to withstand. Indeed, under high pumping levels, part of the pump power is converted into heat inside the disk and, if not correctly evacuated by the cooling system, tends to deform the disk surface through many effects like thermal expansion of the material and modification of the

refractive index. These effects depend both on the properties of the heat sink and of the gain material. Two types of heat sinks made of copper-tungsten and diamond have been used in this work, with the thin disks glued on top of the heat sink. With its higher thermal conductivity, the diamond mount was chosen for high power operation. The thermal conductivity of the gain medium depends on the combination of host material parameters and the doping ion, ytterbium for the present work. A comparative table in the next section (see Table 3.1) presents the different types of host materials doped with ytterbium commonly used in TDLs. The combination of a good heat-sink with a high-thermal conductivity gain material ensures a proper high-power laser operation.

3.1.1.3 Broadband materials for high-power, ultrashort thin-disk lasers

Despite the large and increasing number of materials adapted to the thin-disk configuration, only a few can compete with Yb:YAG (see [94]). In this thesis Yb:CALGO and Yb:LuO were used owing to their very interesting properties with respect to the requirements of the targeted experiment.

The first gain material used in thin disks was Yb:YAG [94] because of its properties suitable for high-power and diode-pumping capability. Indeed, the material exhibits a low quantum defect when pumped at 970 nm (91% of slope efficiency), high doping levels without quenching, pump wavelength of 970 nm (achieved with high power InGaAs pump diodes) and a high thermal conductivity. In comparison to the commonly used Nd:YAG, Yb:YAG displays a much larger gain bandwidth, a longer upper-state lifetime and a better thermal conductivity. Owing to these remarkable features and to the long and proven development time of disk manufacturing, Yb:YAG thin disks hold the record of the highest output power (275 W) emitted out of any passively modelocked laser oscillator with a pulse duration in the femtosecond regime [84]. Using Yb:YAG Kerr-lens modelocking, pulse durations as short as 49 fs has been achieved with an output power of 3.5 W [111] as well as 120 W of output power with 350-fs pulse duration, corresponding to 4 μ J of pulse energy [106].

Yb:YAG led to a proven thin-disk laser technology, however its gain bandwidth limits the achievable pulse duration. Other gain materials have been investigated in order to overcome these limitations. Yb:CALGO and Yb:LuO are both very attractive for their large gain bandwidth and good thermal conductivity for the same doping level as Yb:YAG. Table 3.1 sums up the main properties of those materials.

Ytterbium-doped lutetium oxide (Yb:LuO) combines an excellent thermal conductivity with a large emission bandwidth (larger than Yb:YAG). It allows the material to support short pulses in combination with a high average power. In a first Semiconductor Saturable Absorber Mirrors (SESAM) -modelocked thin-disk-based demonstration in 2007, a pulse duration of 523 fs with an average power of 24 W was achieved with LuO [107]. Recently, a pulse duration down to 35 fs with an average power of 1.6 W was demonstrated at the LTF [108]. In another configuration, a 88-fs pulse duration LuO TDL with up to 11 W of average power was achieved with Kerr-lens modelocking [108].

Table 3.1: Comparison of the properties of different Yb-doped materials. The

Material	Yb:YAG	Yb:LuO	Yb:CALGO
Thermal conductivity (W/m·K)	7.0 (7 at.%)	12 (2 at.%)	6.9 (2 at.%)
Pump wavelength (nm)	940	976	979.5
Absorption cross-section (10^{-21} cm ²)	8	31	9
Absorption bandwidth (nm)	12.5	2.9	5
Emission wavelength (nm)	1030	1034	1051
Emission cross-section (10^{-21} cm ²)	19	12.9	8
Emission bandwidth (nm)	9	12	35

Yb:YAG pump wavelength is shown here at 940 nm for comparison where the absorption bandwidth is the larger. The zero-phonon line at 970 nm is also commonly used for pumping thanks to the availability of reliable and stabilized sources at this wavelength.

On the other hand, Yb:CALGO constitutes as well a suitable solution for short-pulse, high-power thin-disk laser operation. The material displays, in addition to a fairly good thermal conductivity (comparable to YAG), an outstandingly large and almost flat emission cross-section in both polarizations [109] (see Figure 3.3), which allows for ultra-short pulse durations in modelocked laser operation. In its first demonstration in a SESAM-modelocked thin-disk laser in 2012 [110], an Yb:CALGO thin-disk gain medium achieved down to 135-fs pulse duration with an average power of 1.1 W, as well as 28 W of average power with 300-fs pulse duration.

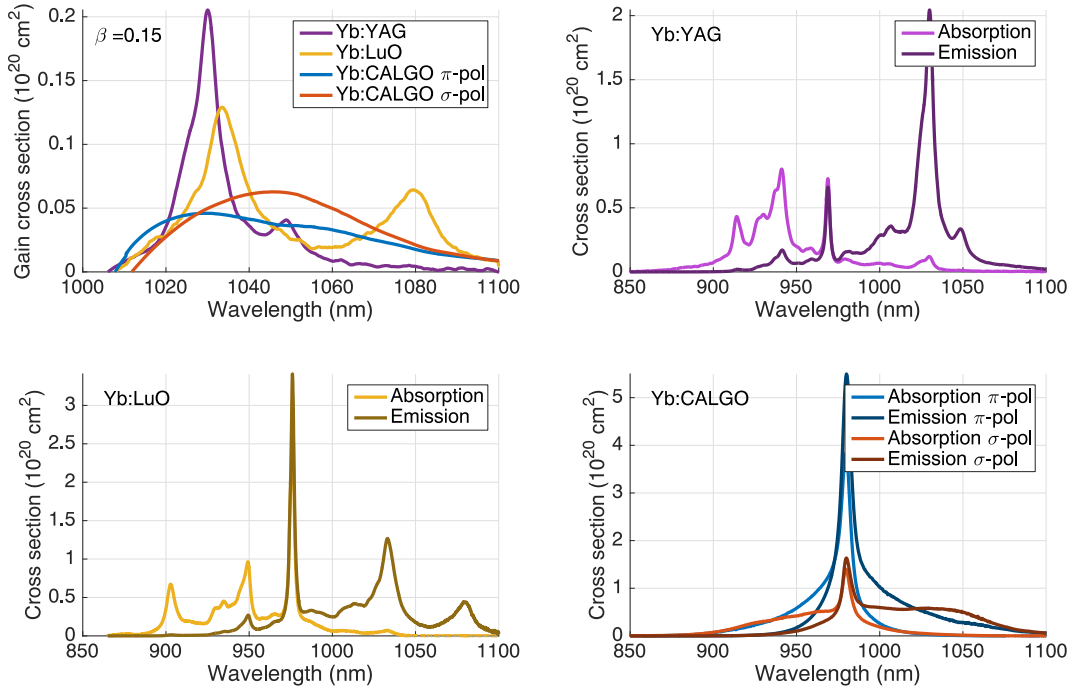


Figure 3.3: Up-left: Gain cross section of different Yb-doped materials. β represents the inversion level. Up-right and down: emission and absorption cross-section of different ytterbium-doped materials. For Yb:CALGO, the spectra corresponding to two different polarizations (π and σ) are displayed.

Nowadays, Yb:CALGO still holds the short pulse duration record of SESAM-modelocked TDLs [111] (49 fs with 2 W of average power, presented in section 3.2.1), as well as the shared record of any Yb-doped modelocked solid-state laser (including bulk lasers) with an Yb:CaYAlO₄ bulk oscillator [112] (30 fs with 15 mW of average power) and a Kerr-lens modelocked CALGO bulk oscillator [113] (32 fs with 90 mW of average power). Indeed, the first demonstration of a Kerr-lens modelocked CALGO TDL realized in at the LTF at the University of Neuchâtel equalized this values [98] with even slightly higher average power (30 fs with 150 mW of average power).

Owing to their outstanding properties, Yb:CALGO and Yb:LuO constitute solid candidates for the generation of pulses enabling HHG inside the laser oscillator. Cavities based on those materials are investigated in the following sections.

3.1.1.4 Soliton modelocking

Amongst the different ways for a laser to produce short and energetic pulses, continuous-wave (cw) modelocking is the most stable method. Literally, “modelocking” refers to the laser operation in which the different resonating longitudinal modes (or frequencies) of the cavity oscillate in phase. The “locking” is achieved by maintaining the phase of the cavity modes such that they interfere constructively at a certain time resulting in a short pulse. In cw modelocking, the pulse experiences some modification through gain and loss effects, dispersion, nonlinearities, etc. as it travels inside the cavity but always retrieves its initial state at a certain position in the cavity.

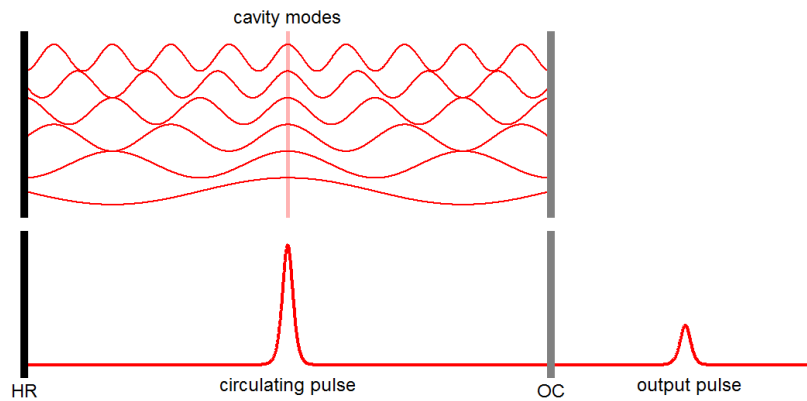


Figure 3.4: Modelocking principle: the longitudinal modes displayed in the upper part interfere constructively (in phase) at a certain position in the cavity and destructively at other positions, leading to the creation of a short pulse that oscillates in the cavity (bottom).

Another pulsed laser operation is to be noted due to its importance: the Q-switched modelocking operation (see Figure 3.5). It consists of modelocked pulses shaped into a periodic Q-switched envelope with a typical frequency in the kHz region. The Q-switched modelocking was actually discovered since pulsed laser operation could be characterized (in the mid-1960s) [114]. Due to its unstable pulse energy and repetition rate, Q-switching is considered as an unwanted laser regime in the frame of this thesis. In the past, before the introduction of semiconductor saturable absorbers with Ti:Al₂O₃ (titanium doped sapphire) gain material (in the 1980s), dye lasers were preferably used over solid-state lasers because of Q-switching issues.

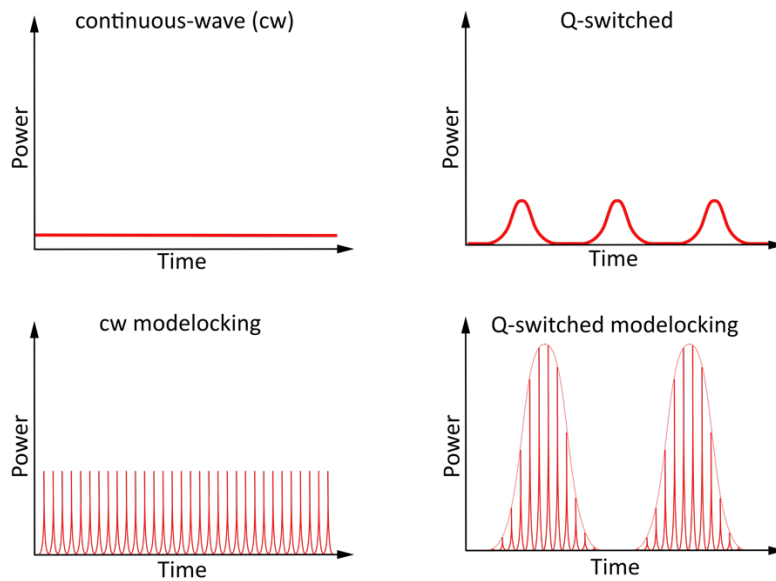


Figure 3.5: Different continuous and pulsed laser operations.

In order to operate in a pulsed regime, the laser cavity requires modulation of the laser gain and/or of the losses. The different methods of modelocking can be classified in two categories: active and passive modelocking. For the first one, an electrically-controlled modulator (typically an acousto-optic modulator) is inserted inside the cavity and modulates the losses, creating a temporal window inside which the pulses can experience more gain than losses and then propagate. But due to the limits of those components, pulse duration under few hundreds of femtoseconds is not achievable. Concerning passive modelocking regime, a passive element modulating the gain/losses is placed inside the cavity. In the frame of this thesis, passive modelocking using saturable absorbers is studied and used. It consists of a material for which the light absorption depends on the incident intensity. The more intense the light is, the less absorptive the material becomes. Its role is to start and stabilize the pulse formation. Starting from a cw operation, the laser operates at constant power over time, presenting however some natural small instabilities (noise peaks). Because of the saturable absorber, those peaks experience less losses and combined with a saturated gain, the energy from the cw operation decreases in favor of those noise peaks. Over many passes inside the cavity, the same combination of saturable absorbance with saturated gain causes the highest peak to be favored over the smallest ones until one peak remains, which forms a short pulse. In the time domain, the more modes participating to the pulse construction, the shorter the pulse becomes. The

pulse experiences a reduction of its temporal width until broadening effects like dispersion limit the pulse duration.

In the process described above, one of the key elements for passive modelocking is the saturable absorber. SESAMs are the most widely used elements to achieved passive modelocking. They came in replacement of dye saturable absorbers, unsuitable for solid state lasers. SESAMs consist of a distributed Bragg reflector (DBR) acting as a mirror above which are grown layers of quantum dots or quantum wells acting as a saturable absorber. The SESAMs important parameters such as the wavelength range, the absorption recovery time, the saturation fluence, etc... are carefully controlled by the design and the growth of the device. Depending on the wavelength range, different materials are used. At near infrared wavelengths (870 nm to 1150 nm), an indium-gallium-arsenide (InGaAs) quantum well is used as saturable absorber. This type of SESAM is used in the cavities presented in this thesis.

On a macroscopic point of view, the nonlinear reflectivity of the SESAM (depicted in Figure 3.6) is described by the fluence-dependent reflectivity curve $R(F)$:

$$R(F) = R_{ns} \frac{\ln \left[1 + R_{lin} / R_{ns} \left(e^{F/F_{sat}} - 1 \right) \right]}{F/F_{sat}} e^{-\frac{F}{F_2}}$$

R_{ns} represents the reflectivity of the highly saturated device, if the roll-over in reflectivity for high probe fluences F is disregarded. This parameter is used for the determination of the non-saturable losses. R_{lin} is the reflectivity for very low probe fluences and F_{sat} is the saturation fluence. The parameter F_2 describes the strength of induced absorption effects, with the most prominent being two-photon absorption when probing with femtosecond pulses. These effects lead to a roll-over in reflectivity for very high probe fluences and are strongly dependent on the probe pulse duration and the material composition of the SESAM. The reflectivity of the SESAM increases with the fluence of the incident light until multiphoton processes such as two-photon absorption limits the reflectivity, thus leading to a roll-over effect (see Figure 3.6). Femtosecond modelocked lasers operating in this regime typically experience multi-pulsing instabilities.

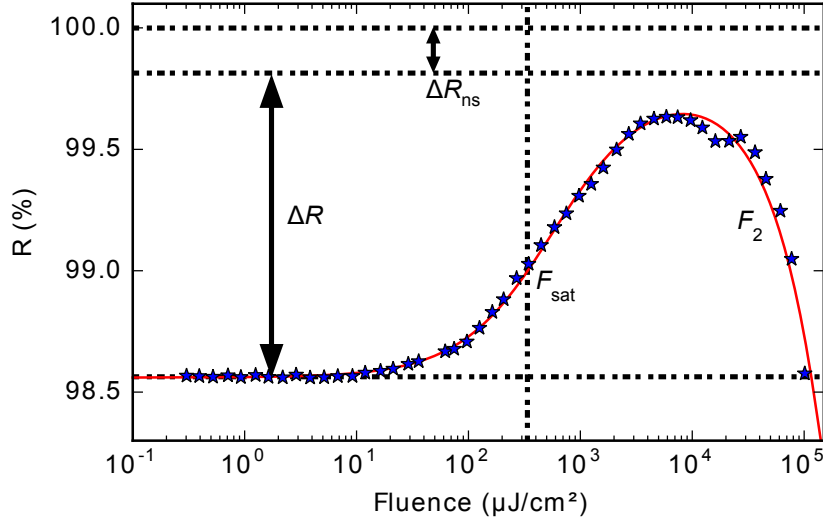


Figure 3.6: Typical nonlinear reflectivity of a SESAM with respect to pulse incident fluence. For this sample, $\Delta R = 1.3\%$, $F_{\text{sat}} = 334.6 \mu\text{J}/\text{cm}^2$, $\Delta R_{\text{ns}} = 0.14\%$ and $F_2 = 9031 \text{ mJ}/\text{cm}^2$ (its actual position is out of the graph but it is nevertheless indicated to highlight the strong drop in the reflectivity R).

The combination of SESAMs displaying a large modulation depth with large emission bandwidth gain materials (like Ti:sapphire) allowed passive modelocking to operate in a stable regime. By compensating the self-phase modulation (SPM) experienced by the pulse in the cavity with elements introducing negative group delay dispersion (GDD), a particular pulse is formed: a soliton. In comparison, active modelocking displays a gaussian pulse propagation. Soliton behavior in waves has already been observed in 1834, in the Edinburg-Glasgow canal [115]. A solitary wave formed after stopping a small boat could propagate over several kilometers. In the optical domain, the soliton pulse created in passive modelocking of solid-state lasers presents similar interesting features, i.e., a propagation with constant temporal and spectral shape as well as a strong stability against many sources of perturbations. The pulse propagation in medium with dispersion and Kerr-effect is described by the nonlinear Schrödinger equation (not-detailed here), and with some approximations (e.g. slowly varying envelope) an analytic steady-state solution is found. For a negative dispersion and a positive Kerr effect, that balance their contributions over the pulse, the steady-state solution is given by:

$$A_s(z, t) = A_0 \operatorname{sech}\left(\frac{t}{\tau}\right) e^{-i\phi_0},$$

with $A_s(z, t)$ the time-dependent amplitude of the electric field, A_0 the maximum amplitude, ϕ_0 the soliton phase, and τ a parameter linked to the

pulse duration: $\tau_p = 1.7627 \tau$ with τ_p the FWHM of the soliton pulse (in s). In intensity, the pulse has a $\text{sech}^2\left(\frac{t}{\tau}\right)$ dependence.

The pulse duration is given by the relation:

$$\tau_p = 1.7627 \frac{2|GDD|}{\gamma E_p},$$

With GDD the total negative group delay dispersion encountered by the pulse in a cavity round-trip (in s^2), γ the self-phase modulation coefficient (in rad/W) and E_p the pulse energy (in J). More details can be found in [116]. The time-bandwidth product of a perfectly unchirped soliton is equal to: $\Delta\nu_p \cdot \tau_p = 0.3148$ with $\Delta\nu_p$ the spectral full width at half maximum of the optical frequencies. The time-bandwidth product is often used to evaluate how much the measured pulse is close to the ideal soliton.

During the pulse formation previously described, many processes can occur. One noticeable process destabilizing the pulse and frequently observed in practice is Q-switching instabilities. Indeed, the highest energy levels are favored by saturable absorbance and saturated gain medium, leading to an exponential growth of the pulse energy until the same gain saturation limits the pulse energy or other components such as the SESAM with the rollover. The absorber and gain medium parameters influence the pulse energy towards damped or undamped oscillations. In the case of undamped oscillations, the pulses are shaped in a slow temporal modulation, in the kHz range leading to bunches of modelocked pulses, as depicted in Figure 3.5. High peak power from Q-switching operation can lead to damage of the cavity component and is then highly undesirable. The threshold between the cw-modelocking regime and the Q-switching instabilities was studied in [117]. The threshold below which cw modelocking occurs was estimated as:

$$E_p^2 > E_{\text{sat},g} E_{\text{sat},a} \Delta R,$$

where E_p is the intracavity pulse energy, $E_{\text{sat},g}$ and $E_{\text{sat},a}$ are the gain and absorber saturation energies respectively, and ΔR the absorber modulation depth. This formula allows evaluating the modelocking regime with macroscopic parameters of the absorber.

3.2 Thin-disk modelocking for intracavity HHG

HHG requires a minimal laser intensity of a few 10^{13} W/cm² for XUV generation in xenon, the noble gas with the lowest ionization threshold. It implies that with a focal size ranging from 10 μ m to 15 μ m in radius, the laser should provide peak powers between 30 MW and 70 MW. If a tight focus of a few-micron radius can be achieved in external HHG systems without consequences on the oscillator stability, for intracavity HHG, the tight focus could be a rather constraining condition with possible consequences on the cavity stability. If HHG imposes two main constraints on the laser cavity, i.e., high peak powers and tight focus, another condition is required for HHG, which is the need to operate it under vacuum. As air strongly absorbs any radiation below 200 nm, the HHG interaction spot and the subsequent XUV propagation path need to be placed under vacuum (around 10^{-3} mbar). For an intracavity HHG experiment, it implies that the entire cavity needs to be evacuated. Thus, a first step was to achieve high intracavity peak power. Different cavities with different thin-disk materials were investigated. Then the cavity had to work under vacuum. Finally, once this cavity demonstrated stable operation under vacuum, a tight focus extension of two short focal curved mirror was added.

3.2.1 CALGO-based thin-disk laser

In the present sub-section, experiments achieved with Yb³⁺:CaAlGdO₄ (CALGO) in order to demonstrate the necessary intracavity peak power are presented. This work started in a collaboration with professor Ursula Keller's group at ETH Zürich to which I contributed on decreasing the pulse duration of an already existing laser cavity.

As previously described, the Yb-doped CALGO gain medium constitutes a good candidate to generate short pulses for HHG owing to its large and smooth gain bandwidth (over 35 nm for an inversion level of 10%). Combined with a good thermal conductivity, the material can be pumped at high power (up to 2 kW/cm²). However, it exhibits a low gain cross-section (compared to YAG for example, see Figure 3.3), which makes it operating preferably with low intracavity losses and therefore low cavity output coupling rates. For the given experiment aiming at a high intracavity peak power, it did not constitute a problem. Nevertheless, a high sensitivity to intracavity losses tends to make the cavity handling difficult. The results of such a system to which I contributed at ETH are presented here.

The laser described in this work is based on the cavity presented in [118]. About one year later (in 2014), the cavity was studied to decrease the pulse duration, leading to the results reported here.

At that time, CALGO-based bulk lasers already achieved sub-100-fs pulse duration with 12 W of average power [119] and 47 fs with 38 mW [120] in SESAM-modelocking, while the thin-disk geometry only demonstrated a SESAM-modelocked CALGO laser with 28 W in 300 fs or 1.3 W in 138 fs [110]. The laser reported by A. Diebold et al. demonstrated 5.1 W in 62 fs [118], the shortest pulse duration from a modelocked TDL (for any gain material) at that time. Starting from this laser, the pulse duration was reduced as described below.

The laser is based on a commercial Yb:CALGO disk (FEE GmbH) with a diameter of 6 mm, a thickness of 220 μm and a doping concentration of 3.1 at.%. The disk is made of a c-cut crystal orientation that allows exploiting the optical σ -polarization operation (broader gain cross-section, see Figure 3.3) and is wedged (wedge angle of $\sim 0.3^\circ$). The disk was soldered onto a copper-tungsten heat sink using indium at 180 $^\circ\text{C}$ and was placed in a commercial laser head (Dausinger & Giesen) with 24 passes of the pump beam onto the disk. The fiber-coupled pump laser diode delivers up to 400 W at 979.5 nm and is wavelength-stabilized by a volume Bragg grating. The pump spot was imaged into the disk with a diameter of 2.1 mm.

During the contacting process, the radius of curvature of the disk changed. In our case, before the contacting, the disk displayed a radius of curvature $R = -1.81$ m, and after the contacting, some deformation was observed resulting from a non-uniform pressure.

Initial tests for cw multi-transversal mode operation were performed using a simple V-cavity with a curved mirror (radius of curvature $R = -100$ mm), the thin disk and an output coupler (transmission rate $T = 0.9\%$). Up to 45 W of output power were obtained corresponding to an optical-to-optical efficiency of 45% and a slope efficiency of 54%. Due to impurities and scratches, the losses for a single pass through the disk was estimated to be $< 0.5\%$. For a comparison, YAG disks commonly feature losses of 0.1% in single pass.

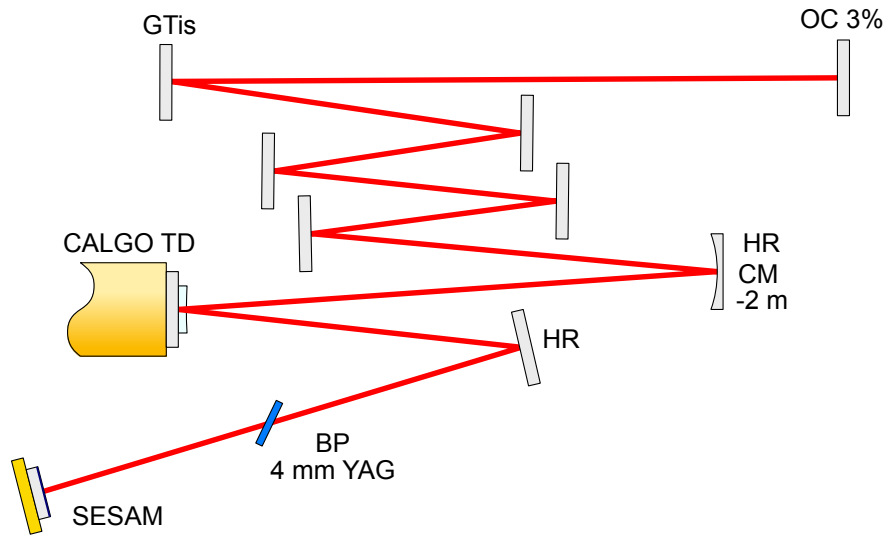


Figure 3.7: CALGO TDL oscillator scheme. OC stands for output coupler, HR for highly reflective mirrors, TD for thin disk and BP for Brewster plate.

The modelocking operation was achieved by first building a cw single-transversal mode cavity with dispersion management for soliton modelocking (depicted in Figure 3.7). An undoped-YAG plate was placed at Brewster's angle into the cavity so that the pulse experiences SPM and for the laser wavelength to select a linear polarization. The position of this plate in the cavity is critical as the beam size determines the amount of induced SPM. Gires-Tournois interferometer (GTI) mirrors were used in the cavity to compensate for dispersion and ensure soliton modelocking. In the optimal configuration, 600 mrad of nonlinear phase were induced by SPM, balanced by a total group delay dispersion of -300 fs^2 . With a 3% transmission output coupler, the laser achieved up to 14 W of average power in fundamental mode continuous-wave operation corresponding to an optical-to-optical efficiency of 19%. To avoid damage of the disk, the pump intensity was limited to 3 kW/cm^2 . The M^2 measurement confirmed a transverse single-mode operation with $M^2 < 1.1$. Passive modelocking was initiated and stabilized by a SESAM placed as a cavity end mirror where the beam radius is the smallest ($400 \mu\text{m}$) to maximize the fluence. The parameters of the SESAM measured at 20°C are a saturation fluence $F_{sat} = 10 \mu\text{J/cm}^2$, a modulation depth $\Delta R = 1.34\%$, non-saturable losses $\Delta R_{ns} = 0.5\%$ and an induced absorption coefficient $F_2 = 275 \text{ mJ/cm}^2$. Decreasing the output coupling rate to 2.5%, 5.1 W of average output power with 62 fs of stable pulse duration were obtained. With a total length of

2.34 m, the oscillator had a repetition rate of 64.8 MHz. The maximum pulse energy was estimated at 80 nJ and the intracavity peak power at 44 MW. The pulse spectrum measured with an optical spectrum analyzer had a FWHM of 23 nm, corresponding to a time-bandwidth product (TBP) of 0.38 (less than 20% above the ideal value). A fast photodiode and a sampling oscilloscope were used to check the single pulse operation.

The aforementioned results were obtained by Andreas Diebold and co-workers at ETH Zürich. In collaboration with the same group, I have been involved in the subsequent results reported below. In order to reduce the duration of the emitted pulses, different configurations were investigated. Different SESAMs, GTI mirrors (varying the total amount of GDD experienced by the pulse) and YAG plate thicknesses (to vary the amount of SPM) were tested. At the end, the configuration with the shortest pulses was close to the initial one. The output coupling rate was decreased down to 1.6%; the total amount of GDD was kept at -300 fs^2 , but the GTI mirrors were replaced with new ones with a flatter spectral dispersion (see Figure 3.8). In practice, a former GTI mirror with a GDD of -250 fs^2 was replaced with five new ones with a lower value of -55 fs^2 each.

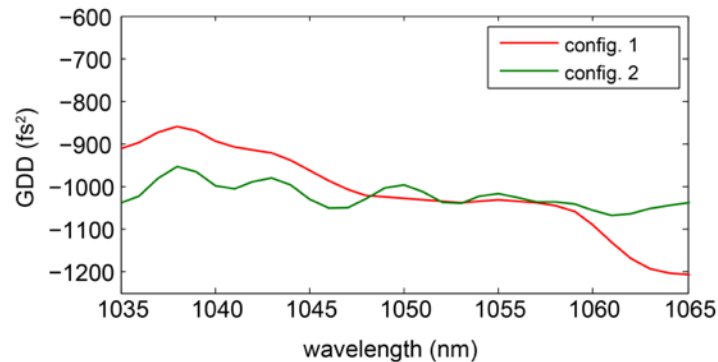


Figure 3.8: Total group delay dispersion spectra of GTI mirrors. Config 1 (red curve) corresponds to a -250 fs^2 coating and config 2 (green curve) corresponds to the sum of five -55 fs^2 coatings. Data provided by Layertec. Figure courtesy of Andreas Diebold (ETH).

In this configuration, a pulse duration of 49 fs was achieved with a spectral bandwidth of 25 nm (see Figure 3.9) and an average output power of 2 W. The time-bandwidth product indicates nearly transform-limited pulses ($\Delta\nu \cdot \tau_p = 0.33$). The M^2 measurement confirmed a transverse single mode operation ($M^2 < 1.05$). The corresponding intracavity peak power changed from 44 MW to 35 MW. When trying to push the laser to even shorter pulse durations by increasing the pump power (and thus increasing

the pulse energy as well as the nonlinear phase), the laser switched to double-pulsing operation.

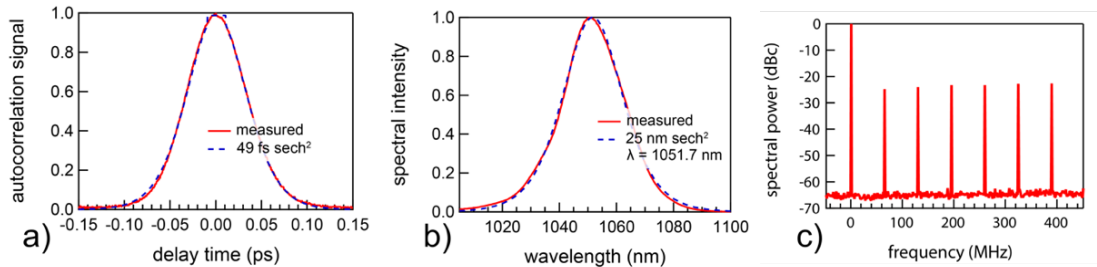


Figure 3.9: a) Autocorrelation trace of a 49-fs pulse with the sech² fit. b) Normalized optical spectrum of the pulse with a 25-nm FWHM sech² fit. c) Microwave spectrum of the pulse train at a resolution bandwidth of 3 MHz.

Transform-limited pulses with the shortest duration achieved from a SESAM-modelocked TDL were obtained (at that time), but the average output power and intracavity peak power were reduced compared to previous results, which is not beneficial for applications like HHG. The double-pulsing operation occurring at high pump power indicates the so-called SESAM roll-over (see Figure 3.10). As the pulse duration decreases and the pulse energy increases, the fluence on the SESAM increases and exceeds the roll-over point. Pulses of high energy thus experience more losses than pulses of lower energy and the fundamental high energy pulse splits into two pulses of lower energy (clearly visible in the experiment).

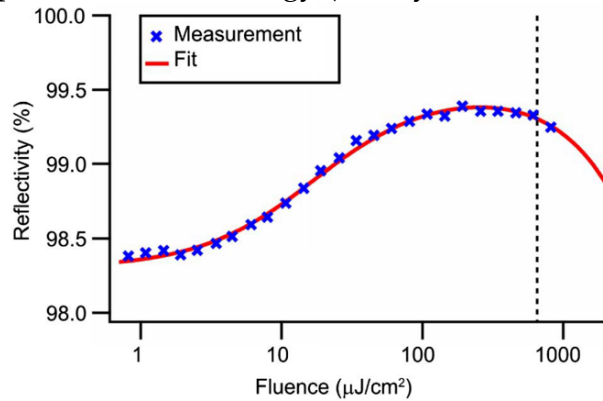


Figure 3.10: Nonlinear reflectivity of the SESAM used in the laser. The measurement was achieved with the reported CALGO laser operating with 85-fs pulses at a center wavelength of 1051 nm. The dash vertical line indicates the fluence occurring on the SESAM in the 62-fs pulse-duration operation of the laser (640 $\mu\text{J}/\text{cm}^2$). The roll-over of the SESAM is clearly visible at this position. Figure courtesy of Andreas Diebold (ETH).

3.2.2 LuO thin-disk modelocked oscillator in air

In comparison with CALGO, LuO displays a narrower emission bandwidth leading potentially to longer pulses. However, its very high thermal conductivity ($\kappa_{LuO} = 12$ (2 at.%) compared to $\kappa_{YAG} = 7.0$ (7 at.%) for YAG with typical doping concentration) combined with a high absorption cross-section as well as its large emission bandwidth (9 nm for YAG and 12 nm for LuO) make LuO the perfect candidate for high-power and short-pulses laser operation.

Since the first modelocking demonstration of a LuO laser in the thin-disk geometry in 2007 [107] with 25 W of output power and 523-fs pulse duration, the LuO material has demonstrated a long track record of high-power [121] and short pulse duration. Late to date is the demonstration, at the University of Neuchâtel, of Kerr-lens modelocking of a LuO thin-disk laser leading to 35 fs of pulse duration with 1.5 W of output power [108].

For the present experiment, changing to the LuO thin-disk led to an almost entirely new setup. With a different disk, set on a new cooling finger and mounted inside a new laser head, the cavity design had also to be changed. The Yb:Lu₂O₃ disk, grown and polished at IPL Hamburg, coated by Jenoptik and mounted on a cooling finger by Trumpf, is 0.1° wedged, 200- μ m thin with a diameter of 7 mm. For an optimal cooling capacity, a diamond heat sink was used. After contacting, the disk displayed a radius of curvature of -2.15 m and no excessive deformation was noticed. The thin-disk laser head, provided by Trumpf, allows the pump beam to pass 32 times onto the disk, creating a 2.4-mm diameter, flat-top shaped pump profile.

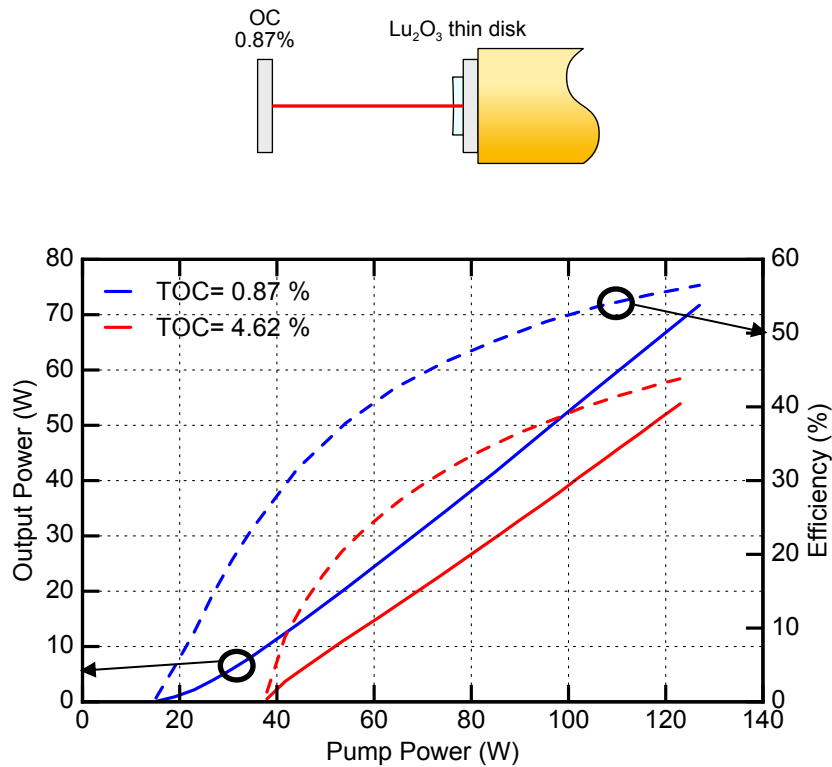


Figure 3.11: Top: cavity scheme for transverse multimode operation. The laser beam is depicted in red, OC: output coupler followed by its transmission rate. Bottom: Power slope of the LuO thin-disk in multimode operation with $T = 0.87\%$ and 4.62% transmission output coupling (TOC) rates. On the left scale, the output power is depicted in solid-line, on the right scale the corresponding efficiency is depicted in dotted-line.

To characterize the thin-disk, a linear cw multimode cavity was used (see Figure 3.11) with a 0.87% -transmission output coupler and the HR-backside of the thin-disk. Almost 80 W of output power was measured with an optical-to-optical efficiency of 57% , corresponding to a slope efficiency of 70% . In comparison, Peters et. al. [122] achieved up to 85% of slope efficiency using a $250\text{-}\mu\text{m}$ thick Yb:LuO doped at $2\text{ at.}\%$ with an output coupler transmission of 2.7% .

The cw single-mode cavity is depicted in Figure 3.12. Starting from the thin-disk, the cavity is divided into two arms. On one side, the beam divergence is handled by a combination of curved mirrors (CM) to be finally reflected on an highly reflective mirror (HR). In the other arm, the beam is simply reflected on HR mirrors before reaching the output coupler.

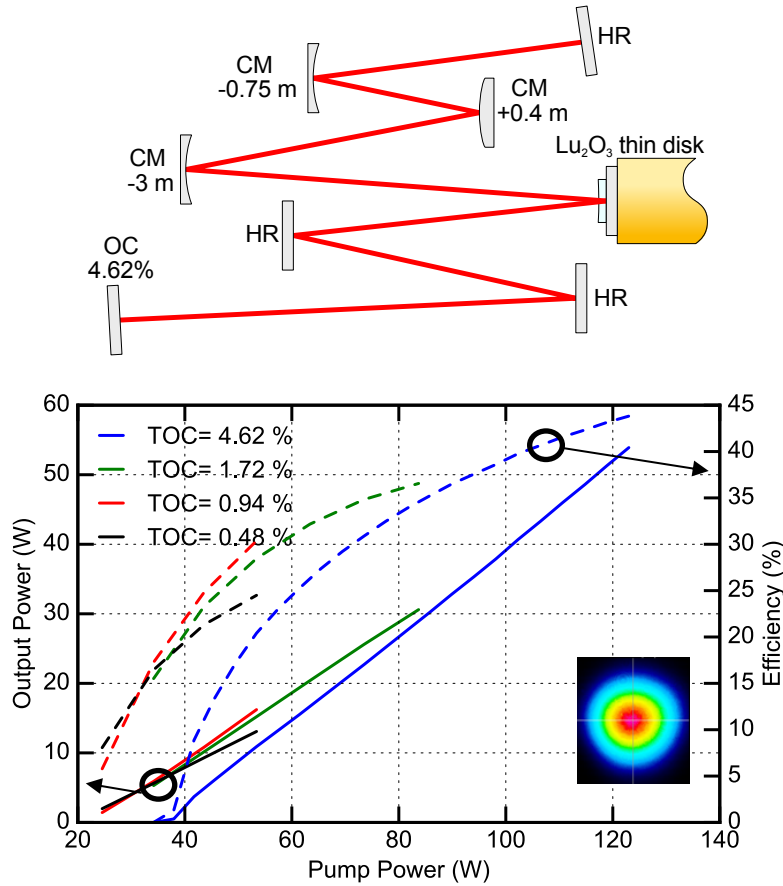


Figure 3.12: Top: laser cavity scheme for transverse single-mode operation. The laser beam path is depicted in red, HR stands for highly reflective mirror, CM: curved mirror followed by the radius of curvature. For this example, the output coupler transmission rate was 4.62%. Bottom: Transverse single-mode operation power slopes with various output coupler transmission rates. The solid-lines depict the output power (left vertical axis) and the dotted-lines the efficiency (right vertical axis). The beam profile displayed corresponds to the laser beam on the disk with 55 W of output power (TOC = 4.62%).

With an output coupling rate in transmission of 4.62%, the cavity demonstrated over 50 W of output power with a corresponding optical-to-optical efficiency of 44.5% and a slope efficiency of 63%. With other output couplers (see Figure 3.12), the power slope is lower and to avoid any damage on the disk, the power was kept at reasonable levels (below 5 kW/cm²) before the modelocking experiments.

For modelocking, the cavity was slightly changed (see Figure 3.13). The HR at the end of the curved-mirrors arm was replaced by a SESAM (saturation fluence $F_{\text{sat}} = 38.4 \mu\text{J}/\text{cm}^2$, modulation depth $\Delta R = 1.8\%$ and non-saturable losses $\Delta R_{\text{ns}} = 0.4\%$) and its position was arranged for an

optimized spot-size on the SESAM (1.4-mm radius). In the other arm, the last part is divided into two and the OC is used as a folding mirror (thus multiplying the output coupling rate of the cavity by a factor of two). A 4-mm thick undoped YAG plate is placed at Brewster angle at a beam of 760 μm in radius to ensure operation at linear p-polarization and to create a sufficient amount of SPM to compensate for negative dispersion for soliton modelocking. One plane HR mirror was added to the lower arm of the cavity (with no incidence on the beam propagation, see Figure 3.13) and three plane HR mirrors were replaced by -550 fs^2 GTI mirrors, accounting for a total negative group delay dispersion of -2750 fs^2 per roundtrip.

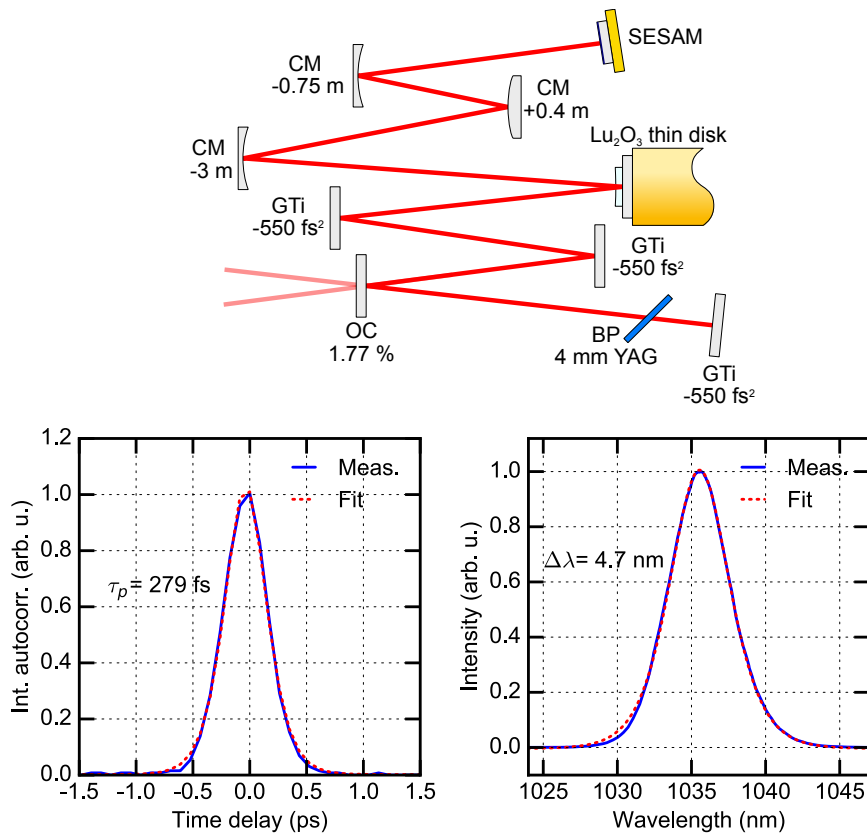


Figure 3.13: Top: laser cavity scheme for modelocking operation. CM: curved mirror followed by the radius of curvature, GTI: GTI mirrors followed by the GDD value, BP: Brewster plate 4-mm thick of undoped YAG. For this example, the output coupler transmission rate is 1.77% leading to an measured output coupling rate of 3.55% per round-trip. Bottom-left: autocorrelation trace of a 279-fs pulse emitted by the laser (solid blue line) with a sech² fit trace (dotted red line). Bottom-right: optical spectrum centered at 1035.7 nm (solid blue line) with 4.8 nm of FWHM with a sech² fit (dotted red line).

The cavity delivered pulses with a duration of 279 fs, a 4.8-nm large optical spectrum (see Figure 3.13) with a total output power of 15 W (7.5 W from each beam) for a pump power of 84 W. Increasing the pump power any further led to double-pulsing operation. The repetition rate of the laser was 44.88 MHz. The transverse mode was close to TEM₀₀ (measured $M^2 < 1.01$). The corresponding intracavity pulse energy was 8.8 μ J and the intracavity peak-power was 27.8 MW. The pulse seemed slightly chirped with a time-bandwidth product (TBP) equal to 0.375 (ideal TBP of 0.315 for a sech² pulse). Multiple output coupling rates were also tested for the optimum intracavity peak power while keeping the same SESAM (see Figure 3.14).

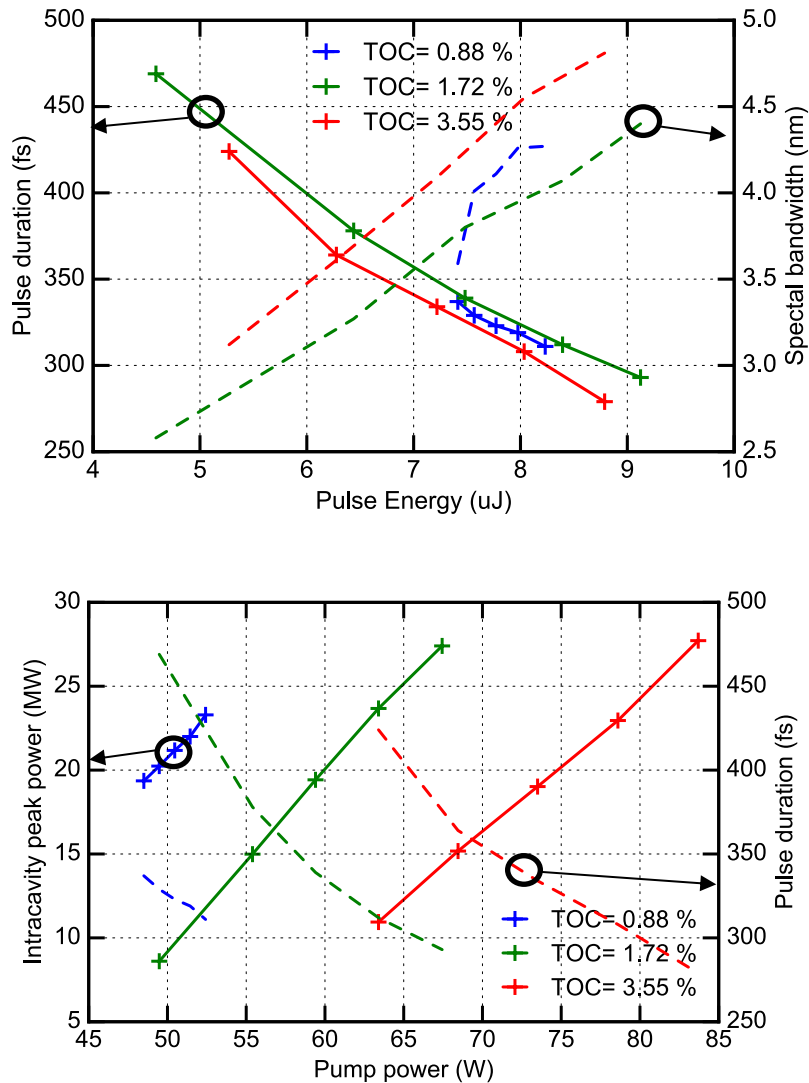


Figure 3.14: Top: pulse duration (left axis) and corresponding spectral bandwidth (right axis) versus pulse energy for different output coupler transmission (TOC) rates. The solid lines depict the pulse duration and the dotted lines the spectral bandwidth. Bottom: Intracavity peak power (left axis) and pulse duration (right axis) versus pump power. For the two graphics, the total transmission rates of 0.88%, 1.72% and 3.55% are respectively represented in blue, green and red.

Using an output coupler with a transmission rate of 0.86% (total transmission rate of 1.72%, in green in Figure 3.14), a pulse duration of 293 fs with an optical spectrum of 4.4 nm (FWHM) was measured with 67 W of pump power. The pulses are slightly closer to transform-limited

pulses as the corresponding TBP is 0.361. The corresponding intracavity peak power is 27.4 MW.

In summary, the developed oscillators demonstrated soliton modelocking operation with a TEM₀₀ transversal mode. However, the intracavity peak-power levels were not high enough to enable high-harmonic generation.

3.2.3 LuO thin-disk modelocked oscillator in vacuum

Following the previous cavity modelocking results, the cavity was placed inside a vacuum chamber. An extension was added in the output coupler arm to enhance the pulses energy, changing the repetition rate from 44.88 MHz to 17.9 MHz. A small additional extension, consisting of two short-radius curved mirrors, was set to create a tight focus for future HHG.

The cavity was mounted inside a compact vacuum chamber (see Figure 3.15) and all components were especially chosen to be compatible with vacuum operation: all mirror mounts were vacuum-compatible, the pipes for water-cooling of the thin-disk laser head and of the SESAM mount were also vacuum compatible. Each other metallic component (such as pillar posts or clamping forks) were cleaned in an ultra-sonic bath and then heated in an oven for outgassing before being placed inside the vacuum chamber.

The extension, depicted in Figure 3.16, consists of two curved mirrors (radius of curvature of -1.5 m and -3 m respectively) and allowed the beam to be expanded up to a diameter of 2.7 mm and to collimate it before encountering the end mirror (mounted on a flip-mount), extending the cavity length up to 8.38 m (see Figure 3.16). The tight-focus extension starts from the large collimated beam (when the HR mirror is flipped down), using a pair of curved mirrors (radius of curvature of -100 mm and -150 mm respectively). An estimated 12- μ m-radius tight focus is created between the two mirrors.

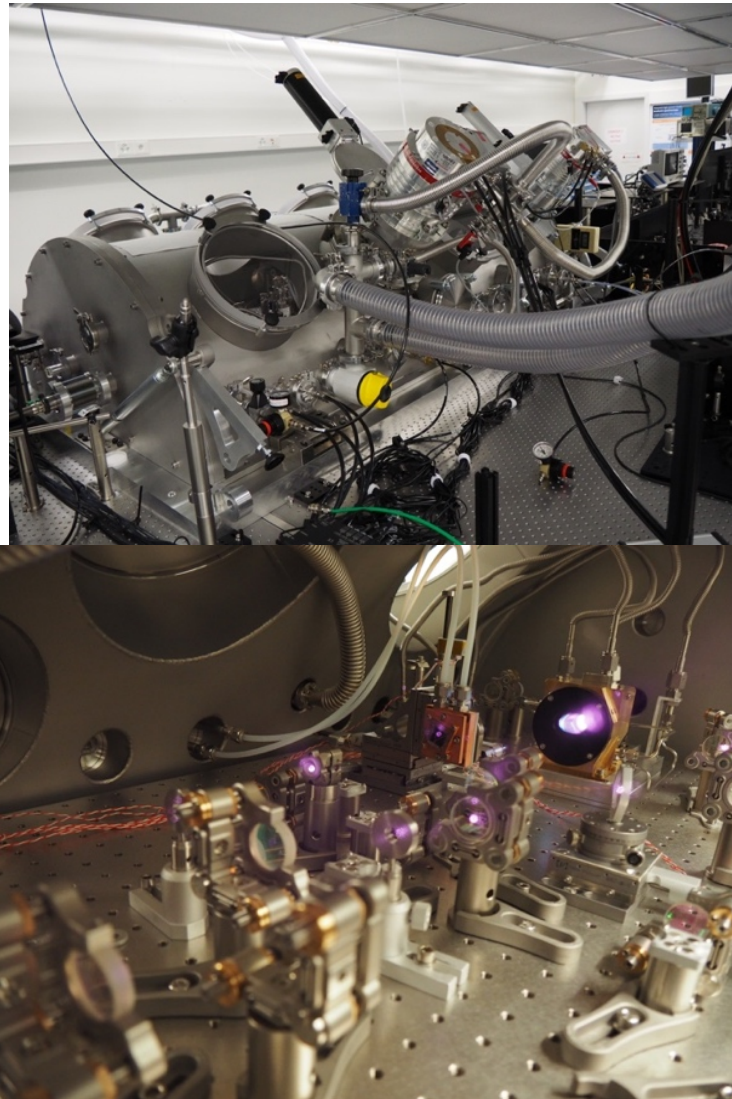


Figure 3.15: Top: picture of the vacuum chamber evacuated by two molecular turbo pumps, and two primary pumps. An optical breadboard of dimensions $150 \times 90 \text{ cm}^2$ is installed inside. Bottom: picture of the LuO thin-disk laser operating inside the vacuum chamber. The SESAM mount as well as the laser head are water-cooled with vacuum-proof pipes.

In cw operation, the laser emitted up to 17.4 W of average power without the tight focus (TF) extension when pumped by 66 W of power with a total output coupling rate of 1.4% in transmission, leading to an optical-to-optical efficiency of 26.4% (slope efficiency of 40%). With the TF extension, the same power level was obtained with good power stability.

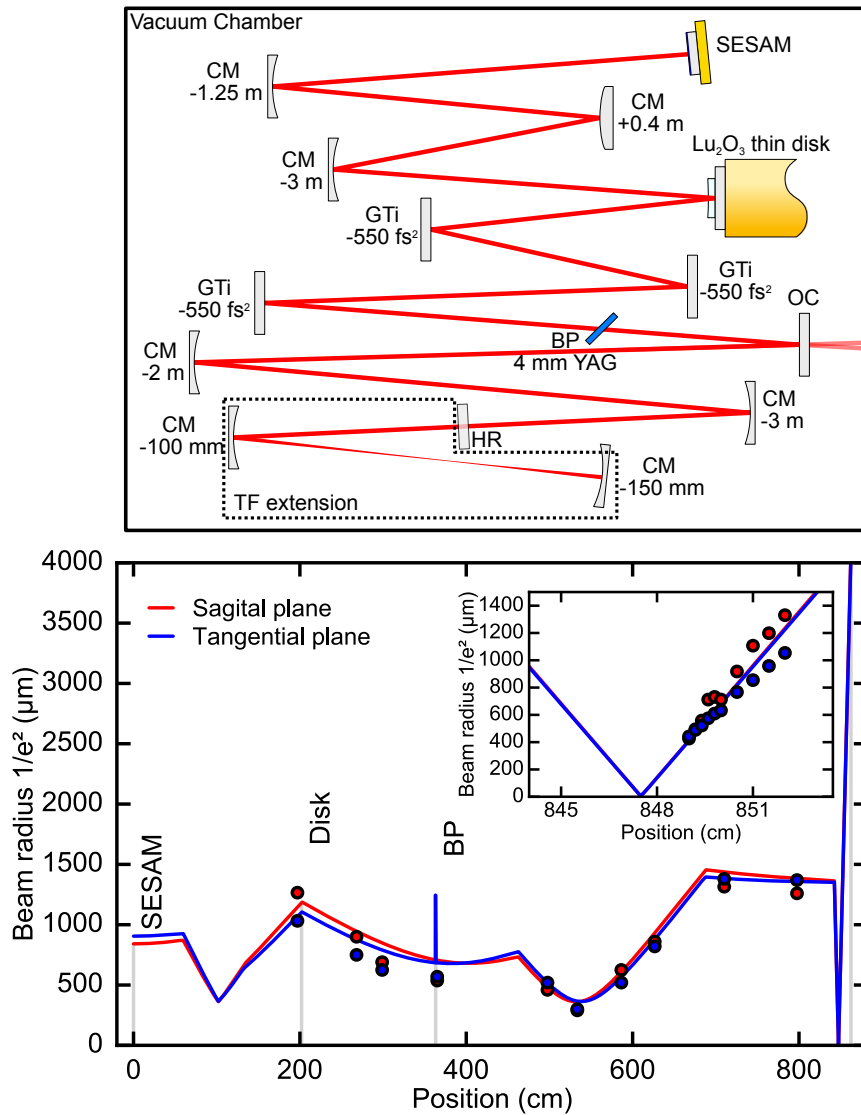


Figure 3.16: Top: Cavity scheme inside the vacuum chamber. The end mirror (HR) is placed on a flip mount, allowing a quick switch between two configurations: with or without the tight focus (TF) extension. Bottom: beam radius versus its position along the cavity for the sagittal and tangential planes. The simulated beam path is depicted by the solid lines while the experimental measurements are represented by the colored points. The vertical grey lines represent cavity elements such as the SESAM, the LuO thin-disk, the Brewster plate and the end cavity mirror.

For modelocking operation, the SESAM was changed for a saturation fluence of $47.5 \mu\text{J}/\text{cm}^2$, a modulation depth of 1.6% and non-saturable losses of 0.3%. Modelocking was achieved with different output couplers, each time re-adjusting the SESAM beam spot size. Operating the laser in vacuum required the amount of GDD and SPM to be adjusted to the vacuum level.

Using only the primary vacuum pumps, with a pressure of 10 mbar inside the chamber and an output coupling rate of 1.4% in transmission the modelocking performances presented in Figure 3.17 was obtained.

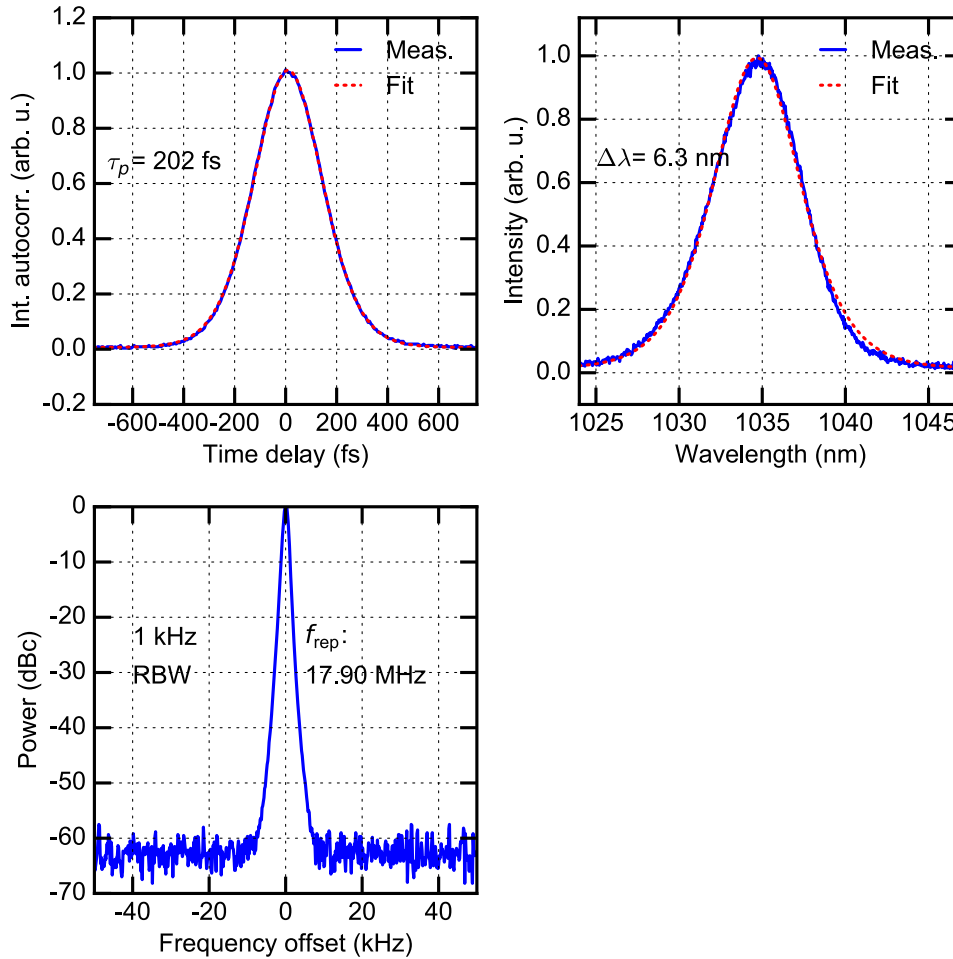


Figure 3.17: Top left: autocorrelation trace and sech² fit. Top right: optical spectrum centered at 1035 nm with sech² fit. Bottom: RF spectrum centered on the repetition rate of 17.9 MHz.

The laser delivered pulses with a duration of 202 fs and an optical spectrum with a width of 6.3 nm (FWHM) at a repetition rate of 17.90 MHz. The pulse time-bandwidth product was calculated as 0.361 and a beam quality of $M^2 < 1.02$ was measured. An output power of 6.7 W, corresponding to an intracavity pulse energy of 26.7 μJ and an intracavity peak power of 116.5 MW (see Figure 3.18) were obtained.

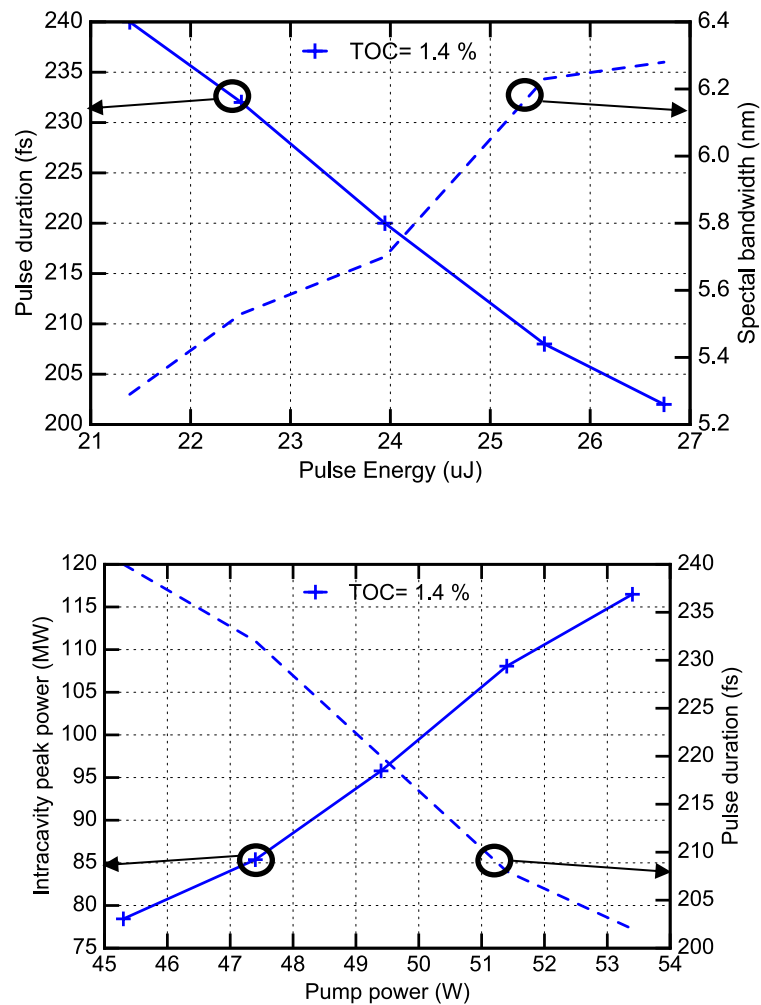


Figure 3.18: Top: pulse duration (solid line, left axis) and corresponding spectral bandwidth (dotted line, right axis) versus pulse energy. Bottom: Intracavity peak power (solid line, left axis) and pulse duration versus pump power (dotted line, right axis). Results obtained with an output coupler transmission (TOC) of 1.4%.

The laser demonstrated a prominent amount of intracavity peak power enabling HHG in xenon. However, the combination of such high-power operation with primary vacuum lead to a deterioration of the long-term power stability of the laser. To keep a good stability, the laser was not operated at full power, but was reduced to a level sufficient for HHG.

3.3 High harmonics generation

As previously discussed, the combination of two curved mirrors with a short focal length (ROC = -100 mm and -150 mm) led to a 12- μm radius tight focus. As HHG is very dependent on the light intensity, the determination of the beam radius at the focal point is crucial. A 250- μm thick wedged sapphire plate was placed before the focal point to reflect a small portion of the beam. The beam size was then measured along its propagation after the focal point. Considering the M^2 value previously measured, the beam-radius at focus was evaluated to be 12 μm . To separate the generated XUV light from the near-IR beam, the same 250- μm sapphire plate was placed at Brewster angle, for IR wavelength, 2 cm after the focal point. At the laser wavelength, the reflection was negligible whereas at $\lambda = 100 \text{ nm}$, $R = 7\%$ and at $\lambda = 60 \text{ nm}$, $R = 15\%$ allowing a minimal disturbance of the laser operation while enabling the extraction of the generated XUV light out of the laser resonator. This extraction methods is commonly used for enhancement cavities [90,91,123].

To deliver the gas close to the focal position, a 100- μm opening diameter quartz nozzle was used. Figure 3.19 depicts the computer-aided design (CAD) image of the nozzle and its mount with a gas dump underneath, together with a picture of the system under laser operation.

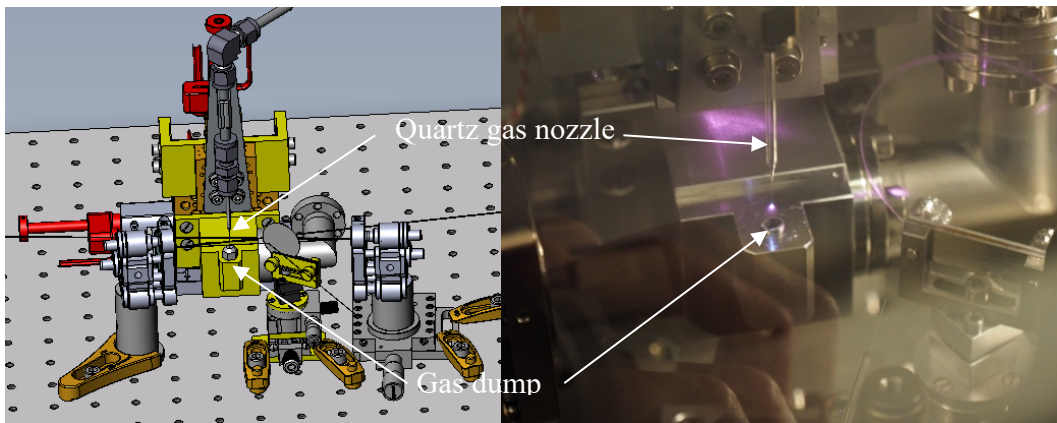


Figure 3.19: Left: CAD representation of the TF extension with the nozzle and gas dump mounted on a 3-D translation stage. Right: picture of the setup during laser operation with gas injection where the plasma created is clearly visible.

The nozzle and gas dump system were mounted on a X-Y-Z translation stage with vacuum compatible pico-motors. The gas dump, located below the nozzle was directly connected to a primary vacuum pump to efficiently extract the gas. With a few bars of gas pressure sent to

the nozzle, a few hundreds of mbar are estimated at the interaction volume position. Thanks to the gas dump, the chamber pressure was kept below 5×10^{-3} mbar, allowing a lossless propagation of the XUV beam inside. As the strength of the HHG signal is very dependent on the nozzle position, the vertical position of the system was roughly set under cw-operation of the laser and the horizontal position was then adjusted during the modelocked operation with HHG, maximizing directly the XUV signal. Figure 3.20 illustrates the modelocked-cavity including the TF extension with the nozzle and gas dump.

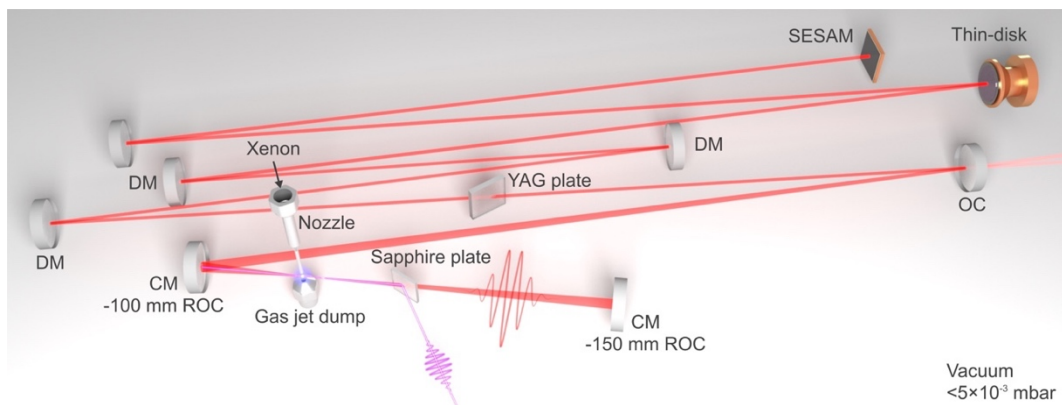


Figure 3.20: Illustration of the modelocked laser with the nozzle and gas dump for HHG (DM: dispersive mirrors, CM: curved mirror).

Without gas, the laser generated 264-fs pulses at a repetition rate of 17.35 MHz with an intracavity average power of 320 W at 49 W of pump power. The corresponding intracavity peak power was 62 MW dealing to a peak intensity of 2.7×10^{13} W/cm² at focus. Increasing the pump power further led to modelocking instabilities, proving that the laser operated close to the SESAM roll-over. Figure 3.21(a-d) depicts the autocorrelation trace, optical spectrum, RF spectrum and M^2 measurements of the modelocked laser without the gas jet.

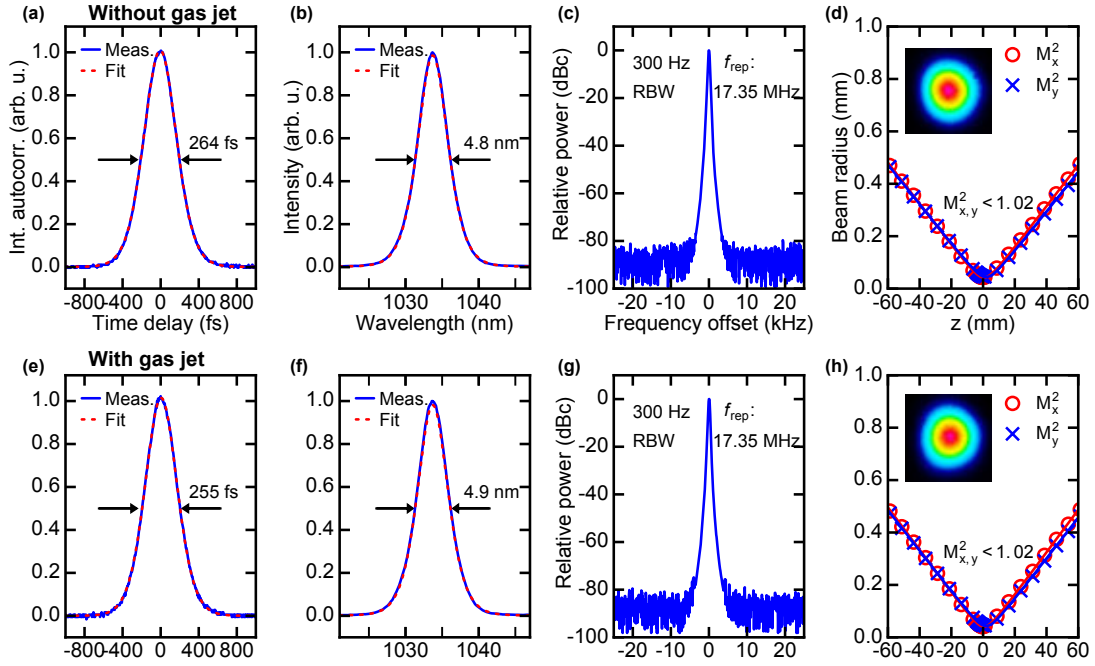


Figure 3.21: Comparison of the TDL oscillator performances without high-pressure gas jet (a-d) and with high-pressure gas jet (e-h). Autocorrelation trace with sech² fit (a,e), optical spectra with sech² fit (b,f), RF spectra centered on the repetition rate (c,g) and M^2 measurements as inset with output beam profile (d,h).

While injecting xenon at the laser focus, HHG was detected with a channel-electron multiplier (Photonis Magnum 5900). The XUV light was sent, by reflection on an unprotected gold mirror, to a wavelength-calibrated monochromator (Acton VM-502) equipped with a 1200-g/mm iridium-coated grating. The slit width allowed achieving a spectral resolution of 3.2 nm. The XUV spectra were acquired with and without a 0.2- μm thick aluminum filter to check the validity of the measurement, as the filter transmission significantly drops at wavelengths longer than 60 nm.

Using 3.4 bar of backing xenon pressure in the nozzle, the pressure at the interaction place is estimated to around 400 mbar. With gas injection, the laser average power was slightly reduced. By increasing the pump power from 49 W to 51 W, the same intracavity average power (320 W) was obtained as without gas jet. As illustrated in Figure 3.21 (e-h), the thin-disk oscillator achieved slightly shorter pulses of $\tau = 255$ fs. The corresponding intracavity peak power is 64 MW and the peak intensity in the focus is 2.8×10^{13} W/cm².

In this configuration, harmonics up to the 17th order (60.8 nm or 20.4 eV) were measured, in accordance to the cut-off formula [124]. The

detected spectrum is showed in Figure 3.22. Harmonics below the 11th order were not detected most likely due to the reabsorption in xenon for the 9th harmonic and to the low quantum efficiency of the detector in the spectral range corresponding to the 7th harmonic and below it.

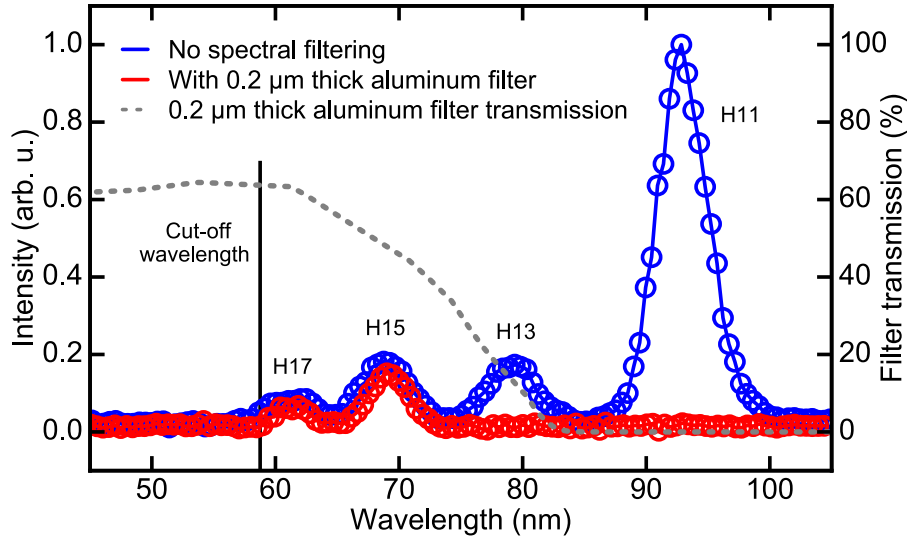


Figure 3.22: XUV light spectra measured without spectral filtering (in blue) and filtered (in red) by a 0.2- μm thick aluminum filter (transmission depicted in grey dotted-line).

Using the measured spectra and an additional measurement of the XUV flux with the channel-electron multiplier in all detected harmonics before the monochromator without aluminum filter, the average power and photon flux generated at the focus was estimated for the 11th harmonic with a similar method as described in [125]. A very conservative estimation results in a generated flux $\geq 2.6 \times 10^8$ photons/s corresponding to an average power ≥ 0.55 nW and a conversion efficiency $\geq 1.7 \times 10^{-12}$ with respect to the intracavity average power and $\geq 1.1 \times 10^{-11}$ with respect to the diode pump power.

To evaluate if the plasma generated during the HHG process induces any laser perturbation, the transverse beam quality and laser noise with and without HHG were evaluated. The laser operated in both cases in a fundamental transverse TEM_{00} mode with an M^2 value < 1.02 (Figure 3.21 (d, h)). The noise of the TDL oscillator output was measured in free-running operation on the passively filtered 4th harmonic of the repetition rate using a phase noise analyzer (Rohde & Schwarz FSWP-26). The measured power spectral density of the amplitude and phase noises of the 4h harmonic of the repetition rate is shown in Figure 3.23.

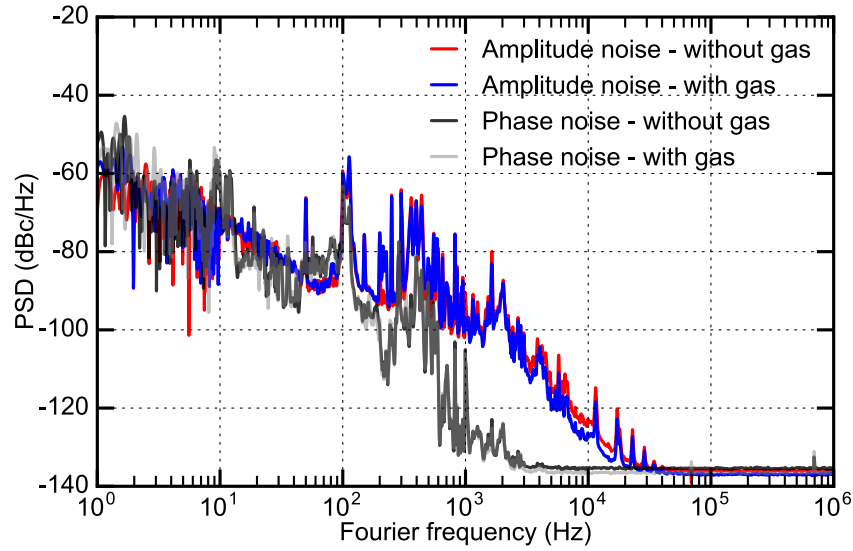


Figure 3.23: Amplitude and phase-noise measurements of the TDL oscillator output in free-running operation with and without gas.

Although the vacuum chamber was connected to two turbomolecular pumps and the opto-mechanical components were not optimized for high mechanical stability, an integrated relative intensity noise of only 0.78% and 0.76% was measured with and without gas, respectively over a large frequency range (1 Hz - 1 MHz). The laser noise is comparable to typical values of free-running ultrafast TDL oscillators [125,126].

Conclusion

In conclusion, the first intracavity HHG inside a modelocked TDL oscillator was demonstrated using an Yb:LuO modelocked TDL generating 255-fs short pulses at a repetition rate of 17.8 MHz with an intracavity average power of 320 W corresponding to an intracavity peak power of 64 MW in which a 12- μm radius tight focus was created. Harmonics up to the 17th order (60.8 nm or 20.4 eV) are detected with a XUV flux of 2.6×10^8 photons/s for the 11th harmonic, corresponding to an average power of 0.55 nW and a conversion efficiency of 1.7×10^{-12} with respect to the intracavity average power and 1.1×10^{-11} with respect to the diode pump power. In comparison with state-of-the-art MHz-repetition-rate HHG-based XUV sources [92,127–129], the conversion efficiency is rather poor as well as the generated flux. This experiment can be considered as a proof-of-principle experiment and should be compared to the first implementation of the other approaches where similar values were obtained.

Due to the early phase of this technology the following limitations need to be overcome in future experiments. In first place, the intracavity peak power reached in this experiment is only at the threshold of the needed power for HHG. Using different thin-disk materials or modelocking mechanisms, such as Kerr-lens modelocking, a higher intracavity average power or a shorter pulse duration could be achieved [85,86,96] thus increasing the intracavity peak power, the generated XUV photon flux should be higher. Secondly, the presented extraction method using a thin sapphire plate at Brewster angle has the advantage to be straightforward to implement. However, it reflects only around 7% of the XUV light, which drastically decreases the measured photon flux. HHG systems based on enhancement cavity share the same challenge. Among the solutions deployed for such systems, some can be adapted for the presented experiment. Instead of sapphire, magnesium oxide [130] can be implemented with up to 30% of reflectivity at around 50 nm. For a spectrally broader output coupling solution, a holey mirror can be used as an XUV output coupler relying on the very low divergence of the XUV light compared to the driving near-IR laser [127]. With a hole size of only 80 μm in radius e.g., the driving laser would experience small losses while around 20% of XUV light can be output-coupled at 60 nm (increasing to 100% at 10 nm). If such approach was successfully applied to enhanced-cavity-based HHG, no modelocked laser cavity has ever been reported with such a mirror. Other solutions are also possible such as an XUV grating etched on the top of an intracavity mirror [131], or non-collinear HHG [132] and

many others, but they have never been used for HHG inside a passive enhancement cavity.

Besides increasing the XUV photon flux, a possible next step for the experiment can be the CEO frequency locking of the thin-disk laser. Considering the recent performances of TDL laser in terms of stabilization of CEO frequency [99–101], and assuming HHG interaction with laser is weak enough, the locking of the presented cavity should be feasible. With the locking of the repetition rate, a fully stabilized laser would lead to a fully stabilized HHG as HHG is a coherent process, representing a stable XUV frequency comb with applications in many scientific fields.

Chapter 4

Conclusion and outlook

In the framework of this thesis two laser sources generating radiation in the mid-IR and in the XUV region were developed. The results from the 3- μm noise characterization allowed a better understanding of the different frequency noise sources present in typical DFG-based mid-IR sources as well as cavity-enhanced sources, with a system providing high 3- μm power levels. The HHG inside a modelocked TDL was demonstrated for the first time, at MHz repetition, adding another milestone on the path towards more compact XUV sources.

The first achievement of the thesis was the demonstration of high-power single frequency 3- μm radiation in cw (more than 120 mW) based on cavity-enhanced DFG using two high-power fiber amplifiers at 1.5 μm and 1 μm . The enhancement cavity allowed higher efficiencies by recycling the unconverted 1.5- μm light, allowing the enhancement of the 3- μm power by a factor of 10 compared to the single pass results. For frequency noise characterization, a single-pass second DFG-based 3- μm source powered by fiber amplifiers was built. A heterodyne beat note between the two 3- μm systems seeded by the same 1- μm and 1.5- μm laser diodes was measured and analyzed, characterizing the additive frequency noise of the cavity-enhanced 3- μm source. Comparing the additive 3- μm frequency noise with the independent frequency noise of the 1- μm and 1.5- μm laser diodes and fiber amplifiers shows that only the frequency noise of the laser diodes contributes to the linewidth of the mid-IR radiation, evaluated to amount to 1.1 MHz. Future steps of the experiment could be to change the end tips of the fiber amplifiers for a more stable system suppressing pointing instabilities. Also, a better thermal management of the DC-fibers for both 1- μm and 1.5- μm amplifiers using e.g. water-cooling systems would reduce the polarization instabilities. Finally, as only the frequency noise of the laser diodes is limiting the 3- μm linewidth, using stabilized 1- μm and 1.5- μm sources would reveal the great potential

of the presented experiment with an ultra-narrow linewidth and powerful mid-IR cw source. This experiment constitutes the first step toward potential cw-Watt level 3- μm source with ultra-narrow linewidth.

Following the rapid development of the TDLs, the first realization of HHG inside a modelocked TD oscillator was achieved using an Yb:LuO TDL achieving 255-fs short pulses with an intracavity average power of 320 W at a repetition rate of 17.8 MHz corresponding to an intracavity peak power of 64 MW in which a 12- μm radius tight focus is created. The detected harmonic spectrum displayed up to the 17th harmonic (60.8 nm or 20.4 eV). For the first detected harmonic (the 11th harmonic), a XUV flux of 2.6×10^8 photons/s was measured, corresponding to an average power of 0.55 nW and a conversion efficiency of 1.7×10^{-12} with respect to the intracavity average power and 1.1×10^{-11} with respect to the diode pump power. The noise evaluation of the system indicated no influence of the gas on the laser stability. For further improvements of the system, improving the laser performances in terms of pulse durations, with for example Kerr-lens modelocking, or average intracavity power would substantially lead to a large increase of the XUV photon flux. Stabilization of the CEO frequency as well as the repetition-rate would lead to a fully stabilized XUV optical frequency comb highly desirable for spectroscopy. Benefiting from the special geometry of TDL and from the inherent compact design from intracavity HHG, this experiment sets a first step towards compact and simple XUV sources at MHz repetition rates.

Bibliography

1. T. H. Maiman, "Stimulated Optical Radiation in Ruby," *Nature* **187**, 493–494 (1960).
2. R. Weiss, K. Thorne, and B. Barish, "Nobel prize in physics 2017, for decisive contributions to the LIGO detector and the observation of gravitational waves," (2017).
3. G. Di Domenico, S. Schilt, and P. Thomann, "Simple approach to the relation between laser frequency noise and laser line shape," *Appl. Opt.* **49**, 4801–4807 (2010).
4. U. Keller, G. W. 'tHooft, W. H. Knox, and J. E. Cunningham, "Femtosecond pulses from a continuously self-starting passively mode-locked Ti:sapphire laser," *Opt. Lett.* **16**, 1022 (1991).
5. P. B. Corkum, "Plasma perspective on strong field multiphoton ionization," *Phys. Rev. Lett.* **71**, 1994–1997 (1993).
6. K. Schafer, B. Yang, L. DiMauro, and K. Kulander, "Above threshold ionization beyond the high harmonic cutoff," *Phys. Rev. Lett.* **70**, 1599 (1993).
7. J. Higuët, "Etude structurelles et dynamiques de systèmes atomiques ou moléculaires par génération d'harmoniques d'ordre élevé," Université de Bordeaux (2010).
8. J. Itatani, J. Levesque, D. Zeidler, H. Niikura, H. Pépin, J. C. Kieffer, P. B. Corkum, and D. M. Villeneuve, "Tomographic imaging of molecular orbitals," *Nature* **432**, 867–871 (2004).
9. O. Smirnova, Y. Mairesse, S. Patchkovskii, N. Dudovich, D. Villeneuve, P. Corkum, and M. Yu. Ivanov, "High harmonic interferometry of multi-electron dynamics in molecules," *Nature* **460**, 972–977 (2009).
10. J. Levesque, Y. Mairesse, N. Dudovich, H. Pépin, J.-C. Kieffer, P. B. Corkum, and D. M. Villeneuve, "Polarization State of High-Order Harmonic Emission from Aligned Molecules," *Phys. Rev. Lett.* **99**, (2007).
11. J. Yu, N. P. Barnes, K. E. Murray, H. R. Lee, and Y. Bai, "Parametric generation of tunable infrared radiation for remote sensing applications," in U. N. Singh, T. Itabe, and Z. Liu, eds. (*Lidar Remote Sensing for Industry and Environment Monitoring III*, 2003), Vol. 4893, pp. 183–193.
12. K. Numata, H. Riris, S. Li, S. Wu, S. R. Kawa, M. Krainak, and J. Abshire, "Development of optical parametric amplifier for lidar measurements of trace gases on Earth and Mars," in U. N. Singh, ed. (*Lidar Remote Sensing for Environmental Monitoring XII*, 2011), Vol. 8159, p. 81590E.
13. C. Ghosh, S. Mandal, G. D. Banik, A. Maity, P. Mukhopadhyay, S. Ghosh, and M. Pradhan, "Targeting erythrocyte carbonic anhydrase and 18O-isotope of breath CO₂ for sorting out type 1 and type 2 diabetes," *Sci. Rep.* **6**, 35836 (2016).
14. E. Kerstel and L. Gianfrani, "Advances in laser-based isotope ratio measurements: selected applications," *Appl. Phys. B* **92**, 439–449 (2008).
15. E. R. Crosson, K. N. Ricci, B. A. Richman, F. C. Chilese, T. G. Owano, R. A. Provencal, M. W. Todd, J. Glasser, A. A. Kachanov, B. A. Paldus, T. G. Spence, and R. N. Zare, "Stable Isotope Ratios Using Cavity Ring-Down Spectroscopy: Determination of ¹³C/¹²C for Carbon Dioxide in Human Breath," *Anal. Chem.* **74**, 2003–2007 (2002).
16. A. Maity, M. Pal, S. Som, S. Maithani, S. Chaudhuri, and M. Pradhan, "Natural 18O and 13C-urea in gastric juice: a new route for non-invasive detection of ulcers," *Anal. Bioanal. Chem.* **409**, 193–200 (2017).
17. M. W. Todd, R. A. Provencal, T. G. Owano, B. A. Paldus, A. Kachanov, K. L. Vodopyanov, M. Hunter, S. L. Coy, J. I. Steinfeld, and J. T. Arnold, "Application of mid-infrared cavity-ringdown spectroscopy to trace explosives vapor detection using a broadly tunable (6–8 μm) optical parametric oscillator," *Appl. Phys. B Lasers Opt.* **75**, 367–376 (2002).
18. V. Z. Kolev, M. W. Duering, B. Luther-Davies, and A. V. Rode, "Compact high-power optical source for resonant infrared pulsed laser ablation and deposition of polymer materials," *Opt. Express* **14**, 12302–12309 (2006).
19. D. M. Bubbb, J. S. Horwitz, R. A. McGill, D. B. Chrisey, M. R. Papantonakis, R. F. Haglund, and B. Toftmann, "Resonant infrared pulsed-laser deposition of a sorbent chemoselective polymer," *Appl. Phys. Lett.* **79**, 2847–2849 (2001).
20. M. Duering, R. Haglund, and B. Luther-Davies, "Resonant infrared ablation of polystyrene with single picosecond pulses generated by an optical parametric amplifier," *Appl. Phys. A* **114**, 151–159 (2014).
21. G. Litfin, R. Beigang, and H. Welling, "Tunable cw laser operation in FB (II) type color center crystals," *Appl. Phys. Lett.* **31**, 381–382 (1977).
22. G. S. May and C. J. Spanos, *Fundamentals of Semiconductor Manufacturing and Process Control* (John Wiley & Sons, 2006).

Bibliography

23. J. Faist, F. Capasso, D. L. Sivco, C. Sirtori, A. L. Hutchinson, and A. Y. Cho, "Quantum Cascade Laser," *Science* **264**, 553–556 (1994).
24. J. M. Wolf, S. Riedi, M. J. Süess, M. Beck, and J. Faist, "3.36 μm single-mode quantum cascade laser with a dissipation below 250 mW," *Opt. Express* **24**, 662–671 (2016).
25. M. Kim, C. L. Canedy, W. W. Bewley, C. S. Kim, J. R. Lindle, J. Abell, I. Vurgaftman, and J. R. Meyer, "Interband cascade laser emitting at $\lambda=3.75\mu\text{m}$ in continuous wave above room temperature," *Appl. Phys. Lett.* **92**, 191110 (2008).
26. B. Argence, B. Chanteau, O. Lopez, D. Nicolodi, M. Abgrall, C. Chardonnet, C. Daussy, B. Darquié, Y. Le Coq, and A. Amy-Klein, "Quantum cascade laser frequency stabilization at the sub-Hz level," *Nat. Photonics* **9**, 456–460 (2015).
27. A. Ly, B. Szymanski, and F. Bretenaker, "Frequency stabilization of the non-resonant wave of a continuous-wave singly resonant optical parametric oscillator," *Appl. Phys. B* **120**, 201–205 (2015).
28. I. Ricciardi, S. Mosca, M. Parisi, P. Maddaloni, L. Santamaria, P. De Natale, and M. De Rosa, "Sub-kilohertz linewidth narrowing of a mid-infrared optical parametric oscillator idler frequency by direct cavity stabilization," *Opt. Lett.* **40**, 4743–4746 (2015).
29. H. Sera, M. Abe, K. Iwakuni, S. Okubo, H. Inaba, F.-L. Hong, and H. Sasada, "Sub-Doppler resolution mid-infrared spectroscopy using a difference-frequency-generation source spectrally narrowed by laser linewidth transfer," *Opt. Lett.* **40**, 5467–5470 (2015).
30. S. Okubo, H. Nakayama, K. Iwakuni, H. Inaba, and H. Sasada, "Absolute frequency list of the ν_3 -band transitions of methane at a relative uncertainty level of 10^{-11} ," *Opt. Express* **19**, 23878–23888 (2011).
31. S. Okubo, H. Nakayama, and H. Sasada, "Hyperfine-resolved 3.4- μm spectroscopy of CH_3I with a widely tunable difference frequency generation source and a cavity-enhanced cell: A case study of a local Coriolis interaction between the $\nu_1 = 1$ and $(\nu_2, \nu_6) = (1, 2^2)$ states," *Phys. Rev. A* **83**, 012505 (2011).
32. S. Chaitanya Kumar, R. Das, G. K. Samanta, and M. Ebrahim-Zadeh, "Optimally-output-coupled, 17.5 W, fiber-laser-pumped continuous-wave optical parametric oscillator," *Appl. Phys. B* **102**, 31–35 (2011).
33. S. Chaitanya Kumar, J. Wei, J. Debray, V. Kemlin, B. Boulanger, H. Ishizuki, T. Taira, and M. Ebrahim-Zadeh, "High-power, widely tunable, room-temperature picosecond optical parametric oscillator based on cylindrical 5%MgO:PPLN," *Opt. Lett.* **40**, 3897–3900 (2015).
34. S. Guha, J. O. Barnes, and L. P. Gonzalez, "Multiwatt-level continuous-wave midwave infrared generation using difference frequency mixing in periodically poled MgO-doped lithium niobate," *Opt. Lett.* **39**, 5018–5021 (2014).
35. L. Tombez, S. Schilt, J. Francesco, T. Führer, B. Rein, T. Walther, G. Domenico, D. Hofstetter, and P. Thomann, "Linewidth of a quantum-cascade laser assessed from its frequency noise spectrum and impact of the current driver," *Appl. Phys. B* **109**, 407–414 (2012).
36. I. Sergachev, R. Maulini, T. Gresch, S. Blaser, A. Bismuto, A. Müller, Y. Bidaux, T. Südmeyer, and S. Schilt, "Frequency stability of a dual wavelength quantum cascade laser," *Opt. Express* **25**, 11027–11037 (2017).
37. B. J. Ainslie, "A review of the fabrication and properties of erbium-doped fibers for optical amplifiers," *J. Light. Technol.* **9**, 220–227 (1991).
38. R. Paschotta, "Gain and absorption (negative gain) of erbium," https://www.rp-photonics.com/erbium_doped_fiber_amplifiers.html.
39. Y. Jeong, J. Nilsson, J. K. Sahu, D. N. Payne, R. Horley, L. M. B. Hickey, and P. W. Turner, "Power Scaling of Single-Frequency Ytterbium-Doped Fiber Master-Oscillator Power-Amplifier Sources up to 500 W," *IEEE J. Sel. Top. Quantum Electron.* **13**, 546–551 (2007).
40. R. Paschotta, "Ytterbium doped gain media," https://www.rp-photonics.com/ytterbium_doped_gain_media.html.
41. C. Shi, H. Zhang, X. Wang, P. Zhou, and X. Xu, "kW-class high power fiber laser enabled by active long tapered fiber," *High Power Laser Sci. Eng.* **6**, (2018).
42. A. Kobayakov, M. Sauer, and D. Chowdhury, "Stimulated Brillouin scattering in optical fibers," *Adv. Opt. Photonics* **2**, 1 (2010).
43. M.-A. Lapointe, S. Chatigny, M. Piché, M. Cain-Skaff, and J.-N. Maran, "Thermal effects in high-power CW fiber lasers," in D. V. Gapontsev, D. A. Kliner, J. W. Dawson, and K. Tankala, eds. (*Fiber Lasers VI: Technology, Systems, and Applications*, 2009), Vol. 7195, p. 71951U.
44. T. Schreiber, F. Röser, O. Schmidt, J. Limpert, R. Iliew, F. Lederer, A. Petersson, C. Jacobsen, K. P. Hansen, J. Broeng, and A. Tünnermann, "Stress-induced single-polarization single-transverse mode photonic crystal fiber with low nonlinearity," *Opt. Express* **13**, 7621–7630 (2005).
45. J. A. Armstrong, N. Bloembergen, J. Ducuing, and P. S. Pershan, "Interaction between light waves in nonlinear dielectric," *Phys Rev* **127**, 1918–1939 (1962).
46. D. A. K. G. D. Boyd, "Parametric Interaction of Focused Gaussian Light Beams," *J. Appl. Phys.* **39**, 3597–3642 (1968).
47. D. Richter and P. Weibring, "Ultra-high precision mid-IR spectrometer I: Design and analysis of an optical fiber pumped difference-frequency generation source," *Appl. Phys. B* **82**, 479–486 (2006).
48. Tran-Ba-Chu and M. Broyer, "Intracavity single resonance optical parametric oscillator (I.S.R.O.)," *J. Phys.* **45**,

- 1599–1606 (1984).
49. D. H. Jundt, "Temperature-dependent Sellmeier equation for the index of refraction, n_e , in congruent lithium niobate," *Opt. Lett.* **22**, 1553–1555 (1997).
 50. O. Paul, A. Quosig, T. Bauer, M. Nittmann, J. Bartschke, G. Anstett, and J. A. L'huillier, "Temperature-dependent Sellmeier equation in the MIR for the extraordinary refractive index of 5% MgO doped congruent LiNbO₃," *Appl. Phys. B* **86**, 111–115 (2006).
 51. L. S. Cruz and F. C. Cruz, "External power-enhancement cavity versus intracavity frequency doubling of Ti:sapphire lasers using BIBO," *Opt. Express* **15**, 11913–11921 (2007).
 52. U. Simon, S. Waltman, I. Loa, F. K. Tittel, and L. Hollberg, "External-cavity difference-frequency source near 3.2 μm , based on combining a tunable diode laser with a diode-pumped Nd:YAG laser in AgGaS₂," *JOSA B* **12**, 323–327 (1995).
 53. M. F. Witinski, J. B. Paul, and J. G. Anderson, "Pump-enhanced difference-frequency generation at 3.3 μm ," *Appl. Opt.* **48**, 2600–2606 (2009).
 54. E. D. Black, "An introduction to Pound–Drever–Hall laser frequency stabilization," *Am. J. Phys.* **69**, 79–87 (2001).
 55. C.-C. Liao, Y.-H. Lien, K.-Y. Wu, Y.-R. Lin, and J.-T. Shy, "Widely tunable difference frequency generation source for high-precision mid-infrared spectroscopy," *Opt. Express* **21**, 9238–9246 (2013).
 56. J. Miao, T. Ishikawa, B. Johnson, E. H. Anderson, B. Lai, and K. O. Hodgson, "High Resolution 3D X-Ray Diffraction Microscopy," *Phys. Rev. Lett.* **89**, 088303 (2002).
 57. B. J. Hillier, K. S. Christopherson, K. E. Prehoda, D. S. Bredt, and W. A. Lim, "Unexpected Modes of PDZ Domain Scaffolding Revealed by Structure of nNOS-Syntrophin Complex," *Science* **284**, 812–815 (1999).
 58. H. Luecke, "Structural Changes in Bacteriorhodopsin During Ion Transport at 2 Angstrom Resolution," *Science* **286**, 255–260 (1999).
 59. R. Neutze, R. Wouts, D. van der Spoel, E. Weckert, and J. Hajdu, "Potential for biomolecular imaging with femtosecond X-ray pulses," *Nature* **406**, 752–757 (2000).
 60. A. Föhlisch, P. Feulner, F. Hennies, A. Fink, D. Menzel, D. Sanchez-Portal, P. M. Echenique, and W. Wurth, "Direct observation of electron dynamics in the attosecond domain," *Nature* **436**, 373–376 (2005).
 61. L. Young, E. P. Kanter, B. Krässig, Y. Li, A. M. March, S. T. Pratt, R. Santra, S. H. Southworth, N. Rohringer, L. F. DiMauro, G. Doumy, C. A. Roedig, N. Berrah, L. Fang, M. Hoener, P. H. Bucksbaum, J. P. Cryan, S. Ghimire, J. M. Glowina, D. A. Reis, J. D. Bozek, C. Bostedt, and M. Messerschmidt, "Femtosecond electronic response of atoms to ultra-intense X-rays," *Nature* **466**, 56–61 (2010).
 62. T. Popmintchev, M.-C. Chen, D. Popmintchev, P. Arpin, S. Brown, S. Alisauskas, G. Andriukaitis, T. Balciunas, O. D. Mücke, A. Pugzlys, A. Baltuska, B. Shim, S. E. Schrauth, A. Gaeta, C. Hernandez-Garcia, L. Plaja, A. Becker, A. Jaron-Becker, M. M. Murnane, and H. C. Kapteyn, "Bright Coherent Ultrahigh Harmonics in the keV X-ray Regime from Mid-Infrared Femtosecond Lasers," *Science* **336**, 1287–1291 (2012).
 63. A. McPherson, G. Gibson, H. Jara, U. Johann, T. S. Luk, I. A. McIntyre, K. Boyer, and C. K. Rhodes, "Studies of multiphoton production of vacuum-ultraviolet radiation in the rare gases," *J. Opt. Soc. Am B* **4**, 595–601 (1987).
 64. M. Ferray, A. L'Huillier, X. F. Li, L. A. Lompré, G. Mainfray, and C. Manus, "Multiple-harmonic conversion of 1064 nm radiation in rare gases," *J. Phys. B At. Mol. Opt. Phys.* **21**, L31–L35 (1988).
 65. G. Vampa, C. R. McDonald, G. Orlando, D. D. Klug, P. B. Corkum, and T. Brabec, "Theoretical Analysis of High-Harmonic Generation in Solids," *Phys. Rev. Lett.* **113**, 073901 (2014).
 66. O. Razskazovskaya, T. T. Luu, M. Trubetskov, E. Goulielmakis, and V. Pervak, "Nonlinear absorbance in dielectric multilayers," *Optica* **2**, 803 (2015).
 67. T. T. Luu, Z. Yin, A. Jain, T. Gaumnitz, Y. Pertot, J. Ma, and H. J. Wörner, "Extreme-ultraviolet high-harmonic generation in liquids," *Nat. Commun.* **9**, 3723 (2018).
 68. P. M. Paul, E. S. Toma, P. Breger, G. Mullot, F. Augé, Ph. Balcou, H. G. Muller, and P. Agostini, "Observation of a Train of Attosecond Pulses from High Harmonic Generation," *Science* **292**, 1689–1692 (2001).
 69. M. Hentschel, R. Kienberger, Ch. Spielmann, G. A. Reider, N. Milosevic, T. Brabec, P. Corkum, U. Heinzmann, M. Drescher, and F. Krausz, "Attosecond metrology," *Nature* **414**, 509–513 (2001).
 70. Y. Mairesse, A. de Bohan, L. J. Frasinski, H. Merdji, L. C. Dinu, P. Monchicourt, P. Breger, M. Kovačev, R. Taïeb, B. Carré, H. G. Muller, P. Agostini, and P. Salières, "Attosecond Synchronization of High-Harmonic Soft X-rays," *Science* **302**, 1540–1543 (2003).
 71. S. Backus, C. G. Durfee, M. M. Murnane, and H. C. Kapteyn, "High power ultrafast lasers," *Rev. Sci. Instrum.* **69**, 1207–1223 (1998).
 72. R. Dörner, V. Mergel, O. Jagutzki, L. Spielberger, J. Ullrich, R. Moshhammer, and H. Schmidt-Böcking, "Cold Target Recoil Ion Momentum Spectroscopy: a 'momentum microscope' to view atomic collision dynamics," *Phys. Rep.* **330**, 95–192 (2000).
 73. M. Sabbar, S. Heuser, R. Boge, M. Lucchini, L. Gallmann, C. Cirelli, and U. Keller, "Combining attosecond XUV pulses with coincidence spectroscopy," *Rev. Sci. Instrum.* **85**, 103113 (2014).
 74. M. I. Stockman, M. F. Kling, U. Kleineberg, and F. Krausz, "Attosecond nanoplasmonic-field microscope," *Nat. Photonics* **1**, 539–544 (2007).

Bibliography

75. R. Klas, S. Demmler, M. Tschernajew, S. Hädrich, Y. Shamir, A. Tünnermann, J. Rothhardt, and J. Limpert, "Table-top milliwatt-class extreme ultraviolet high harmonic light source," *Optica* **3**, 1167–1170 (2016).
76. M. D. Seaberg, D. E. Adams, E. L. Townsend, D. A. Raymondson, W. F. Schlotter, Y. Liu, C. S. Menoni, L. Rong, C.-C. Chen, J. Miao, and others, "Ultrahigh 22 nm resolution coherent diffractive imaging using a desktop 13 nm high harmonic source," *Opt. Express* **19**, 22470–22479 (2011).
77. G. K. Tadesse, R. Klas, S. Demmler, S. Hädrich, I. Wahyutama, M. Steinert, C. Spielmann, M. Zürch, T. Pertsch, A. Tünnermann, J. Limpert, and J. Rothhardt, "High speed and high resolution table-top nanoscale imaging," *Opt. Lett.* **41**, 5170–5173 (2016).
78. D. Z. Kandula, C. Gohle, T. J. Pinkert, W. Ubachs, and K. S. E. Eikema, "Extreme Ultraviolet Frequency Comb Metrology," *Phys. Rev. Lett.* **105**, 063001 (2010).
79. A. Cingöz, D. C. Yost, T. K. Allison, A. Ruehl, M. E. Fermann, I. Hartl, and J. Ye, "Direct frequency comb spectroscopy in the extreme ultraviolet," *Nature* **482**, 68–71 (2012).
80. P. Russbuehdt, T. Mans, J. Weitenberg, H. D. Hoffmann, and R. Poprawe, "Compact diode-pumped 1.1 kW Yb:YAG Innoslab femtosecond amplifier," *Opt. Lett.* **35**, 4169–4171 (2010).
81. A. Klenke, S. Breilkopf, M. Kienel, T. Gottschall, T. Eidam, S. Hädrich, J. Rothhardt, J. Limpert, and A. Tünnermann, "530 W, 13 mJ, four-channel coherently combined femtosecond fiber chirped-pulse amplification system," *Opt. Lett.* **38**, 2283–2285 (2013).
82. M. Müller, M. Kienel, A. Klenke, T. Gottschall, E. Shestaev, M. Plötner, J. Limpert, and A. Tünnermann, "1 kW 1 mJ eight-channel ultrafast fiber laser," *Opt. Lett.* **41**, 3439–3442 (2016).
83. J. A. der Au, G. J. Spühler, T. Südmeyer, R. Paschotta, R. Hövel, M. Moser, S. Erhard, M. Karszewski, A. Giesen, and U. Keller, "16.2-W average power from a diode-pumped femtosecond Yb:YAG thin disk laser," *Opt. Lett.* **25**, 859–861 (2000).
84. C. J. Saraceno, F. Emaury, O. H. Heckl, C. R. E. Baer, M. Hoffmann, C. Schriber, M. Golling, T. Südmeyer, and U. Keller, "275 W average output power from a femtosecond thin disk oscillator operated in a vacuum environment," *Opt. Express* **20**, 23535–23541 (2012).
85. C. J. Saraceno, F. Emaury, C. Schriber, M. Hoffmann, M. Golling, T. Südmeyer, and U. Keller, "Ultrafast thin-disk laser with 80 μ J pulse energy and 242 W of average power," *Opt. Lett.* **39**, 9–12 (2014).
86. J. Brons, V. Pervak, D. Bauer, D. Sutter, O. Pronin, and F. Krausz, "Powerful 100-fs-scale Kerr-lens mode-locked thin-disk oscillator," *Opt. Lett.* **41**, 3567–3570 (2016).
87. M. Nisoli, S. De Silvestri, and O. Svelto, "Generation of high energy 10 fs pulses by a new pulse compression technique," *Appl. Phys. Lett.* **68**, 2793–2795 (1996).
88. F. Emaury, C. J. Saraceno, B. Debord, D. Ghosh, A. Diebold, F. Gèrôme, T. Südmeyer, F. Benabid, and U. Keller, "Efficient spectral broadening in the 100-W average power regime using gas-filled kagome HC-PCF and pulse compression," *Opt. Lett.* **39**, 6843–6846 (2014).
89. R. J. Jones and J. Ye, "Femtosecond pulse amplification by coherent addition in a passive optical cavity," *Opt. Lett.* **27**, 1848–1850 (2002).
90. R. J. Jones, K. D. Moll, M. J. Thorpe, and J. Ye, "Phase-Coherent Frequency Combs in the Vacuum Ultraviolet via High-Harmonic Generation inside a Femtosecond Enhancement Cavity," *Phys. Rev. Lett.* **94**, 193201 (2005).
91. C. Gohle, T. Udem, M. Herrmann, J. Rauschenberger, R. Holzwarth, H. A. Schuessler, F. Krausz, and T. W. Hänsch, "A frequency comb in the extreme ultraviolet," *Nature* **436**, 234–237 (2005).
92. H. Carstens, M. Högner, T. Saule, S. Holzberger, N. Lilienfein, A. Guggenmos, C. Jocher, T. Eidam, D. Esser, V. Tosa, V. Pervak, J. Limpert, A. Tünnermann, U. Kleineberg, F. Krausz, and I. Pupeza, "High-harmonic generation at 250 MHz with photon energies exceeding 100 eV," *Optica* **3**, 366–369 (2016).
93. E. Seres, J. Seres, and C. Spielmann, "Extreme ultraviolet light source based on intracavity high harmonic generation in a mode locked Ti:sapphire oscillator with 9.4 MHz repetition rate," *Opt. Express* **20**, 6185–6190 (2012).
94. A. Giesen, H. Hügel, A. Voss, K. Wittig, U. Brauch, and H. Opower, "Scalable concept for diode-pumped high-power solid-state lasers," *Appl. Phys. B Lasers Opt.* **58**, 365–372 (1994).
95. J. Brons, V. Pervak, E. Fedulova, D. Bauer, D. Sutter, V. Kalashnikov, A. Apolonskiy, O. Pronin, and F. Krausz, "Energy scaling of Kerr-lens mode-locked thin-disk oscillators," *Opt. Lett.* **39**, 6442–6445 (2014).
96. N. Kanda, A. A. Eilanlou, T. Imahoko, T. Sumiyoshi, Y. Nabekawa, M. Kuwata-Gonokami, and K. Midorikawa, "High-Pulse-Energy Yb: YAG Thin Disk Mode-Locked Oscillator for Intra-Cavity High Harmonic Generation," in *Advanced Solid State Lasers Congress (2013)* (Optical Society of America, 2013), pp. AF3A–8.
97. C. Paradis, N. Modsching, V. J. Wittwer, B. Deppe, C. Kränkel, and T. Südmeyer, "Generation of 35-fs pulses from a Kerr lens mode-locked Yb:Lu₂O₃ thin-disk laser," *Opt. Express* **25**, 14918–14925 (2017).
98. N. Modsching, C. Paradis, F. Labaye, M. Gaponenko, I. J. Graumann, A. Diebold, F. Emaury, V. J. Wittwer, and T. Südmeyer, "Kerr lens mode-locked Yb:CALGO thin-disk laser," *Opt. Lett.* **43**, 879–882 (2018).
99. A. Klenner, F. Emaury, C. Schriber, A. Diebold, C. J. Saraceno, S. Schilt, U. Keller, and T. Südmeyer, "Phase-stabilization of the carrier-envelope-offset frequency of a SESAM modelocked thin disk laser," *Opt. Express* **21**, 24770–24780 (2013).
100. O. Pronin, M. Seidel, J. Brons, F. Lücking, V. Pervak, A. Apolonski, T. Udem, and F. Krausz, "Carrier-envelope

- phase stabilized thin-disk oscillator," in *Advanced Solid-State Lasers Congress (2013)* (Optical Society of America, 2013), p. AF3A.5.
101. M. Seidel, J. Brons, F. Lücking, V. Pervak, A. Apolonski, T. Udem, and O. Pronin, "Carrier-envelope-phase stabilization via dual wavelength pumping," *Opt. Lett.* **41**, 1853–1856 (2016).
 102. N. Jornod, K. Gürel, V. J. Wittwer, P. Brochard, S. Hakobyan, S. Schilt, D. Waldburger, U. Keller, and T. Südmeyer, "Carrier-envelope offset frequency stabilization of a gigahertz semiconductor disk laser," *Optica* **4**, 1482–1487 (2017).
 103. R. Ell, U. Morgner, F. X. Kärtner, J. G. Fujimoto, E. P. Ippen, V. Scheuer, G. Angelow, T. Tschudi, M. J. Lederer, A. Boiko, and B. Luther-Davies, "Generation of 5-fs pulses and octave-spanning spectra directly from a Ti:sapphire laser," *Opt. Lett.* **26**, 373–375 (2001).
 104. D. E. Spence, P. N. Kean, and W. Sibbett, "60-fsec pulse generation from a self-mode-locked Ti:sapphire laser," *Opt. Lett.* **16**, 42–44 (1991).
 105. J. Zhang, J. Brons, M. Seidel, V. Pervak, V. Kalashnikov, Z. Wei, A. Apolonski, F. Krausz, and O. Pronin, "49-fs Yb:YAG thin-disk oscillator with distributed Kerr-lens mode-locking," in *European Quantum Electronics Conference* (Optical Society of America, 2015), p. PD_A_1.
 106. J. Brons, O. Pronin, M. Seidel, V. Pervak, D. Bauer, D. Sutter, V. L. Kalashnikov, A. Apolonski, and F. Krausz, "120 W, 4 μ J from a purely Kerr-lens mode-locked Yb:YAG thin-disk oscillator," in *Advanced Solid-State Lasers Congress (2013)* (Optical Society of America, 2013), p. AF3A.4.
 107. S. V. Marchese, C. R. E. Baer, R. Peters, C. Kränkel, A. G. Engqvist, M. Golling, D. J. H. C. Maas, K. Petermann, T. Südmeyer, G. Huber, and U. Keller, "Efficient femtosecond high power Yb:Lu₂O₃ thin disk laser," *Opt. Express* **15**, 16966–16971 (2007).
 108. C. Paradis, N. Modsching, V. J. Wittwer, B. Deppe, C. Kränkel, and T. Südmeyer, "Generation of 35-fs pulses from a Kerr lens mode-locked Yb:Lu₂O₃ thin-disk laser," *Opt. Express* **25**, 14918–14925 (2017).
 109. K. Hasse, T. Calmano, B. Deppe, C. Liebald, and C. Kränkel, "Efficient Yb³⁺:CaGdAlO₄ bulk and femtosecond-laser-written waveguide lasers," *Opt. Lett.* **40**, 3552–3555 (2015).
 110. S. Ricaud, A. Jaffres, K. Wentsch, A. Suganuma, B. Viana, P. Loiseau, B. Weichelt, M. Abdou-Ahmed, A. Voss, T. Graf, D. Rytz, C. Hönninger, E. Mottay, P. Georges, and F. Druon, "Femtosecond Yb:CaGdAlO₄ thin-disk oscillator," *Opt. Lett.* **37**, 3984–3986 (2012).
 111. C. Schriber, L. Merceron, A. Diebold, F. Emaury, M. Golling, K. Beil, C. Kränkel, C. J. Saraceno, T. Südmeyer, and U. Keller, "Pushing SESAM modelocked thin-disk lasers to shortest pulse durations," in *Advanced Solid State Lasers Congress (2014)* (Optical Society of America, 2014), p. AF1A.4.
 112. J. Ma, H. Huang, K. Ning, X. Xu, G. Xie, L. Qian, K. P. Loh, and D. Tang, "Generation of 30 fs pulses from a diode-pumped graphene mode-locked Yb:CaYAlO₄ laser," *Opt. Lett.* **41**, 890–893 (2016).
 113. P. Sévillano, P. Georges, F. Druon, D. Descamps, and E. Cormier, "32-fs Kerr-lens mode-locked Yb:CaGdAlO₄ oscillator optically pumped by a bright fiber laser," *Opt. Lett.* **39**, 6001–6004 (2014).
 114. A. J. DeMaria, D. A. Stetser, and H. Heynau, "Self mode-locking of lasers with saturable absorbers," *Appl. Phys. Lett.* **8**, 174–176 (1966).
 115. J. S. Russel, "Report of the Committee on Waves," *Rept Brit Assoc Adv. Sci* **8**, 14 (1838).
 116. F. X. Kärtner and U. Keller, "Stabilization of solitonlike pulses with a slow saturable absorber," *Opt. Lett.* **20**, 16–18 (1995).
 117. C. Hönninger, R. Paschotta, F. Morier-Genoud, M. Moser, and U. Keller, "Q-switching stability limits of continuous-wave passive mode locking," *JOSA B* **16**, 46–56 (1999).
 118. A. Diebold, F. Emaury, C. Schriber, M. Golling, C. J. Saraceno, T. Südmeyer, and U. Keller, "SESAM mode-locked Yb:CaGdAlO₄ thin disk laser with 62 fs pulse generation," *Opt. Lett.* **38**, 3842–3845 (2013).
 119. A. Greborio, A. Guandalini, and J. Aus der Au, "Sub-100 fs pulses with 12.5-W from Yb:CALGO based oscillators," in *Proc. SPIE*, W. A. Clarkson and R. K. Shori, eds. (2012), p. 823511.
 120. Y. Zaouter, J. Didierjean, F. Balembois, G. L. Leclin, F. Druon, P. Georges, J. Petit, P. Goldner, and B. Viana, "47-fs diode-pumped Yb³⁺:CaGdAlO₄ laser," *Opt. Lett.* **31**, 119–121 (2006).
 121. C. R. E. Baer, C. Kränkel, C. J. Saraceno, O. H. Heckl, M. Golling, R. Peters, K. Petermann, T. Südmeyer, G. Huber, and U. Keller, "Femtosecond thin-disk laser with 141 W of average power," *Opt. Lett.* **35**, 2302–2304 (2010).
 122. R. Peters, C. Kränkel, S. T. Fredrich-Thornton, K. Beil, K. Petermann, G. Huber, O. H. Heckl, C. R. E. Baer, C. J. Saraceno, T. Südmeyer, and U. Keller, "Thermal analysis and efficient high power continuous-wave and mode-locked thin disk laser operation of Yb-doped sesquioxides," *Appl. Phys. B* **102**, 509–514 (2011).
 123. C. Benko, T. K. Allison, A. Cingöz, L. Hua, F. Labaye, D. C. Yost, and J. Ye, "Extreme ultraviolet radiation with coherence time greater than 1 s," *Nat. Photonics* **8**, 530–536 (2014).
 124. J. L. Krause, K. J. Schafer, and K. C. Kulander, "High-order harmonic generation from atoms and ions in the high intensity regime," *Phys. Rev. Lett.* **68**, 3535 (1992).
 125. F. Emaury, A. Diebold, C. J. Saraceno, and U. Keller, "Compact extreme ultraviolet source at megahertz pulse repetition rate with a low-noise ultrafast thin-disk laser oscillator," *Optica* **2**, 980–984 (2015).
 126. F. Emaury, A. Diebold, A. Klenner, C. J. Saraceno, S. Schilt, T. Südmeyer, and U. Keller, "Frequency comb offset

Bibliography

- dynamics of SESAM modelocked thin disk lasers," *Opt. Express* **23**, 21836–21856 (2015).
127. I. Pupeza, S. Holzberger, T. Eidam, H. Carstens, D. Esser, J. Weitenberg, P. Rußbüldt, J. Rauschenberger, J. Limpert, T. Udem, A. Tünnermann, T. W. Hänsch, A. Apolonski, F. Krausz, and E. Fill, "Compact high-repetition-rate source of coherent 100 eV radiation," *Nat. Photonics* **7**, 608–612 (2013).
128. G. Porat, C. M. Heyl, S. B. Schoun, C. Benko, N. Dörre, K. L. Corwin, and J. Ye, "Phase-matched extreme-ultraviolet frequency-comb generation," *Nat. Photonics* **12**, 387–391 (2018).
129. S. Hädrich, M. Krebs, A. Hoffmann, A. Klenke, J. Rothhardt, J. Limpert, and A. Tünnermann, "Exploring new avenues in high repetition rate table-top coherent extreme ultraviolet sources," *Light Sci. Appl.* **4**, e320 (2015).
130. A. Ozawa, Z. Zhao, M. Kuwata-Gonokami, and Y. Kobayashi, "High average power coherent vuv generation at 10 MHz repetition frequency by intracavity high harmonic generation," *Opt. Express* **23**, 15107–15118 (2015).
131. D. C. Yost, T. R. Schibli, and J. Ye, "Efficient output coupling of intracavity high-harmonic generation," *Opt. Lett.* **33**, 1099–1101 (2008).
132. J. Wu and H. Zeng, "Cavity-enhanced noncollinear high-harmonic generation for extreme ultraviolet frequency combs," *Opt. Lett.* **32**, 3315–3317 (2007).

Curriculum vitae

Name: Loïc Pierre Jean Marie Merceron

Date of birth: 19.09.1990

Nationality: French

Education:

2013- present: Doctoral studies at University of Neuchâtel, Switzerland

2011-2013: Master studies in Fundamental Physics in University of Bordeaux, France.

2008-2011: Bachelor studies in Physics in University of Bordeaux, France

Research Experience:

2018-present: Research and development engineer at Synova, Duillier, Switzerland

2013-2018: Research assistant at Laboratoire Temps-Fréquence (LTF), University of Neuchâtel, Neuchâtel, Switzerland

2011, 2012, 2013: Internships in research group at Centre des Lasers Intenses et Applications (CELIA), University of Bordeaux, Talence, France.

Remerciements

Enfin la fin ! Après tant d'années, le moment fatidique est arrivé : celui de la conclusion de ce travail de thèse. Avec celle-ci, vient le moment où je me remémore toutes les personnes qui ont rendu cette aventure possible. Ces personnes qui, au cours de ce long chemin m'ont apporté quelque chose qui m'a permis de faire un pas de plus.

En premier lieu, c'est toi Thomas que j'aimerais remercier ! Pour ta motivation constante, pour la confiance que tu m'as accordée, pour les idées (parfois un peu folles) que tu as, pour ton soutien en cas de coup dur, pour ta générosité et ton écoute.

Ensuite, c'est toi Stéphane que j'aimerais remercier, pour ton support sans faille, ta volonté d'aider, ta disponibilité que ce soit pour des questions techniques ou administratives, ta volonté de partager.

Un grand merci à toi Valentin pour ton soutien, ta générosité, ta constante volonté d'aider et tes conseils tant sur la technique que sur la manière de s'organiser autour d'une expérience scientifique.

Cette thèse n'aurait pas la même saveur sans les autres doctorants avec qui j'ai partagé, échangé et tant ri ! Je pense en particulier à toi Kutan, sans ton approche pédagogique et ta patience concernant les systèmes fibrés, sans ton humour décapant et tes farces, ce travail n'aurait pas été le même. Pierre, avec ton attitude toujours zen et bienveillante, tu m'as aussi beaucoup aidé en particulier avec tout ce qui touche à la mesure de bruit. Merci à toi Nayara ! Pour être l'amie que tu es, pour ton soutien, ton aide et toutes les astuces que tu partages sans réserve avec tous. Merci à vous Sargis, William pour tous les rires et les moments de détente franchement nécessaires durant ces années. Merci à tous les autres doctorants.

Mais le laboratoire Temps-Fréquence se compose également de post-doc, scientifiques senior, ingénieurs, techniciens et secrétaires qui m'ont également beaucoup aidé : François et Maxim qui m'ont toujours aidé et soutenu malgré les moments de stress. Clara pour m'avoir fait découvrir le monde de la recherche. Merci à toi Patricia pour ton aide et ton soutien. A vous Renaud, Christof, Florian, Mathieu, Patrick, Marc, Thierry, Isidro et tous les membres du LTF.

Une pensée émue pour toi Natacha, qui nous a quitté trop tôt mais dont je me souviendrai toujours des moments partagés ensemble : tant les rires que les pleurs.

La majeure partie de la thèse se déroule dans le laboratoire et avec les collègues, mais une autre part, elle aussi nécessaire prend place ailleurs, dans des cercles un peu plus élargis : celui des amis et celui de la famille. Ces personnes qui, de par leurs conseils et/ou leurs simple présence permettent au travail de prendre une nouvelle tournure.

Je vous remercie tous, mes amis et amies, de longue date, ou rencontrés au gré de mes activités à Neuchâtel, de mes voyages à l'étranger ou autre lieux insolites. Je pense d'abord à mes amis de longues dates rencontrés à Bordeaux : Kevin, Emilie, Emeline, Fabien, Pauline et Aymeric, Vincent et Florian, Sarah, Quentin, Jonathan et plein d'autres encore. A mes amis de fac : Ludovic, Morgane, Léona, Kevin, Yusuf, Morgan, Jessica, Jean-Baptiste (les deux) et encore tous ceux que je ne cite pas. Je pense ensuite à tous mes amis rencontrés à Neuchâtel et en particulier aux arts martiaux, qui ont pris une part non négligeable de ma vie tant dans la pratique qu'à côté : Bianca, Nathalie, Samuel, Louis, Fabien, Federica, Johann, Anthony, Damien, Lorena, Luca, Larissa. Mais je pense aussi aux avancés qui montrent vers où diriger nos pas : Loris en premier lieu, Katherine, Guido, Ivan, Catherine, Barbara, Pascal, Yves, Fabrizio, Quoc-Si et encore quelques autres. Et il y a enfin Olivier et Martine avec Tristan et Gladis, merci à vous quatre de m'avoir accueilli à Neuchâtel en premier lieu, mais encore Delphine, Maxime, Théa, Aurélien, Laura, Cécile, Laëticia, Hélène, Sandra, Michel, Maïwenn et encore quelques autres que je remercie pour simplement avoir été là ou pour avoir discuté avec quand j'en ai eu besoin.

En dernier lieu, je vous remercie Papa et Maman pour ces années loin de Bordeaux et durant lesquelles vous m'avez tant aidé et soutenu. Je pense également à vous, mes sœurs et frères, Clémence, Lucile et Pierre-Jean, qui chacun à sa façon m'a apporté un petit quelque chose qui m'a aidé à continuer. Je remercie aussi tout le reste de la famille, sans votre soutien tout ceci n'aurait pas été possible.